National Library of Canada

Acquisitions and Bibliographic Services Branch

395 Wellington Street
Ottawa, Ontario
K1A 0N4

Bibliothèque nationale du Canada

Direction des acquisitions et des services bibliographiques

395, rue Wellington
Ottawa (Ontario)
K1A 0N4

Your file Votre référence

Our file Notre référence

NOTICE

The quality of this microform is heavily dependent upon the quality of the original thesis submitted for microfilming. Every effort has been made to ensure the highest quality of reproduction possible.

If pages are missing, contact the university which granted the degree.

Some pages may have indistinct print especially if the original pages were typed with a poor typewriter ribbon or if the university sent us an inferior photocopy.

Reproduction in full or in part of this microform is governed by the Canadian Copyright Act, R.S.C. 1970, c. C-30, and subsequent amendments.

AVIS

La qualité de cette microforme dépend grandement de la qualité de la thèse soumise au microfilmage. Nous avons tout fait pour assurer une qualité supérieure de reproduction.

S'il manque des pages, veuillez communiquer avec l'université qui a conféré le grade.

La qualité d'impression de certaines pages peut laisser à désirer, surtout si les pages originales ont été dactylographiées à l'aide d'un ruban usé ou si l'université nous a fait parvenir une photocopie de qualité inférieure.

La reproduction, même partielle, de cette microforme est soumise à la Loi canadienne sur le droit d'auteur, SRC 1970, c. C-30, et ses amendements subséquents.

Canada

NITROGEN SUBSTITUTED CARBONS AS ELECTRODE MATERIALS FOR LITHIUM INTERCALATION BATTERIES

by

Wolfgang Weydanz

A THESIS SUBMITTED IN PARTIAL FULFILLMENT
OF THE REQUIREMENTS FOR THE DEGREE OF MASTER OF SCIENCE

IN THE DEPARTMENT OF PHYSICS

SIMON FRASER UNIVERSITY

JULY 1993

National Library of Canada

Acquisitions and Bibliographic Services Branch

395 Wellington Street
Ottawa, Ontario
K1A 0N4

Bibliothèque nationale du Canada

Direction des acquisitions et des services bibliographiques

395, rue Wellington
Ottawa (Ontario)
K1A 0N4

Your file Votre référence

Our file Notre référence

ISBN 0-315-91333-9

APPROVAL

Name: Wolfgang Weydanz

Degree: Master of Science

Title of thesis: Nitrogen substituted carbons as electrode materials for lithium intercalation batteries.

Examining Committee:

Chairman: Dr. Simon P. Watkins

Dr. Jeff R. Dahn
Senior Supervisor

Dr. Konrad Colbow

Dr. Brett Heinrich

Dr. Albert E. Curzon
Internal Examiner, Department of Physics, SFU

Date Approved: July 26, 1993

PARTIAL COPYRIGHT LICENSE

Title of Thesis/Project/Extended Essay

NITROGEN SUBSTITUTED CARBONS AS ELECTRODE MATERIALS FOR LITHIUM INTERCALATION BATTERIES

Author: ______________ __________

(signature)

WOLFGANG WEYDANZ

(name)

Aug 10, 1993

(date)

ABSTRACT

Nitrogen containing carbons, N_zC_{1-z}, have been made from different precursors at temperatures between 850°C and 1050°C. Their composition and structure have been studied by chemical analysis, powder x-ray diffraction, x-ray absorption spectroscopy and Auger electron spectroscopy. These techniques show that some nitrogen has been substitutionally incorporated for carbon. Nitrogen affects the behavior of $Li/Li(N_zC_{1-z})_6$ electrochemical cells in two ways. First, the irreversible capacity observed during the first electrochemical reaction of Li with N_zC_{1-z} (during the first discharge) increases with the nitrogen content of the samples. Secondly, the incorporated nitrogen causes a shift of the cell capacity to lower voltages compared to pure carbon electrodes. The first effect can be qualitatively understood using a model where Li reacts irreversibly with nitrogen containing species (we call these nitrogen atoms 'chemical nitrogen') to form lithium-nitrogen-organic compounds. The second effect is caused by the nitrogen which has been substituted for carbon in the lattice (we call this 'lattice nitrogen'). Such nitrogen containing carbons are not considered useful as anodes for Li-ion cells.

DEDICATION

I would like to dedicate this thesis with gratitude to all my excellent friends, especially Oliver Schnetz, and my family who all helped me overcome the difficult, and enjoy the easy parts of my studies in Germany and Canada.

I read and I forget

I see and I remember

I do and I understand

(unknown)

ACKNOWLEDGEMENT

Above all I would like to thank Dr. Jeff R. Dahn very much for his advice, guidance and encouragement throughout the research project. As well I would like to thank my fellow graduate students and lab companions for their help and fellowship and a very good lab atmosphere.

As well I would like to thank Dr. B. Heinrich and Mr. K. Myrtle for the use of their Auger instrumentation and the answering of never ending questions about the technique and equipment.

I appreciate the work done by the secretaries and the good cooperation and creative atmosphere found in the department as a whole.

In addition I would like to thank Dr. J.R. Dahn, Rotary International and Simon Fraser University for providing the necessary funding.

TABLE OF CONTENTS

CHAPTER ONE: INTRODUCTION

CHAPTER TWO: SAMPLE PREPARATION

CHAPTER THREE: POWDER ANALYSIS TECHNIQUES

CHAPTER FOUR: ANALYSIS AND RESULTS

TABLE OF CONTENTS (CONTINUED)

CHAPTER FIVE: DISCUSSION

LIST OF TABLES

LIST OF FIGURES

LIST OF FIGURES (CONTINUED)

LIST OF FIGURES (CONTINUED)

LIST OF FIGURES (CONTINUED)

LIST OF FIGURES (CONTINUED)

LIST OF FIGURES (CONTINUED)

CHAPTER ONE: INTRODUCTION

1.1 RECHARGEABLE BATTERIES

Our modern society is greatly dependent on all kinds of energy. With energy comes the problem of its availability and storage. For many applications electrical energy is the most convenient form to use, as opposed to energy from fossil fuels or thermal energy. Batteries are used to store electrical energy on a chemical basis. A lot of applications around the world rely on batteries, mainly when independence from a power net is required. As our society is getting more and more mobile, the demand for batteries rises greatly. Needs for many different applications have to be satisfied. The field of use extends from very small batteries, e.g. for pacemakers and watches to the rapidly growing field of medium size batteries (AAA to D cells) for all kinds of hand held electronic devices to car batteries and emergency storage units which are characterized by large energy storage capacities.

Batteries are classified into two major categories: primary or non rechargeable batteries and secondary or rechargeable batteries. Primary batteries are widely and cheaply available for a variety of applications. They can create problems in landfills due to the number of batteries and the toxicity of some of their reactant materials. A more advanced concept is the secondary battery, which can be built using a wide variety of different chemical processes.

For different uses different batteries are required. A common goal for all applications is to increase the energy density of the battery. At the moment, energy densities for secondary batteries (typically 30-50Wh/kg for conventional technologies and around 75 Wh/kg for lithium cells [1-1]) are far less than the energy density of, for example, gasoline (12,000Wh/kg). One goal for battery researchers has been to reduce the gap between the theoretical (>1000Wh/kg) [1-2] and practical energy densities of batteries. Other considerations are cell voltage, long shelf life (meaning as little self discharge over time as possible) and high cycle life (as many charge/discharge cycles as possible without dramatic loss of capacity). For large scale applications, as in electric vehicles, price, safety and environmental friendliness are concerns as well.

With the recent decision by the state of California to require 10% of all new car sales to be 'zero-emisson vehicles' by the year 2005, electric vehicles are moving more and more into the public eye. Thus a large demand for light weight batteries with high energy density has been created very suddenly. Requirements for an electric car battery are a specific energy of about 80-120Wh/kg to reduce battery weight to a reasonable amount [1-3,1-4]. A 1989 study with requirements of 21kWh minimum stored energy and 700kg maximum battery weight (30Wh/kg) [1-5] showed that at that time no existing battery system was able to meet these performance requirements when coupled with low cost, environmental friendliness and safety.

Different concepts have been used historically to build rechargeable batteries. The first kind of electrochemical cells were metal-acid batteries, of which lead-acid batteries are most well known. They are bulky and heavy but still widely used e.g. as starter batteries for cars. Later, nickel-cadmium batteries appeared with longer cycle life and higher energy density. Nickel-cadmium cells are also maintenance free and can deliver high current pulses due to their low cell resistance. But they have a high self discharge rate. Another major disadvantage is that they contain cadmium, which is considered highly toxic.

Looking closely at the periodic table, recent developments in the battery field can be understood. They are based on the idea that weight and electronegativity are the two main factors to be considered for high energy density. Elements in the top rows of the periodic table are to be preferred for light weight batteries. Elements on the left side of the periodic table are electropositive and good candidates for anodes, whereas materials on the right are electronegative (except for the noble gases) and thus good candidates for cathodes. Nickel-metal hydride batteries are based on the lightest element of all, hydrogen. Unfortunately a storage medium, such as a metal compound, storing hydrogen as H_xMe, is necessary, as hydrogen is not a solid at room temperature. These batteries became commercially available recently, improving battery performance compared to nickel-cadmium cells and eliminating the toxic cadmium in the cell at the same time.

Lithium is the next material to consider, with the highest overall charge density of 3860Ah/kg. This assumes an electrochemical reaction using one electron per atom. Rechargeable lithium batteries have several advantages over the formerly mentioned concepts for designing secondary batteries. They have high energy densities of up to 100Wh/kg for AA-size batteries and also show a cell voltage of around 3.5V, compared to between 1.2V and 2.0V for all conventional systems. They have an extremely high shelf life of up to 5 years with little capacity loss and contain little or no toxic materials.

The first generation of lithium batteries was manufactured using lithium metal as anode material, some organic solvent with a lithium salt dissolved in it as an ion transmitter (the electrolyte) and a cathode. These cells developed some serious safety problems due to the highly reactive metallic lithium in the cell. Lithium reacts with the electrolyte, but a passivating film is normally quickly formed, which prevents further reaction. Only under unusual circumstances like short circuiting or overheating of heavily cycled cells can this reaction lead to dramatic cell 'venting with flame' [1-6]. Despite this problem it was still desirable to keep lithium as the active material in rechargeable batteries. Thus a safe lithium battery was sought.

Based on the above findings, the cell design for lithium batteries was modified to a new concept. The new cells are called 'rocking chair' [1-7] or 'lithium-ion' [1-8] cells. In these cells metallic lithium is eliminated. Instead, a graphitic carbon is used as the anode and an air stable lithium transition metal oxide compound like $LiMn_2O_4$ [1-9,1-10] is used as the cathode. A phenomenon, called 'intercalation', is observed for these materials. Intercalation is the reversible insertion of 'guest' atoms into 'host' solids. Both, carbon and Mn_2O_4 are good intercalation compounds, which means that guest atoms can easily move into the host material and can be removed from it in the same fashion.

Carbon is a preferred element for batteries as well, since it has a very low atomic weight. This increases the energy density of the cell, which is desirable. Cells made from carbon and lithium transition metal oxides also show high voltages of around 3.0V to 4.5V, depending on the transition metal used. A higher voltage is good as it raises the energy density of the cells. Self discharge of these cells is as low as 1% a month [1-11].

The as-built lithium-ion cell is in the discharged state and has to be charged first. During charge the lithium is transferred as ions from the lithium transition metal oxide electrode through the non-aqueous electrolyte solution into the carbon compound at the other electrode. The electrons are forced over to the carbon electrode by the charger. The lithium ions and electrons recombine at the carbon surface and the lithium is intercalated as atoms within the carbon structure. On discharge the process is reversed and the lithium is deintercalated from the carbon and again intercalated in the Mn_2O_4 compound. Thus the lithium atoms 'rock' back and forth between the two electrodes. This concept avoids dealing with elemental lithium at any time and also has the advantage that all materials are air stable and the batteries can be manufactured under ambient conditions.

1.2 CARBON ELECTRODES

We are not going to discuss the lithium transition metal oxide electrodes any further, although many groups are researching them. Our aim is to look closer at the properties of the carbon electrodes for lithium batteries.

Carbon is an element of the first full period in the periodic table and exists in three basic modifications. The first modification is diamond, which does not intercalate lithium at all and is not of interest to us here.

Graphite, the second modification of carbon, has completely different properties than diamond. It is soft and flaky, looks black and feels a bit greasy to the touch. It has a quasi two dimensional structure of interconnected, 6-membered carbon rings, joined together to form a honeycomb pattern. Figure 1.1 shows the graphite sheet structure and a unit cell [1-12]. Its crystal structure is hexagonal with a four atom basis [1-13], two atoms each from two adjacent layers.

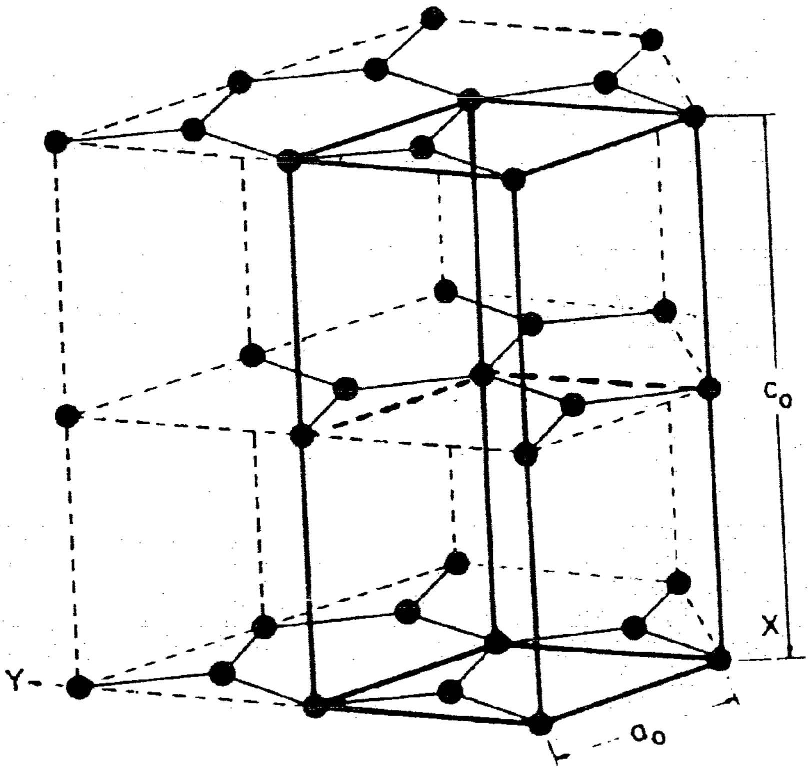

Fig. 1.1 Honeycomb layer structure for graphite and drawn in unit cell of four atoms from two adjacent layers. Adjacent layers are shifted by 1/3 unit cell to give ABABAB stacking, from [1-12].

The layer stacking is ABABAB, where adjacent layers are shifted by 1/3 of a unit cell along the (110) crystal direction with respect to each other. The two dimensional layers in graphite are loosely connected by van der Waals bonds. The nearest-neighbor distance in the c-direction is more than twice the nearest-neighbor distance within the a-b plane of the sheets. The material is very soft and can be split into these plane sheets easily. This property made graphite a widely appreciated lubricant, even well before our century.

The third and most recently discovered modification of carbon is the C_{60} or buckyball modification. In this structure 60 carbon atoms form a soccerball-like closed structure. Other structures can be constructed using a different number of carbon atoms, e.g. 54 or 72, but they are not as uniform and symmetric as C_{60}. The C_{60} balls crystallize in an orientationally disordered face-centered cubic (fcc) structure below 250K and have a first order phase transition at that temperature into an orientationally ordered simple cubic structure [1-14]. As well they can be intercalated with other atoms like cesium and potassium and are superconducting as Cs_3C_{60} and K_3C_{60} [1-14]. Buckyballs are said to hydrogenate and thus could be used as electrode materials in nickel-hydride batteries in the future [1-15]. They are also reported to electrochemically incorporate lithium up to $Li_{12}C_{60}$, which is roughly equal to the amount of lithium that can be hosted by graphitic carbons. However, this lithium intercalation is only reversible up to Li_3C_{60} [1-16]. Comparatively, little is known about the properties of the bulk C_{60} compared to graphite. This is not surprising as pure C_{60} costs $355 per gram at the moment [1-15].

Only the graphite structure modification will be discussed below. This does not mean that all samples produced and described here show the ideal graphite structure. But the goal is to produce materials that are as close as possible to that ideal structure. This is desirable, as earlier research has shown that the best intercalation results for lithium into carbon are achieved for carbons that are close to the ideal graphite structure [1-17]. In this context it is interesting to notice, that material produced at low temperatures (under 900 C) by decomposition of hydrocarbons has some hydrogen atoms still bonded to the carbon atoms. These hydrogen atoms are lost when the material is heated to higher temperatures under an inert gas or if the carbon is made at higher temperatures. The loss of hydrogen has a minor effect on the compound by reducing its layer spacing slightly for higher temperatures.

Another factor influencing the structure of carbons produced at low temperatures is called 'turbostratic disorder' [1-18]. This means that the carbon sheets are not completely coplanar and perfectly stacked in the ABABAB structure. They are to a certain extent randomly oriented. When carbons are heated up to 3000^{o}C under an inert gas, the material orders more and more in the ideal graphite structure and the turbostratic disorder is reduced with treatment temperature and length of treatment. This orientation process is called 'graphitization' of carbons [1-16,1-19,1-20]. It can be clearly observed by a reduction of the c-axis lattice spacing of the material with increasing temperature. This effect has been experimentally shown by x-ray studies [1-21].

1.3 NITROGEN DOPING

Carbon in the graphite structure is a good electrode material for rechargeable lithium batteries. The properties of many materials can be enhanced by adding some controlled impurities to them, that is to dope them with another material. The idea of doping carbon with other elements is not new. Experiments of substituting boron [1-22,1-23,1-24], phosphorus [1-25,1-26,1-27] and both boron and nitrogen [1-28,1-29] for carbon atoms have been previously done.

Boron is the element adjacent on the left of carbon in the periodic table, and nitrogen is the one adjacent on the right. The difference between the atoms is that boron has only three outer electrons, where carbon has four and nitrogen five. Thus the substitution of carbon atoms by boron creates a lack of electrons in the material, the nitrogen substitution an excess of electrons. For boron it has been shown that this lack of electrons changes the battery properties greatly. Higher voltage capacity can be seen in a cell with a boron-carbon electrode against a lithium electrode $(Li/(B_xC_{1-x})_6$

cell) compared to a cell with pure carbon electrode (Li/C_6 cell) [1-24]. More details about boron substitution will be provided later, when we discuss electrochemical data from our experiments and compare it to pure carbon and boron substituted carbon cells.

Phosphorus doping has also been tried. Phosphorus is located in the periodic table to the right and one row down from carbon, directly underneath nitrogen. Thus it has five outer electrons, one more than carbon, and is also a considerably bigger atom due to its extra electron shell. This might introduce flaws in the crystal structure of the graphitic material, which are known to increase the reversible capacity of the respective cells. Cells with phosphorus doped carbons showed discharge capacity increases of around 30% compared to cells with pure carbon electrodes manufactured under the same conditions [1-25,1-27].

Boron combined with nitrogen is supposedly a material very similar to carbon. A boron atom combined with a nitrogen atom has 8 outer electrons, just as two carbon atoms do. The electrochemical properties for the reported material with a stoichiometry close to BC_2N was very similar to those observed for pure carbon electrodes [1-28].

Thus nitrogen doping was considered to develop better anodes for Li-ion cells. Nitrogen, like phosphorus, introduces extra electrons into the material. At the same time it has the advantage over phosphorus of being roughly the same size as a carbon atom. So it will probably not disturb the crystal structure as much as is the case with phosphorus.

This work, to our knowledge, presents the first systematic study of nitrogen doped carbons for battery use. We will describe the sample preparation, chemical and X-ray analysis of the samples and electrochemical studies performed on the novel materials.

1.4 ELECTROCHEMICAL CELL VOLTAGE

The voltage of an electrochemical cell is one of the main characteristics to describe its properties. It is a physical quantity that can be understood on the basis of chemical potentials of atoms in a solid. In our case the cell voltage is caused by the difference in chemical potential of the lithium atoms in the anode or in the cathode material. The cell voltage, V(x), can be described with the following formula at any time:

$$V(x) = -(\mu_{Li}[\text{cathode}] - \mu_{Li}[\text{anode}]) / e \qquad \text{(eq. 1.1)}$$

where $\mu_{Li}[..]$ is the chemical potential of lithium in the appropriate electrode, e is the elementary charge and x is the amount of lithium in the cathode [1-30].

Up to now we have been talking about commercial lithium-ion cells, where both electrodes have varying potential with lithium content. For scientific purposes it is necessary to isolate the effects at both electrodes by using a lithium metal electrode as a 'neutral' reference electrode. We will further be talking about cells with lithium versus carbon electrodes, to eliminate the effects at the transition metal oxide electrode. For these cells the potential difference between the electrodes and thus the cell voltage varies during the discharging and charging process of the cell as the amount of lithium, x, in the carbon electrode varies. Intercalation cells can be used to measure the chemical potential of guest atoms in the host solids by means of cell voltages.

For the lithium-carbon electrochemical cells described here, the cell voltage is about 2.8V to 3.2V for an as made (fully charged) cell. As the cell discharges, x in Li_xC_6 increases up to a maximum of $x=1$ for graphite while the cell voltage decreases at the same time to near 0.0V for $x=1$. This is the maximum amount of lithium that can be intercalated into graphite and its potential in the carbon host is then very close to that for lithium in lithium metal. The capacity associated with $x=1$ in Li_xC_6 for graphite is 370mAh/g, where the weight is the weight of the graphite host. We use this ideal capacity of graphite to calculate our discharge and charge currents, even though most other carbon materials do not intercalate to $x=1$ in Li_xC_6, but considerably less.

The charge and discharge currents are determined so that a change of $\Delta x=1$ in Li_xC_6, meaning a full ideal discharge or charge of a graphite containing cell would take place in a certain time, e.g. 50 or 150 hours. These will be referred to as a '50 hour rate' or a '150 hour rate' respectively. The smaller the current, the slower the charging or discharging process and the closer the cell will be to equilibrium, which is important for studying the lithium intercalation process into carbonaceous materials in detail. As our cells do not intercalate x=1 lithium into carbon, but less as mentioned before, the respective charges and discharges for a 50 hour rate did not take the full 50 hours.

For lithium intercalation into pure graphite, different phases of the Li_xC_6 material are known for different values of x. The effect observed is the so-called staging, when lithium is intercalated in different stages between the sheets in the graphite structure. At first, lithium starts intercalating between every 4th sheet of graphite, which is called the stage-4 phase. Then a phase transition to lithium occupying every third layer is observed, called the stage-3 phase. This phase transition appears to be smooth, as determined from X-ray diffraction studies, indicating a coexistence of both phases. Islands of stage-4 phase shrink while those of stage-3 phase grow. The filling of sites in the graphite continues via a liquid like stage-2 and a normal stage-2 until stage-1 is reached and all possible lithium sites in the graphite are filled [1-31].

This behaviour can clearly be seen in the voltage curve for a lithium vs. graphite cell, meaning a cell with a lithium metal anode and a graphite cathode, as shown in Figure 1.2, from [1-31]. The voltage is plotted as a function of the amount of lithium, x, in the graphite electrode for the cell charge and discharge. We will plot most

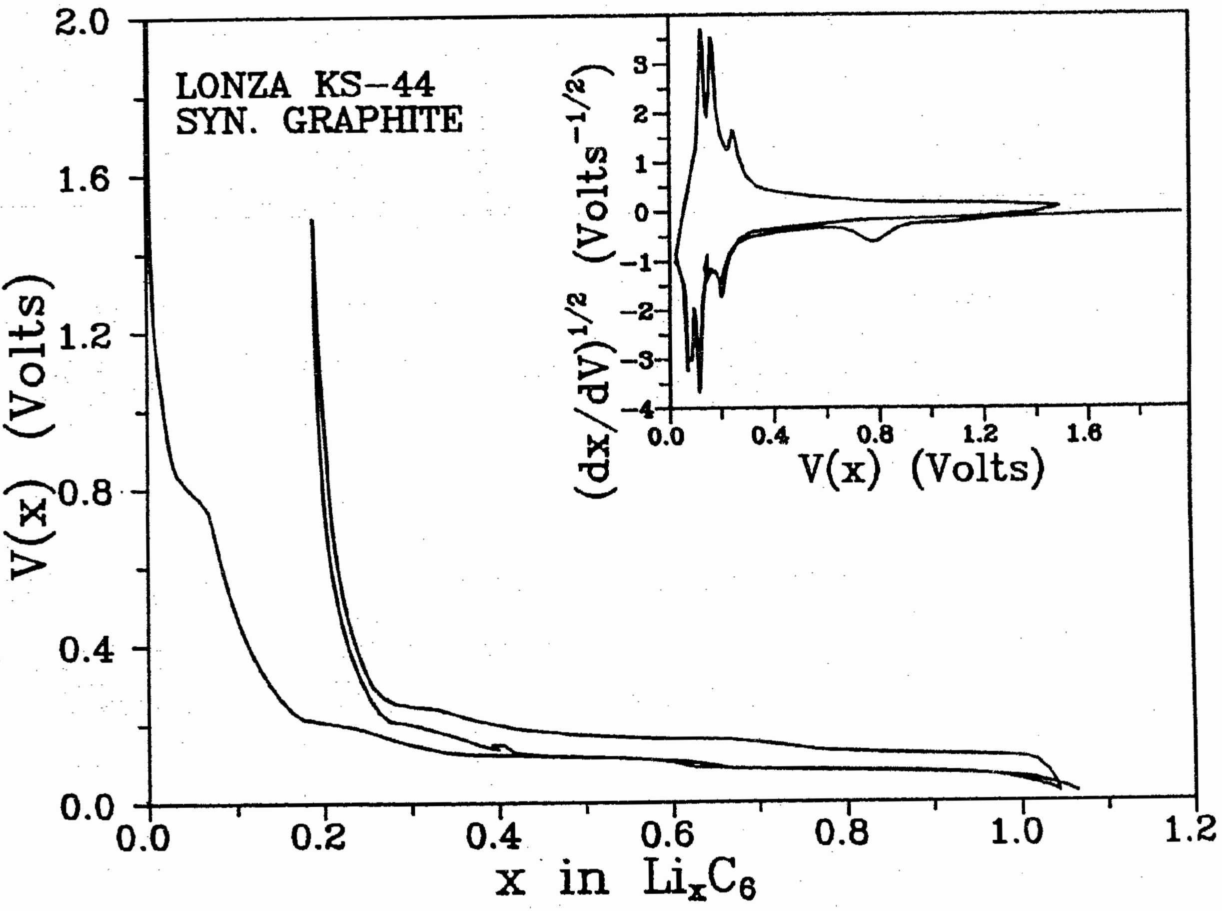

Fig. 1.2 Cell voltage versus x in Li_xC_6 for a cell with graphite electrode, showing plateaus for staging effects as described in the text, from [1-31].

of our voltage curves in this manner. The x-axis represents a capacity axis if we keep in mind that the value for x in Li_xC_6 multiplied by 370 is equivalent to the cell capacity in mAh/g. As the chemical potential in coexisting phases is equal, plateaus appear in the voltage curve at points of first order phase transitions. We also see, that most of the lithium is intercalated into graphite at cell voltages below 0.25V.

The above described plateaus in the voltage curve for graphite vs. lithium cells can not be observed in cells with more disordered carbons like 'cokes', 'pitches' or materials decomposed from e.g. benzene. This is due to the disorder in those materials. In perfect graphite all sites for lithium are energetically equal, as all nearest-neighbour environments are the same in this perfectly stacked material. Less perfect carbon materials have stacking faults with random rotation and translation of the adjacent carbon sheets. Thus not all nearest-neighbour environments are alike and the site energies vary from site to site. The disorder in the host suppresses staging as the energetically lowest sites are filled first. These are randomly distributed throughout the material. A smoother voltage curve without the distinct plateaus, as shown in Figure 1.3 for a cell containing our material decomposed from benzene at 900°C, is characteristic for these carbons [1-32]. Sites are available for all different binding energies between lithium and the host material and thus the curve is smoothed out and does not show any distinct plateaus any more. These carbon materials also intercalate considerably less lithium than x=1 in Li_xC_6, e.g. our material intercalates about x=0.65 reversibly.

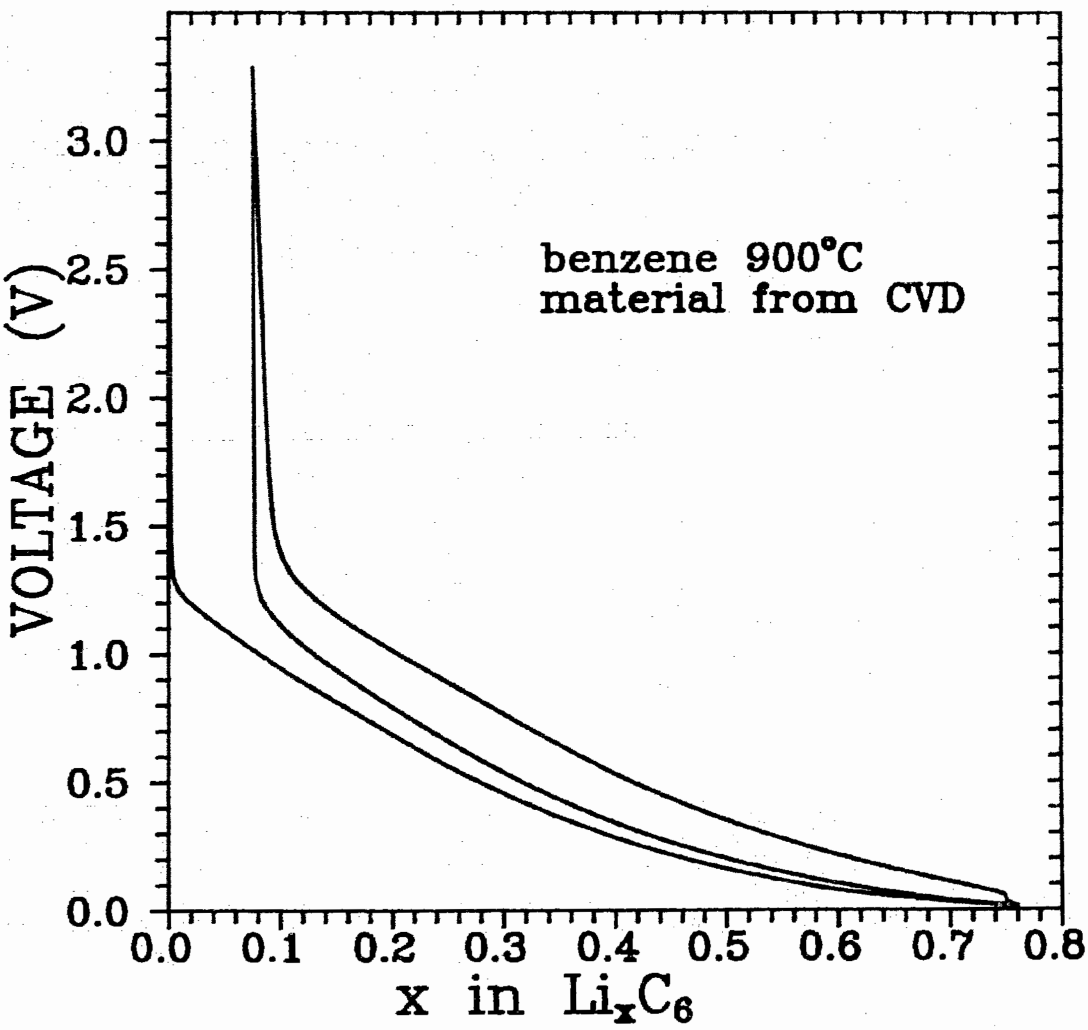

Fig. 1.3 Cell voltage versus x in Li_xC_6 for the first cycle and second discharge for a cell made from the benzene 900°C reference.

CHAPTER TWO: SAMPLE PREPARATION

Four different types of samples were produced using two different experimental methods. We will describe the two setups used and outline the further processing of the samples. The two setups used for sample production are fairly similar.

The first is a chemical vapor deposition reactor (CVD) which was used for the reactions of two different gaseous reactants. The second setup is an ordinary furnace which was used for pyrolyzing a single substance. The substances used in the furnace depositions were liquids with a vapor pressure on the order of 100 torr at room temperature.

2.1 CHEMICAL VAPOUR DEPOSITION (CVD)

A Vactronic CVD-300M hot wall reactor as shown schematically in Figure 2.1 was used. Two reactant gases, acetylene (C_2H_2) and ammonia (NH_3) (schematic strutures for these molecules are shown in Figure 2.2), were introduced into the quartz reactor tube through mass flow controllers. Two different flow rate combinations were used. For the first combination, further referenced as (1:1), the flow rates were established at flow meter readings of '150 flow' for both gases. Both gas flow rates were afterwards calibrated to give flow rates of

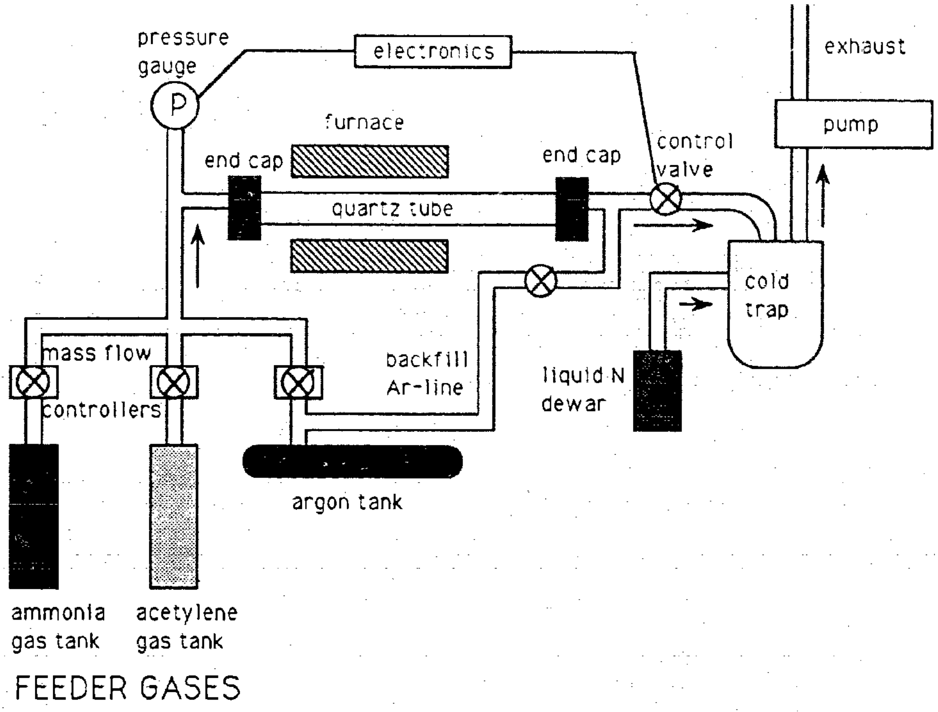

Fig. 2.1 Sketch of the chemical vapour deposition reactor (CVD) setup used for producing samples from acetylene and ammonia.

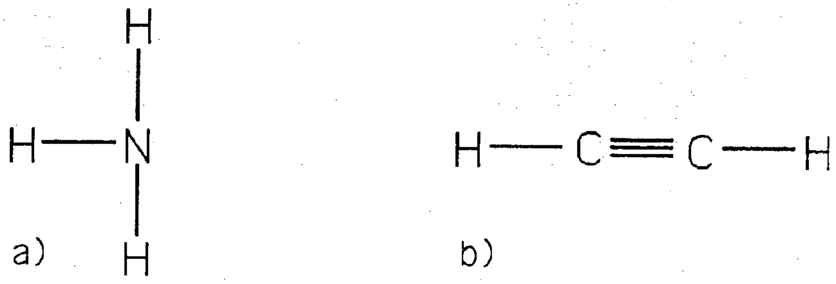

Fig. 2.2 Schematic structures for the a) ammonia and b) acetylene molecules.

85ccm/min (standard cubic centimeters per minute) for acetylene and 127ccm/min for ammonia. We will still use the notation of (1:1), although the 'real' flow rates do not resemble this proportionality any more. For the second combination, referred to as (2:3), the acetylene flow was dropped to a meter reading of '100 flow' while the ammonia flow was kept at '150 flow'. These flow rates convert to 56ccm/min for acetylene and 127ccm/min for ammonia. The error for all 'real' flow rates values quoted above is 5%.

The reaction product was deposited in the tube and the unreacted precursor gas was caught in a cold trap cooled by liquid nitrogen. A throttle valve and pump were used to keep the system at constant pressure during the deposition process. The base pressure inside the reaction tube was kept at 80-85 Torr by adjusting the backfilling with argon as much as necessary to maintain this pressure.

The deposition was continued at constant temperature - within about 3°C of the set point - for two to eight hours. The temperature was the independent parameter for the series of different samples produced. Not only the stoichiometry of the samples, but also the deposition rate depended on temperature. Thus, the length of the runs had to be adjusted to obtain sufficient amounts of powder, ideally in excess of 500mg. The temperature range was limited to three different deposition temperatures (900°C, 950°C and 1000°C). For 850°C no deposition of material was observed. The upper limit of 1000°C was due to the inability of the furnace to maintain temperatures over 1010°C once the reactant gas flow was switched on.

The resulting materials were either shiny black flakes or a black fluffy powder deposited inside the tube. This was in accordance with previous observations [2-1]. The shiny flakes are found in the hot zone of the furnace and the fluffy powder is formed on the edges and downstream from the hot zone. Very little deposition is observed upstream from the hot zone but often a tar-like black substance is found there. Anywhere between 100mg and 2.0g of material was produced in a single run. This reaction product was scraped off the inside of the tube with a long handled scalpel. Then the powder was further processed as described below.

To prepare the CVD system for the next run, it was taken apart and the quartz tube was burned out in air at about 900°C for roughly an hour to burn out all left over traces of powder, that had not been recovered. The tube was considered clean after this procedure, as all the black powder had been burned away without residue.

2.2 FURNACE DEPOSITION

For the other three depositions a normal furnace with a quartz tube as shown in Figure 2.3 was used. The hot zone of the furnace was

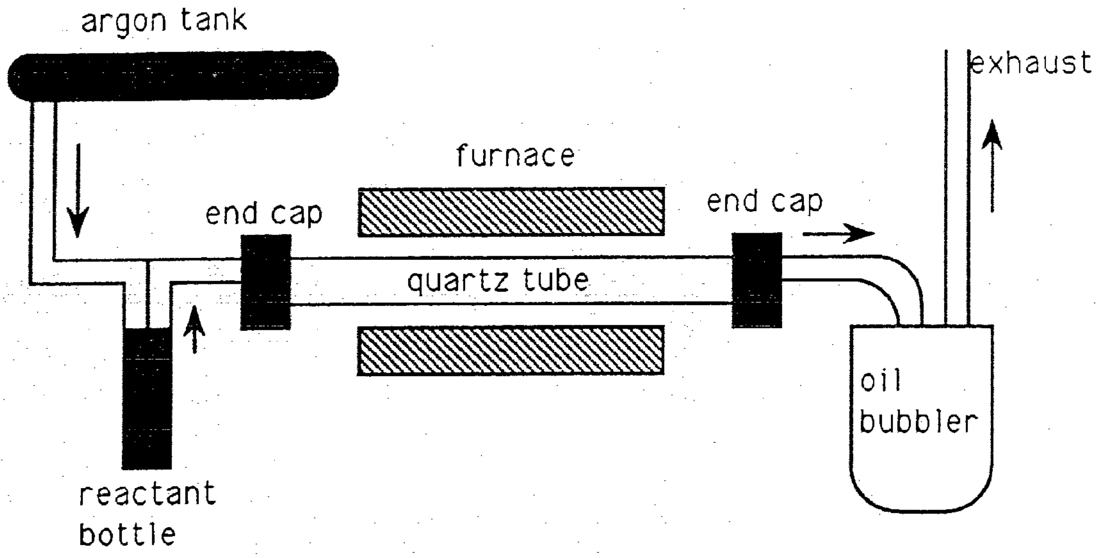

Fig. 2.3 Sketch of the furnace setup used for pyrolyzing benzene, acetonitrile and pyridine.

about 40cm long. The tube was fitted with end flanges, that could be sealed tight with brass caps. The inlet end cap was connected to the feeder gas line via a gas feed-through and the outlet end cap was connected to an oil bubbler to prevent backflow of air into the tube. The tube was flushed with argon for 10 minutes before the deposition started to create an oxygen-free atmosphere to eliminate reaction of oxygen with the feeder gas.

The setup for the pyrolysis of either of the three different materials, benzene (C_6H_6), pyridine (C_5H_5N) and acetonitrile (CH_3CN)

(schematic structures for these molecules are shown in Figure 2.4), was the same. A steady flow of argon was established through a stainless steel bottle with the reactant in it. The argon acted as a carrier gas, carrying some of the reactant into the furnace, where it was pyrolyzed and deposited on the tube walls. The deposition took place at atmospheric pressure. The flow rate of argon with the reactant in it was kept at about 3ccm per second. This meant that roughly 1g of the reactant was brought into the furnace per hour. The yield turned out to be high. An exact determination of the yield was not of major concern to us.

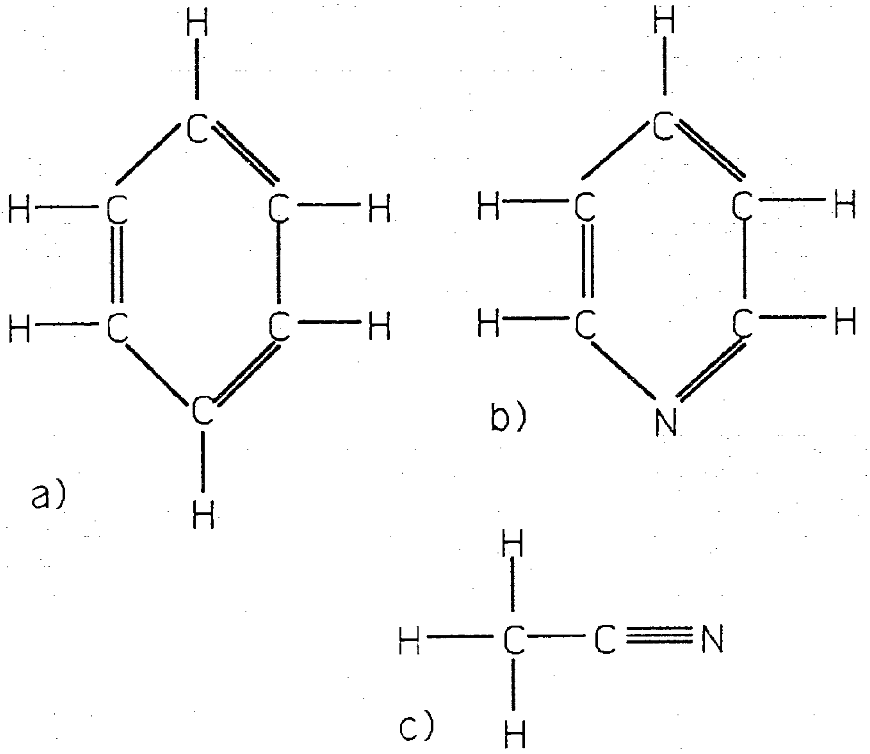

Fig. 2.4 Schematic structures for the a) benzene, b) pyridine and c) acetonitrile molecules

As described in Chapter 2.1, two main products were again found, shiny flakes and a fluffy powder. The flakes had been deposited roughly in the downstream half of the hot zone whereas the fluffy powder was deposited in the upstream half of the hot zone. Some tarry material was found outside the hot zone. The powders were retrieved as described above and the quartz tube was cleaned as described before.

2.3 TERMINOLOGY

For the different samples produced, the following terminology will be used. The carbon and carbon-nitrogen materials will be referred to by the name of the precursor material from which they were produced. This will be followed by a temperature reading in °C, specifying the conditions under which the powder was produced. From the above description it will thus be clear which production method was used.

For example, the material 'benzene 900°C' would refer to carbon material produced from benzene at 900°C in the simple furnace. For the materials produced in the CVD from acetylene and ammonia, the material abbreviation $C_2H_2:NH_3$ (1:1) or (2:3) followed by the temperature reading will be used, according to the ratio of flow rates of the gases, as described above. The acetonitrile samples will sometimes be referred to as 'aceto'.

Whenever the chemical material is mentioned without a temperature reading, the actual liquid or gaseous chemical is referred to and not the carbonaceous material produced from it in a deposition.

2.4 POWDER PROCESSING

The flakes were first ground thoroughly, which meant that a uniform powder was produced. This was normally achieved after 10 minutes of manual grinding. The maximum grain size of the flakes was thus reduced to below 100 microns, determined by a 200-mesh screen, which has 75 micron openings. All data presented here is taken from materials ground from the flakes.

Afterwards all powders were X-rayed for structural analysis as described in Chapter 3.3. below. After X-raying the powder, cathodes were made from it on copper foil. The powders were mixed with a 20% by weight solution of Polyvinylidenefluoride (PVDF) (as a binder) in 1-Methyl-2-Pyrrolidinone (NMP). Excess NMP was added to obtain a syrupy consistency of the material, which was then spread uniformly onto the copper foil using a doctor blade spreader. The NMP was evaporated in an oven at 105°C overnight and well adhering films of the powder material were obtained on the copper.

2.5 CELL PRODUCTION

The cathode material was cut into unit squares (12mm x 12mm) using a precision cutting jig and weighed. The weight of the copper substrate square was known to be 44.5mg. The weight of the electrodes was corrected for this substrate weight as well as the weight of the binder in the material. Thus the final weight of the active material was obtained. Typical electrodes had a thickness of about 150μm and an active weight of roughly 10mg. Then the cathodes and other cell parts were brought into a glove box with an argon atmosphere for assembly. This was done to protect the lithium electrode from harm by water vapor in the air during the cell manufacturing process.

As sketched in Figure 2.5, from [1-18], cells were built using the produced material as a cathode and lithium metal as an anode. The electrodes were separated by a separator, which had been wetted with electrolyte under pressure. A mixture of ethylene carbonate (EC: 25%), propylene carbonate (PC: 25%) and dimethylcarbonate (DMC: 50%) with lithiumhexafluorophosphate ($LiPF_6$) dissolved as an electrolyte salt (concentration 1 molar) was used as the electrolyte. This electrolyte constitutes the state of the art in electrolyte research [2-2].

The cell parts were assembled into a cell housing. The housing contains, apart from the active parts (lithium metal, separator with electrolyte and carbon cathode) a spacer disc to distribute the pressure uniformly over the electrodes and a spring to create the necessary pressure to keep the electrodes firmly in contact inside the sealed housing. The cells were finally sealed with a pressure crimper inside the glove box.

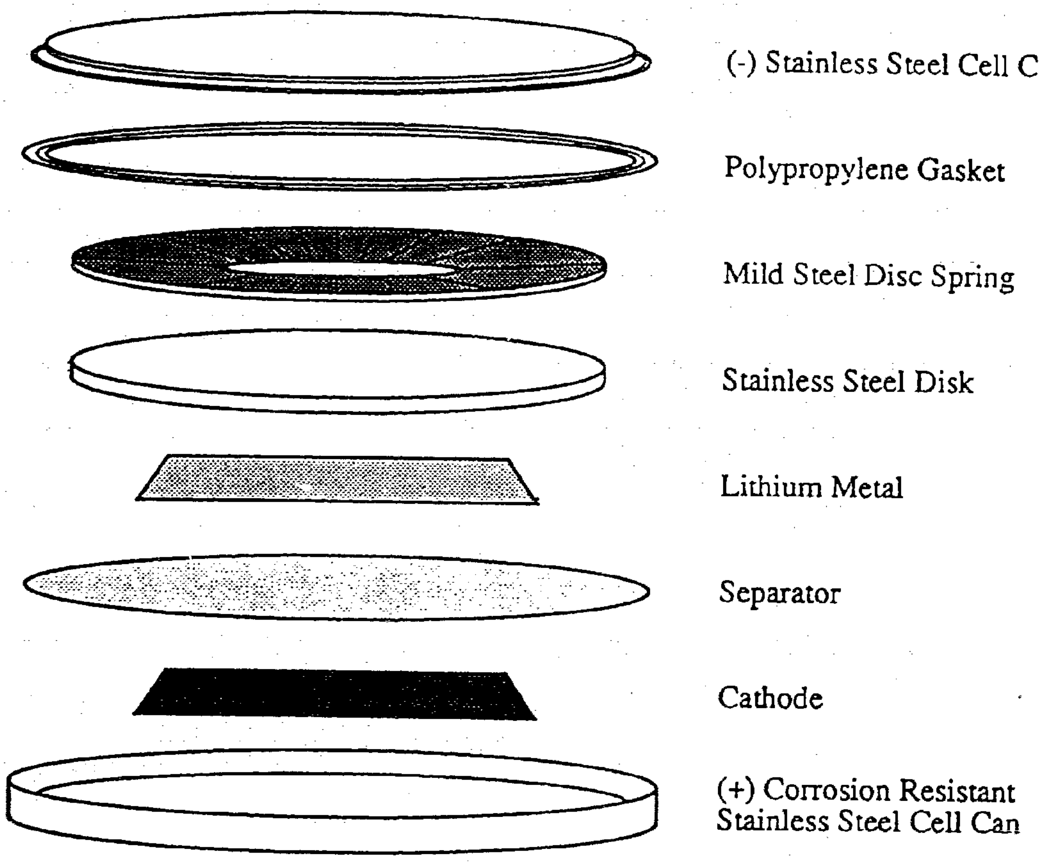

Fig. 2.5 Sketch of all parts contained in a coin cell as used for our cell experiments, from [1-18].

Only the sealed cells were taken out of the glove box and were then checked for voltage, which for a good cell should be around 3.0V. Cells with considerably lower voltages had either been short circuited in the production process or showed other flaws and were not usable for further experiments.

Afterwards the cells were charged and discharged using a computer-controlled constant-current charging system with current stability of ± 0.1%. The charge and discharge currents were equal and chosen so that a change $\Delta x=1$ in Li_xC_6 would take 50 hours. This is commonly referred to as a 50 hour rate. We used the previously calculated electrode mass and the specific capacity of pure carbon corresponding to Li_1C_6 (370mAh/g) for our calculation. No adjustments of the specific capacity were made for the mass differences for the nitrogen and hydrogen in the electrode material, compared to carbon. All cell testing was done at $30^oC\pm0.1^oC$ in a temperature controlled enclosure.

CHAPTER THREE: POWDER ANALYSIS TECHNIQUES

The powders produced as described in Chapter 2 had black to silverish appearance but were otherwise uncharacterized to this point. How much nitrogen did the different samples, in fact, contain? What was the crystal structure of the materials and where was the nitrogen located within it? Was it substitutional nitrogen, incorporated within the graphite honeycomb structure, or placed randomly in the material, for example between the carbon sheets? Finally, how would the nitrogen substitution affect the electrochemical intercalation of lithium as monitored by the cell charge and discharge profiles. We expected the voltage and the capacity of the cells to change somewhat due to the incorporated nitrogen. All of the above questions were addressed and the results are presented in the following sections and chapters making up the rest of the thesis.

3.1 CHEMICAL ANALYSIS

Small quantities (about 20mg each) of all potentially nitrogen containing samples and selected samples prepared from benzene, were sent to Canadian Microanalytical Services Ltd., Delta, B.C.. They performed chemical analysis for the elements carbon, nitrogen and hydrogen (C-N-H analysis) [3-1] on the samples. A Carlo Erba 1106

(Milan, Italy) gas chromatography unit was used, which works by burning the sample in pure oxygen in a quartz tube. The reaction products CO_2, H_2O and N_2 are then carried in an argon stream into an attached gas chromatography unit and identified quantitatively. This allows accurate determination of the masses of carbon, nitrogen and hydrogen in the initial material. Percentages by weight for those three elements in the original material can be calculated with an error of ±0.3% [3-1].

3.2 ANGULAR DEPENDENT X-RAY ABSORPTION SPECTROSCOPY

X-ray absorption spectroscopy (XAS) is a modern tool for structural and electronic analysis of solids. High intensity tunable radiation from electron storage rings (synchrotrons) is used to excite transitions between filled core states and unfilled conduction band levels. The experiments described here were done at the Canadian Synchrotron Radiation Facility (Grasshopper beamline) at the Alladin Synchrotron at the University of Wisconsin in Stoughton, Wisconsin. Details of the beamline are described in [3-2].

The total electron yield I_y from the sample is measured while the energy of the incoming photon beam is scanned over an energy range using the 'grasshopper' monochromator. The incident beam intensity I_o is simultaneously measured with a gold grid in the beam path before the beam hits the sample. We will display normalized intensities $I = I_y/I_o$

in all our XAS scans. We have to correct all data with an I_o reference, as the incoming radiation varies with time, mainly due to beam decay and noise and also varies with photon energy, mainly due to carbon in the system, as will be discussed below.

For nitrogen edge measurements it is sufficient to correct the data, I_y, with the I_o as defined above to obtain I. For carbon edge measurements, however, the I_o obtained from the gold grid can not be trusted, as carbon is widely present in the system and in particular on the monochromator grating and the mirrors. The carbon present on these system parts already absorbs about half of the incoming beam intensity around 285eV (the carbon absorption edge) compared to e.g. 260eV and gives us incorrect I_o values, as measured by the gold grid. Thus we need a reference spectrum that takes care of the presence of carbon in the system. The reference is a scan of the carbon edge (280eV to 325eV) on pure, clean silicon, which does not contain any carbon. It should not show any carbon absorption and we can say that the absorption observed from the measurement, as shown in Figure 3.1, is due to the carbon that is present in the system. All carbon edge data were corrected with this reference scan as the I_o value. Carbon is the only element that is present in this form within the system, so that this correction is not necessary for nitrogen or any other element [3-3].

The materials studied at the synchrotron were all flaky powders and thus not as well oriented as the original deposited film. As

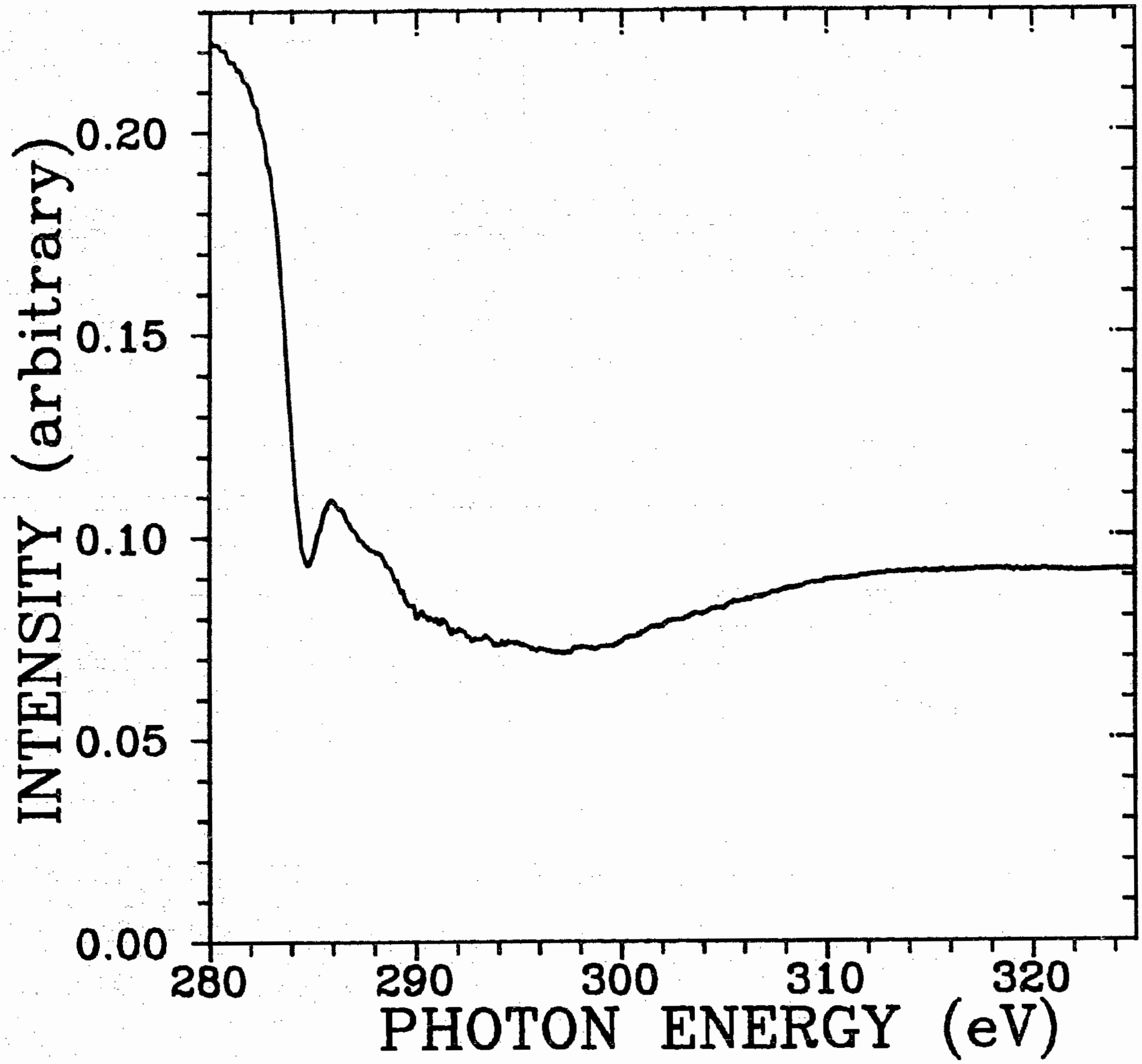

Fig. 3.1 XAS scan on clean silicon around the carbon edge, used as a reference for the carbon absorption in the system.

mentioned in Section 2.4, it was hard to grind these powders to small size, which was an advantage here. The powders were still tiny flakes, which were carefully pressed onto carbon tape using a flat glass surface. After several pressings the samples were substantially oriented with their c-axes normal to the sample surface.

All scans, which will be shown and described in Section 4.1.3 are measured in the following manner. The incident photon beam energy is scanned through a certain region (for the overview scan from 280eV to 430eV, for the carbon absorption edge from 280eV to 325eV and for the nitrogen absorption edge from 392eV to 430eV) by computer controlled motion of the 'grasshopper' monochromator. After every scan the angle of incidence of the beam on the sample is varied. For each film both the carbon and nitrogen edge were scanned at three different angles, 90^{o} (normal incidence), 59^{o} and 30^{o}, between the incident photon beam and the flat sample surface.

The basis of angular dependent XAS is that the different transitions into antibonding orbitals (denoted as σ^{*} and π^{*}) above the Fermi energy, E_F, are excited differently at certain angles. The σ^{*} orbitals have a spatial orientation along the connecting line of the atoms in the plane of the carbon sheets, as shown by the outlined empty electron orbitals in Figure 3.2a for an ethylene molecule, from [3-4]. They are formed from the s and the p_x and p_y antibonding orbitals to give a resulting sp^2-hybrid orbital. Graphite can be viewed as a compound made up of many connected benzene rings, so that all σ^* orbitals are in the x-y plane. They are simplified to a line connecting the atoms in Figure 3.2b, from [3-5], where the π^* orbitals are shown in their spatial orientation in the z-direction, perpendicular to the plane of the σ^* orbitals.

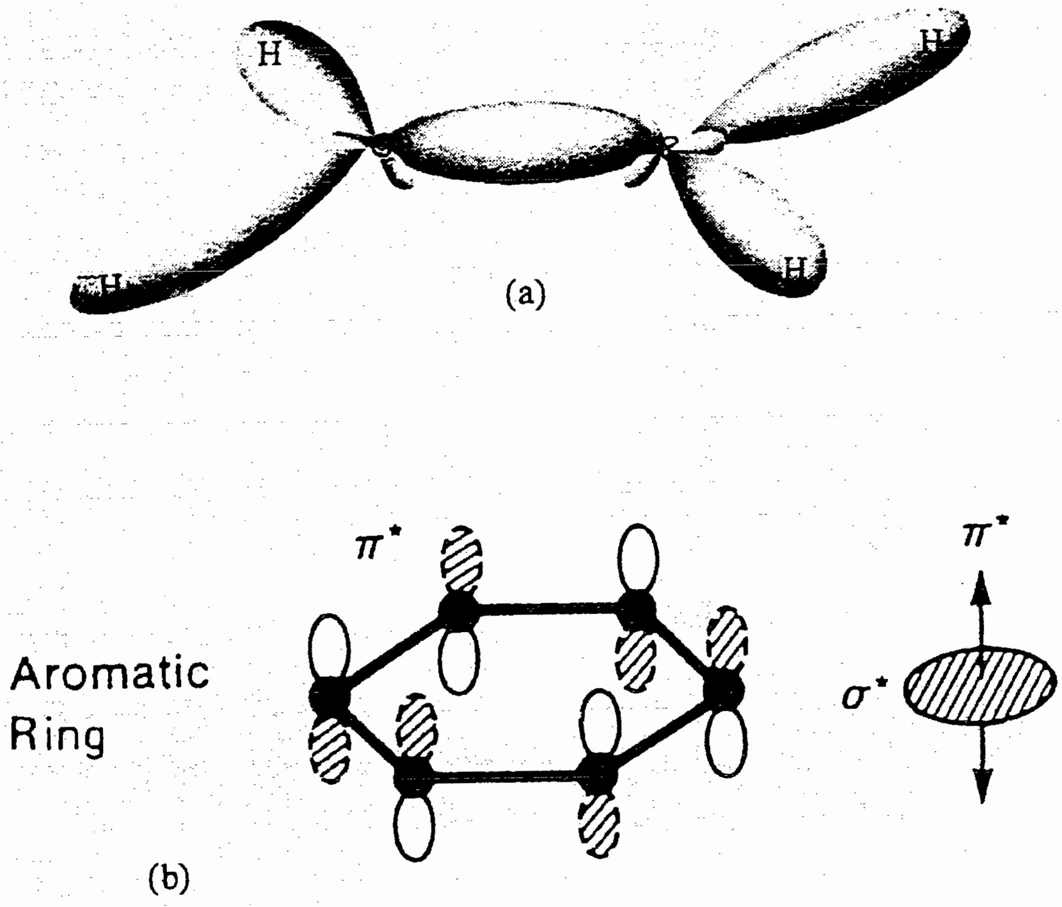

Fig. 3.2 Antibonding atomic orbitals. In a) the spatial orientation of the σ^*-orbitals in the x/y-plane is shown, from [3-4], whereas in b) the orientation of the π^*-orbitals in the z-direction is sketched for benzene, from [3-5].

The angle dependence of the absorption into both these final anti-bonding states is due to the reaction with the incoming polarized synchrotron radiation. The beam has an $\underline{E}$-field vector and a $\underline{B}$-field vector perpendicular to each other and perpendicular to the direction of wave propagation. We are interested in the $\underline{E}$-field vector here, as the dipole selection rules determine the transition from the initial 1s state $|i>$ to the $p_{x,y,z}$ component of the final state $<f|$, which can be a σ^* or π^* state. The intensity of the absorption into a final state $<f|$ can be described by:

$$I \sim | <f|\underline{e}\circ\underline{p}|i> |^2 \qquad \text{(eq. 3.1)}$$

where $\underline{e} = \underline{E}/|E|$ is the unit vector in the direction of the electric field of the synchrotron radiation and $\underline{p}$ is the momentum operator [3-5]. For linearly polarized light equation 3.1 simplifies to:

$$I \sim | \underline{e}\circ<f|\underline{p}|i> |^2 \qquad \text{(eq. 3.2)}$$

We can simplify eq 3.2 by substituting $\underline{p} = im/\hbar \circ [\underline{H},\underline{r}]$, where $[\underline{H},\underline{r}]$ is the quantum mechanical commutator of the Hamilton operator $\underline{H}$ with the position operator $\underline{r}$ and m is the electron mass, to arrive at:

$$I \sim | \underline{e}\circ <f|\underline{H}\circ\underline{r} - \underline{r}\circ\underline{H}|i> |^2 \qquad \text{(eq. 3.3)}$$

and applying $\underline{H}$ to get the respective eigenvalues, eq 3.3 simplifies to:

$$I \sim (E_f - E_i) | \underline{e}\circ <f|\underline{r}|i> |^2 \qquad \text{(eq. 3.4)}$$

where the matrix element $<f|\underline{r}|i>$ is a vector quantity, which points in the direction of the $\underline{r}$-component in the final state orbital, that is in the direction of maximum orbital amplitude of the final π^* or σ^* state and $(E_f - E_i) = \hbar\omega$, where ω is the angular frequency of the absorbed or emitted light.

The absorption with angle into final σ^* states, which are within the x-y plane, is described by:

$$I_\sigma \sim | <f_\sigma|\underline{e}\circ\underline{p}|i> |^2 = | \underline{e}\circ<f_\sigma|\underline{p}|i> |^2 \sim \sin^2\gamma \qquad \text{(eq. 3.5)}$$

where γ is the angle between the electric field vector $\underline{E}$ and the normal of the x-y plane. For absorption into the final π^* states, which are oriented in the z-direction, we find:

$$I_\pi \sim | <f_\pi|\underline{e}\circ\underline{p}|i> |^2 \sim \cos^2\gamma \qquad \text{(eq. 3.6)}$$

accordingly. This is valid for the case of the incoming radiation being 100% polarized with the $\underline{E}$ field vector in the horizontal plane of the electron orbit [3-5].

The two dimensional nature of graphite shows strong directionality of the orbitals, as shown above in Figure 3.2. Thus the σ^* orbital final state can only be reached if the $\underline{E}$-field vector has a component parallel to the x-y plane. This means that for maximum signal the beam has to hit the sample perpendicular to the x-y plane, thus perpendicular to the sample surface. For the π^* orbitals the opposite applies so that the beam has to hit the sample at grazing incidence to maximize absorption into the π^* states [3-6,3-7,3-8].

The σ^* and π^* bonding energies are slightly different. This can be seen from band structure calculations for graphite, as shown in Figure 3.3, from [3-6]. The figure shows a complete band structure calculation for all bands above the Fermi Energy, E_F. The bands we are mainly interested in are those associated with the two XAS features closest to

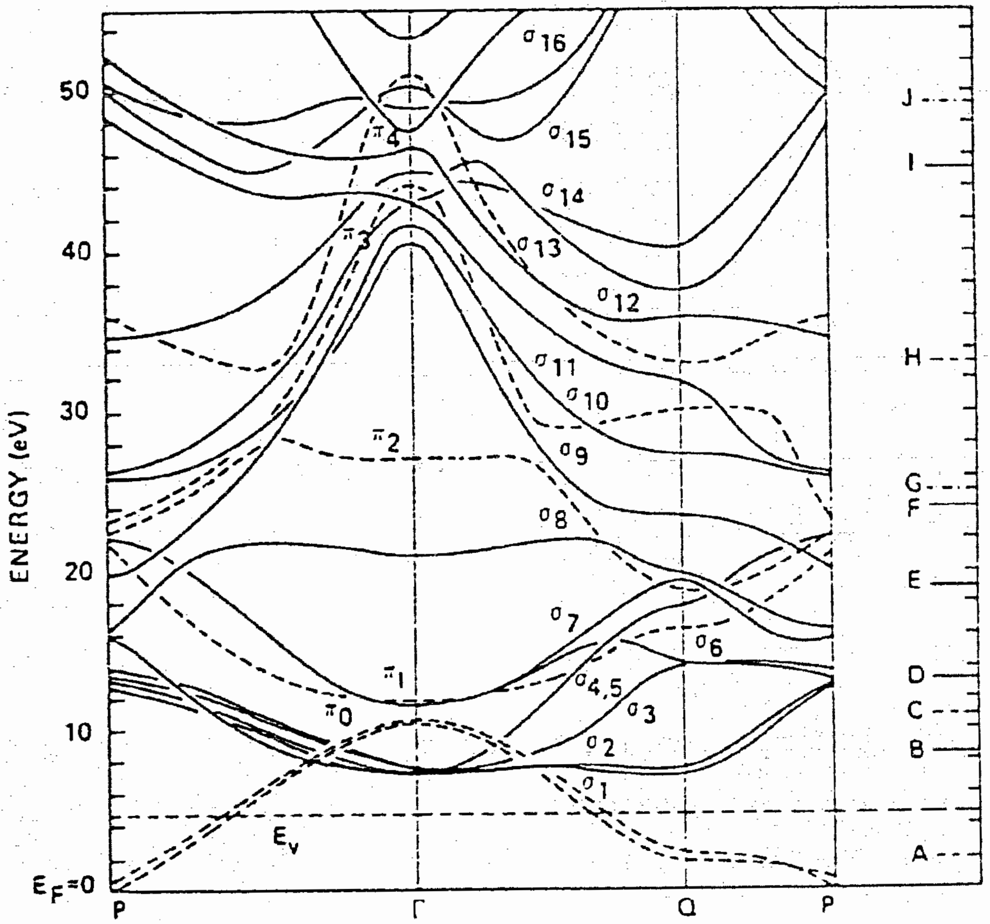

Fig. 3.3 Band structure calculation of all bands above E_F for graphite, from [3-4].

the respective absorption edge. We refer to them as π^* and σ^*, as they originate from the bands marked as π_0 and σ_1-σ_5 respectively in the calculation in Figure 3.3. The energy for the π^* band is marked with 'A' at 2.0eV above E_F and the one for the σ^* band is denoted 'B' at 8.4eV above E_F. The letters 'A' and 'B' correspond to the letters that refer to the first two features of the carbon K absorption edge spectra shown in Figure 3.4, from [3-6]. We can see a clear dependence of the π^* and σ^* peaks on angle for the highly oriented pyrolytic graphite samples (HOPG), which is expected from theory. The angular dependence is governed by above mentioned transition matrix elements for the respective orbitals.

From the band structure calculation we can also obtain a density of states plot, shown in Figure 3.5. We only show the density of states close to the Fermi energy, E_F, as this is the region of interest to us. The chemical bonding of lithium as well as the shift of E_F due to the boron or nitrogen substitution can be understood from this narrow region around E_F. Lithium that intercalates into carbon transfers one electron per lithium atom to the carbon host. This corresponds to the filling of all empty electronic states in the carbon up to 1.3V above E_F for Li_1C_6, as calculated earlier [3-9]. We will refer to the density of states plot further in Section 5.

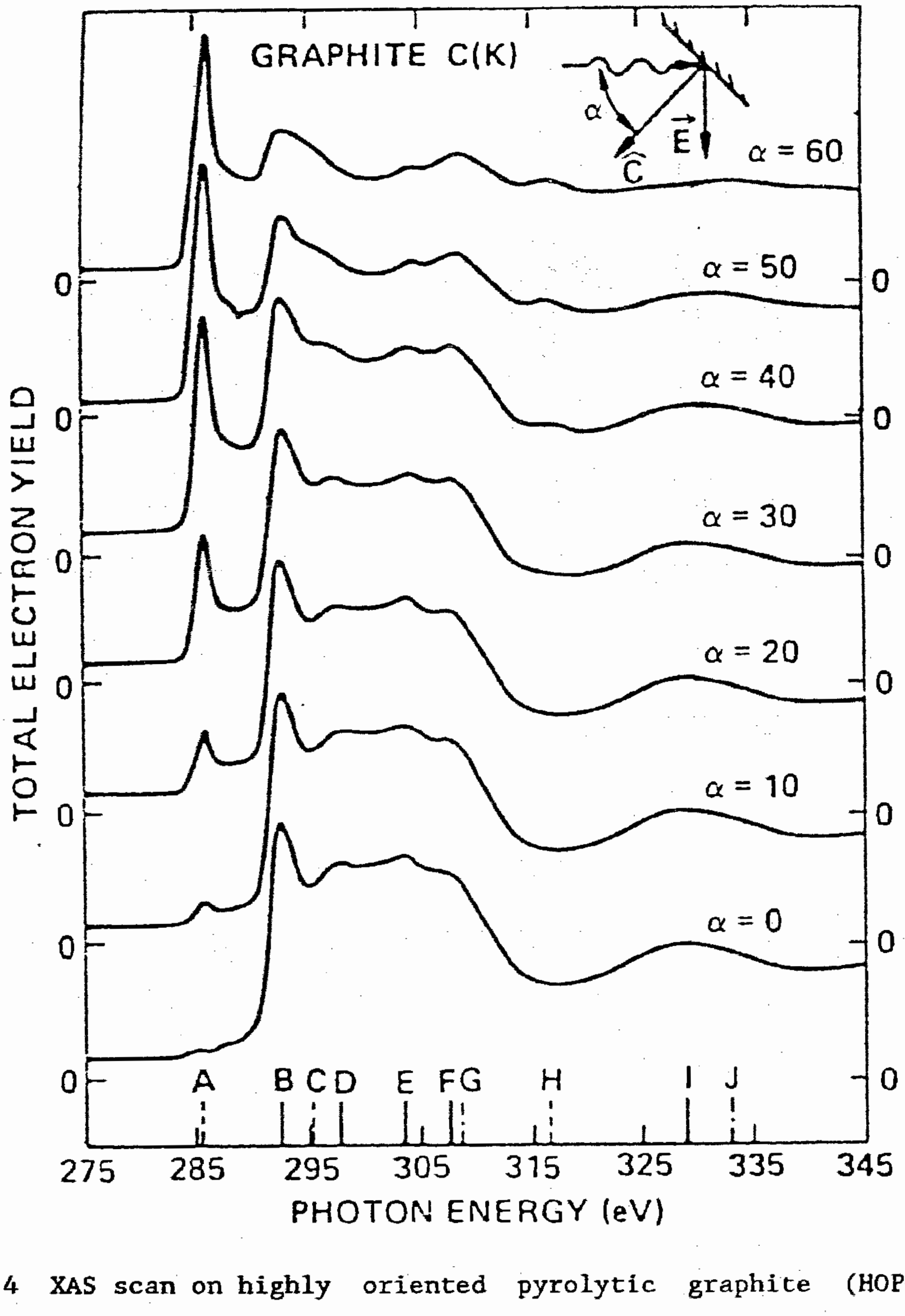

Fig. 3.4 XAS scan on highly oriented pyrolytic graphite (HOPG), exhibiting dependence on angle between the incident beam and the sample surface, as described in the text, from [3-6].

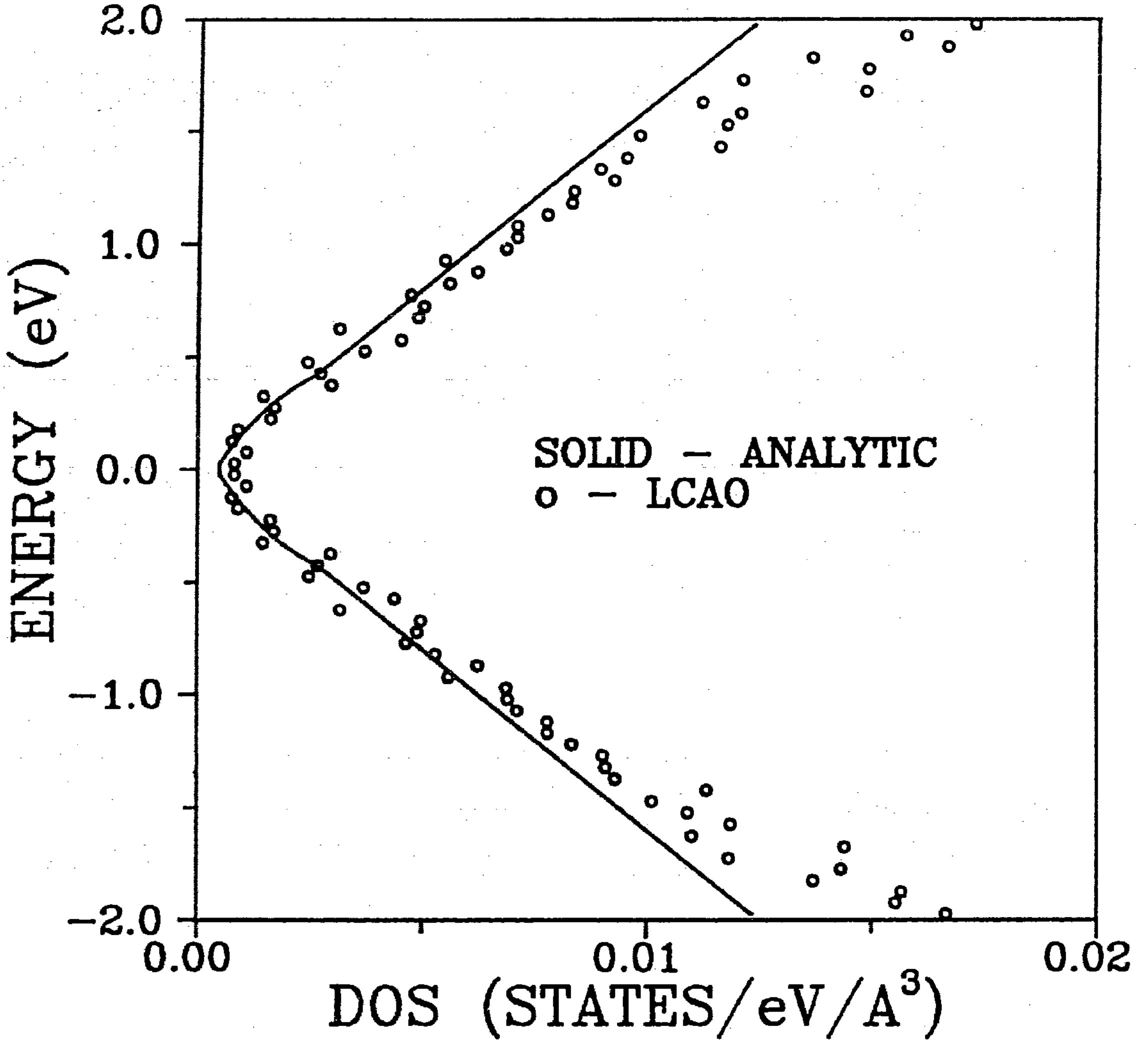

Fig. 3.5 Density of states plot near E_F for pure carbon, from [1-22].

3.3 POWDER X-RAY DIFFRACTION

Powder X-ray diffraction patterns were collected using a Phillips PW 1730 X-ray generator and a diffracted beam monochromator. The X-ray generator was equipped with a copper target X-ray tube. Its wavelength originates from the Cu K-α line and is 1.54178Å. The resolution of the equipment is about 0.15° in scattering angle. Narrow slits were used (0.25° as the incident slit and 0.1mm as the outgoing slit) to achieve high scanning precision even at low scattering angles. The scans were all taken from 5° to 120° (2θ) at 0.2° steps. Overnight scans with 80 seconds count time per step were chosen to give good signal to noise ratio over the whole range of the spectrum.

The samples were scanned in a 2.5mm deep stainless steel X-ray holder, which was firmly packed with the carbonaceous material, the top surface being smoothed with a glass slide. For some samples with not enough powder to fill the holder, a thin, level layer of powder was applied to an off axis cut, zero background silicon wafer. A very thin layer of Dow Corning high vacuum grease was used to make the powder adhere to the silicon. Corrections for the peak width of these samples had to be made. The peak width for all samples is mainly due to the disorder in the samples but is also affected by the holder geometry as well. Broadened, slightly asymmetric Bragg peaks are observed for thick samples, as X-rays scattered from the top layers of the sample are not attenuated by the material. The intensities of X-rays scattered from layers at depth d in the sample will be reduced, however, by:

$$I(d) = I_o * \exp(-2\mu d/\sin\theta) \qquad \text{(eq. 3.7)}$$

where μ is the linear absorption coefficient of the material and θ is the angle between the X-ray beam and the sample surface. The X-rays scattered at depth d are also observed at a slightly different angle, θ', than those scattered from the top layer of the sample. This is caused by the extra depth, d, the beam has to penetrate into the sample, as schematically drawn in Figure 3.6. It then scatters at a different position in the x-direction in the sample and is observed by the detector under a slightly shifted angle compared to the beam scattered off the top layer of the sample. The angle of observation for X-rays scattered at depth d is:

$$\theta'(d) = \theta - d\cos\theta / L_o \qquad \text{(eq. 3.8)}$$

where L_o is the goniometer arm length.

Therefore, we expect peaks with a broadened flank towards low angle and an increased peak width compared to peaks measured on thin samples. From reference materials prepared from benzene a difference of 0.25^o in peak width between the scans on the silicon (sharper peaks) and scans of material in the deep holder (wider peaks) was determined. This correction of 0.25^o was applied to all peak width data, obtained using the silicon wafer.

All X-ray data was corrected for the atomic scattering factor of carbon (referred to as: $f(\theta)^2$) [3-10] and for the Lorentz factor (referred to as: $L(\theta)$) [3-11]. Measured powder X-ray patterns are the product of many different contributions, the atomic scattering factor, the Lorentz factor, the structure factor of the material (our primary interest) and other corrections such as the influence of the holder geometry. The actual interest in the X-ray data is to extract the structure factor, which is peaked at reciprocal space lattice positions and thus gives us the real space information as well. For example, the peak around 26° in the carbon diffraction pattern is associated with the layer spacing in the c-axis direction of the carbon material.

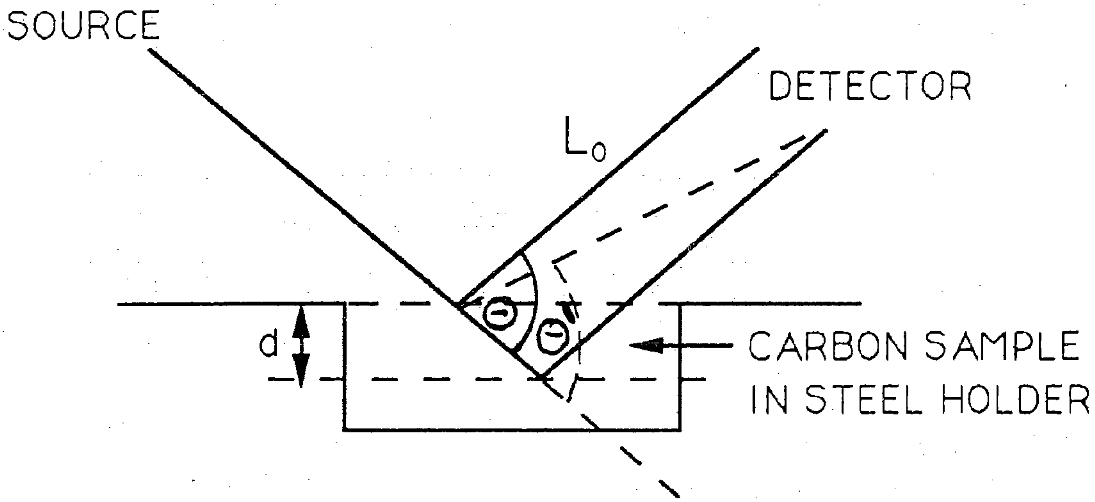

Fig. 3.6 Geometry of the X-ray diffraction setup showing the shift of scattering angle due to sample thickness.

To obtain the peaks in the structure factor, we have to correct the data for all other contributions. Otherwise incorrect peak positions for the broad (002) peak and thus wrong lattice spacings for the material would be obtained [3-11]. These corrections were made in agreement with theoretical calculations. The effect of these corrections is strongest for the broad peaks (broader than 2°) and especially for those at low scattering angle. The atomic scattering factor and Lorentz factor contributions get smaller for larger angle as can be seen in Figure 3.7, where we plot the two correction functions, $f(\theta)^2$ and $L(\theta)$, and their product $f(\theta)^2 \circ L(\theta)$ (not to scale), as a function of scattering angle. Thus a correction of the data is essential as we are mainly interested in the (002) peak.

The (002) peaks were fitted using a simple fitting program with four fitting parameters: peak area, peak position, half width at half maximum and a Lorentzian / Gaussian weighting function. We only used the data from 15° to 35° (2θ) as data for the fitting routine. The fits were not perfect as can be seen from Figure 3.8, where we plot raw data (corrected for $f(\theta)^2$ and $L(\theta)$ as described above) and a fit for the (002) peak of the acetonitrile 950°C sample. The divergence of the fit from the data is due to the asymmetric peak shape as described above. Accepting the asymmetry as a systematic error that is incorporated in the data for all samples, we fitted all data sets using this one-peak fitting routine. The fit to data correlation is very much the same for all fits, and we believe the peak width can be reliably extracted.

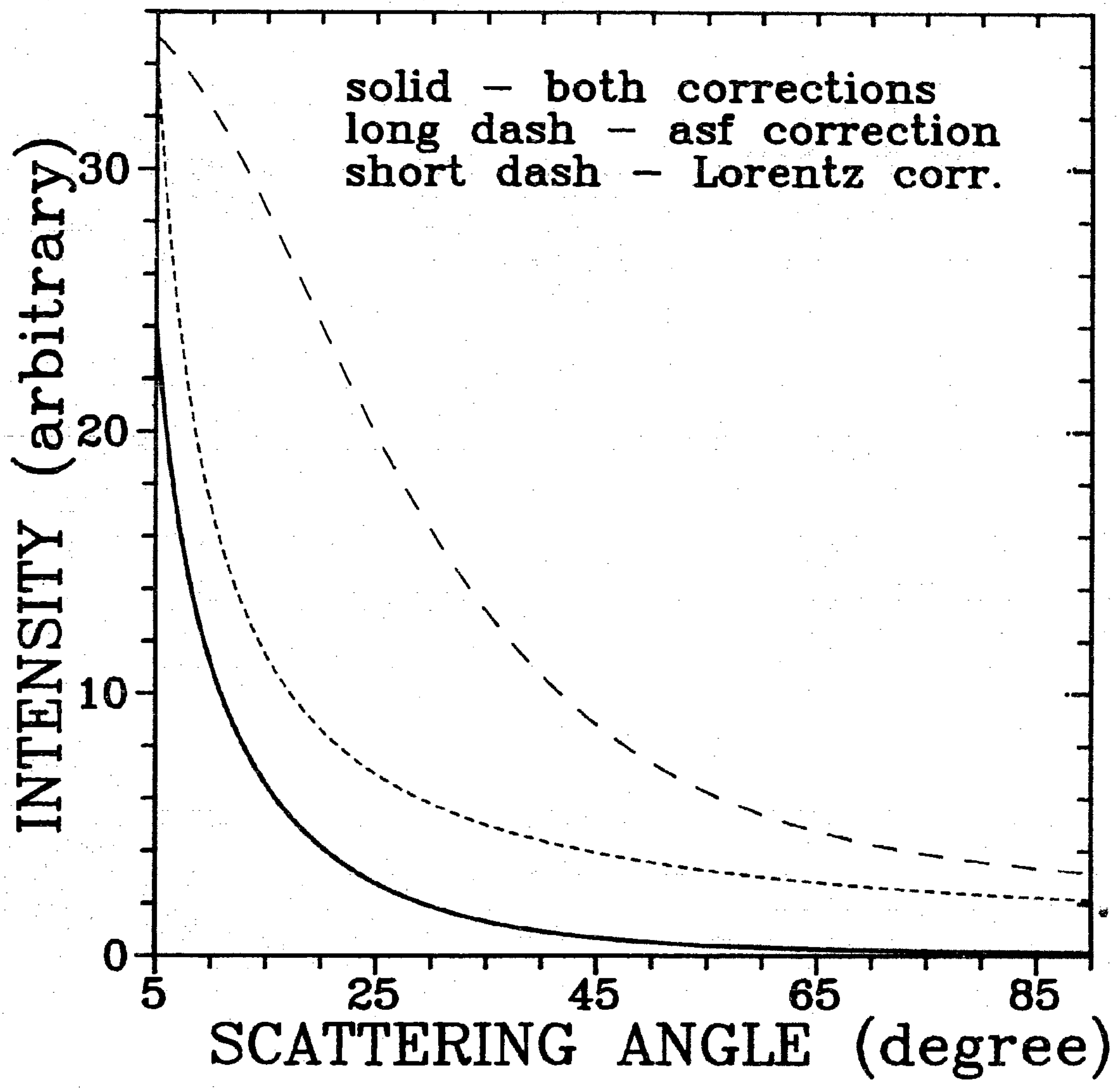

Fig. 3.7 Lorentz correction function and atomic scattering factor correction function, as well as their product (not to scale), graphed vs. scattering angle (2θ).

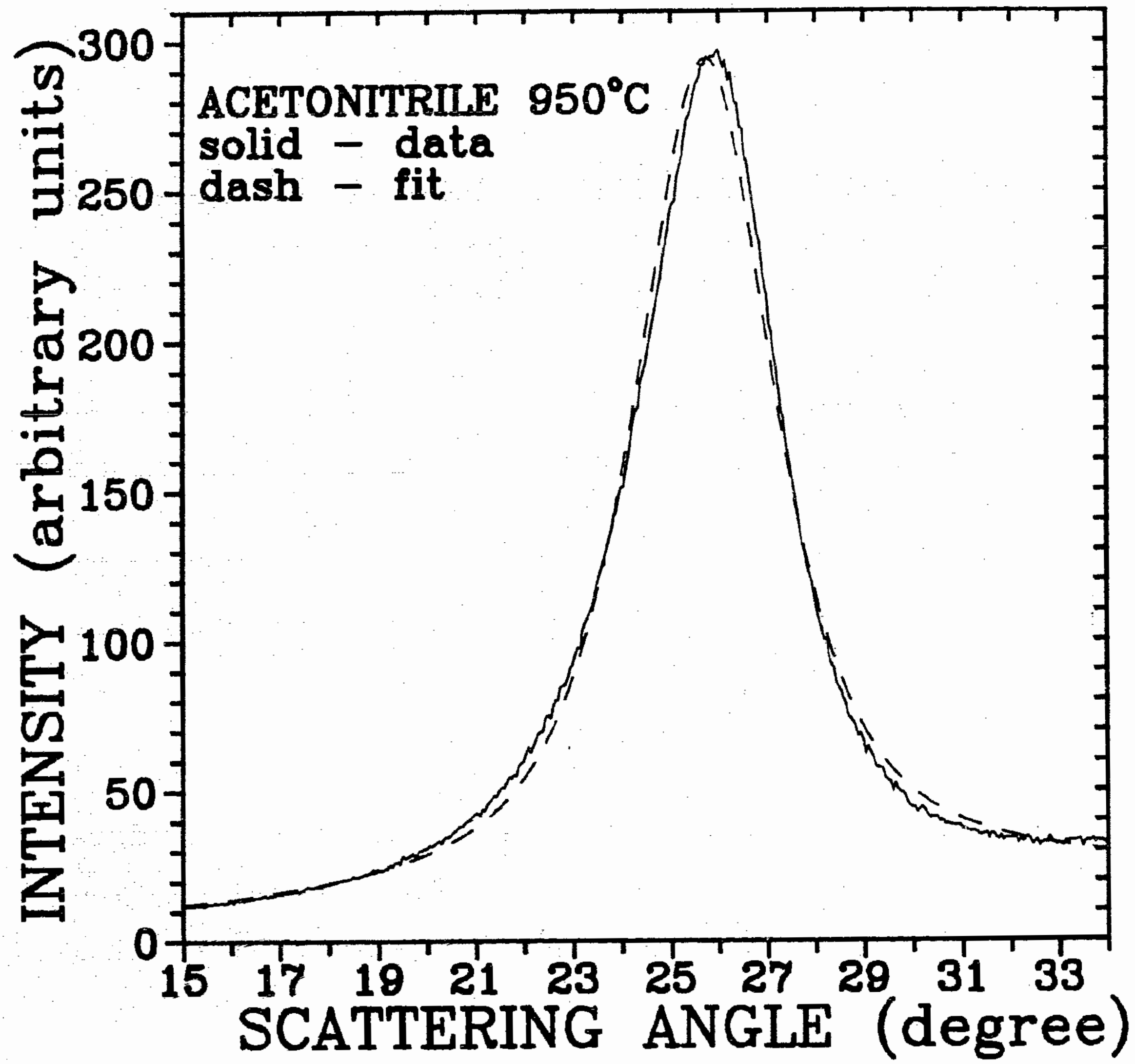

Fig. 3.8 Peak fit for the (002) Bragg peak, obtained from the fitting program described in the text, and raw data for acetonitrile 950°C sample x-ray diffraction data.

3.4 AUGER ELECTRON SPECTROSCOPY

Auger electron spectroscopy (AES) was performed using a Physical Electronics Industries Inc., Scanning Auger Microprobe PHI Model 25-120 spectrometer. AES is a semi quantitative technique to measure the elemental composition of a material. AES is based on the Auger process, which is an atomic process involving three electrons. An electron beam with a well defined energy, in our case, 3keV, is focused onto the sample. The electron beam ejects core electrons with binding energy E_b from the core of the atom. The hole left in the core is then filled by an internal process. A second electron from a different level with energy E_{s1} falls into the core hole. The energy released in this process is transferred to a third electron from a level with energy E_{s2}, often equal to E_{s1}, which leaves the atom. This electron is the Auger electron which has a very element specific energy, the Auger energy E_a. It can easily be calculated:

$$E_a = E_{s1} + E_{s2} - E_b \qquad \text{(eq. 3.9)}$$

The common processes are KLL, LMM and MNN, where the letters describe the three shells from which the electrons originate. The first letter describes the core shell of the electron that initially left the atom. The second letter refers to the shell of the electron that filled the core hole and the third letter refers to the shell from which the Auger electron originated.

The characteristic Auger energies of carbon and nitrogen are 272eV and 379eV respectively. The peak positions determine the elements present and the peak heights determine the relative concentrations of the particular elements. For better determination of the peak heights, the original data is differentiated [3-12].

The scans were taken on battery electrodes as prepared in Section 2.5. Prior to measurement the samples were sputtered with argon for 5 minutes at 3kV with a current of 20μA to remove surface adsorbents as much as possible and sputter away some of the binder material that covers the carbonaceous flakes. The area around the two peaks for carbon (245eV to 275eV) and nitrogen (372eV to 392eV) was scanned in 0.5eV steps. To gain a better signal to noise ratio for the low intensity nitrogen peak (only 2%-9% by weight of the sample material), it was scanned 30 times per cycle whereas the carbon peak was only scanned once per cycle. A single measurement consisted of 50 cycles.

Figures 3.9 and 3.10 show the differentiated Auger scans for the carbon and nitrogen edges respectively of the reference cathode made from the actetonitrile 950^{o}C sample. Peak heights are determined from the scans by taking the difference in counts between the maximum count value (at 249.5eV for the carbon edge and at 376eV for the nitrogen edge) and the minimum count value (at 272.5eV for the carbon edge and at 384eV for the nitrogen edge). The peak heights for each element, corrected for the relative Auger intensities for the element, are a quantitative measure for the composition of the samples with respect to these two elements [3-13].

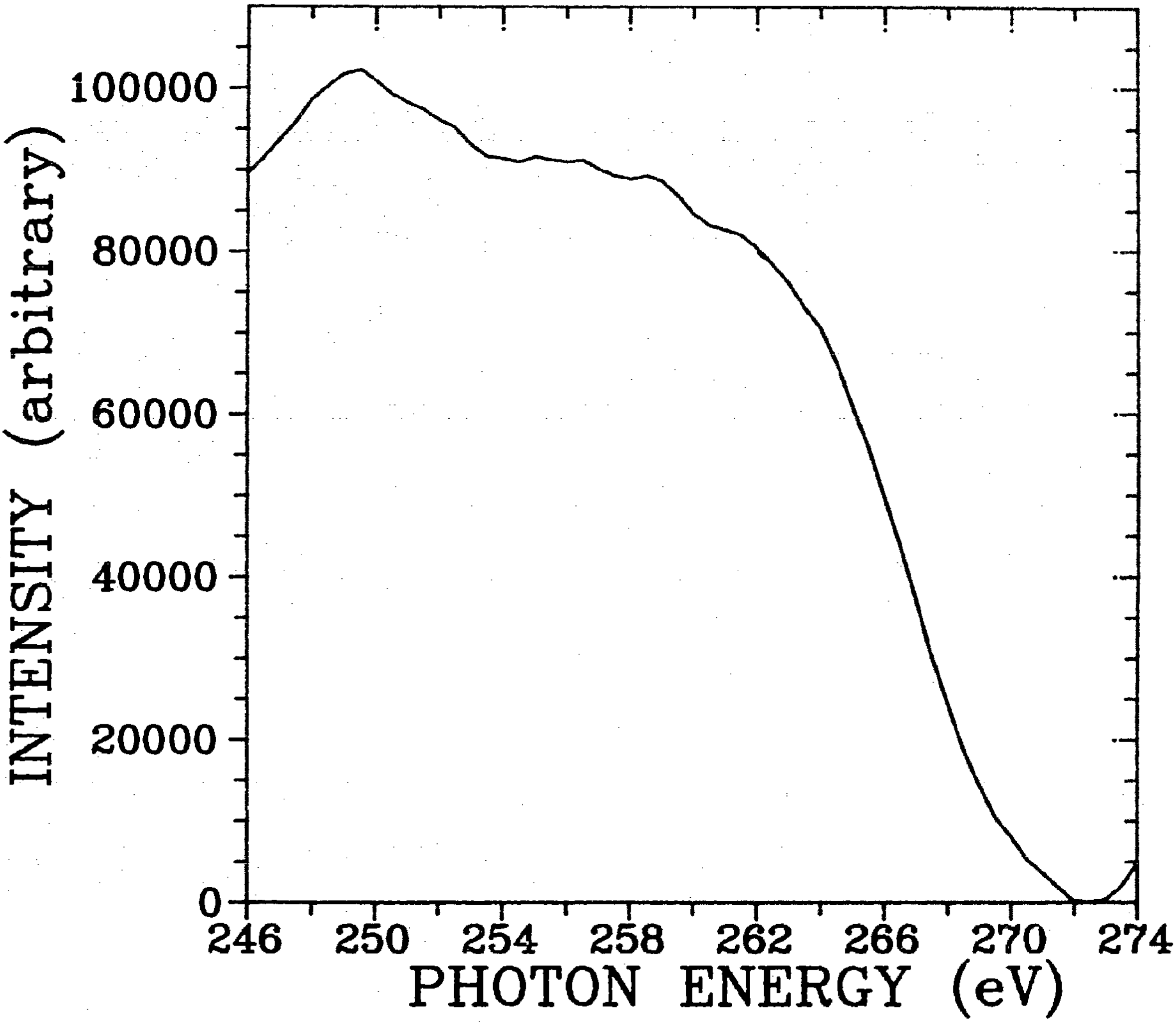

Fig.3.9 Auger scan (differentiated data) of the carbon edge for the reference cathode made from the acetonitrile 950°C material.

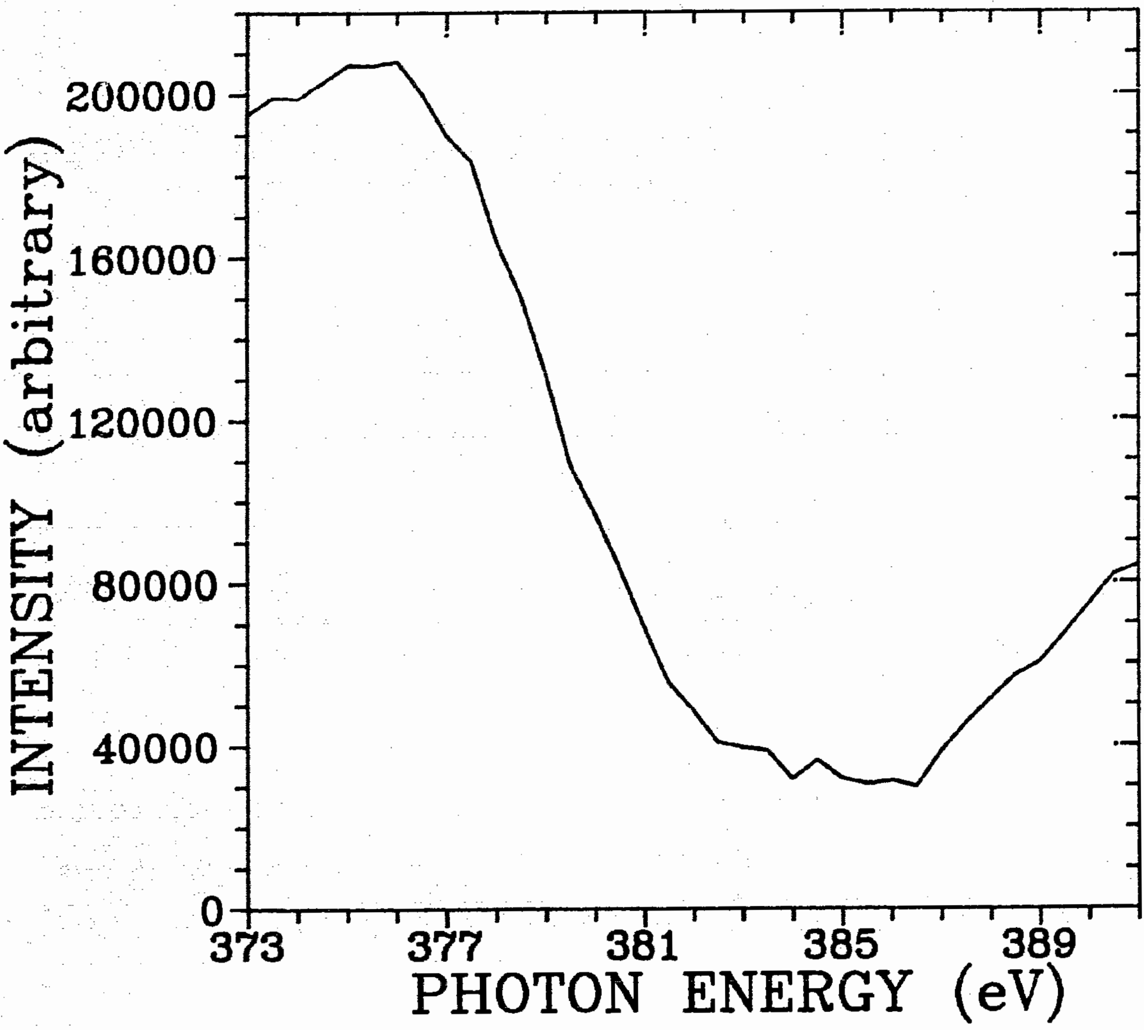

Fig. 3.10 Auger scan (differentiated data) of the nitrogen edge for the reference cathode made from the acetonitrile 950°C material.

The peaks for oxygen and fluorine, introduced by the binder, will not be considered here. The percentage of carbon in the material as measured by AES is expected to be higher than the percentage of carbon obtained from chemical analysis. This is so, since we used cathodes for AES analysis and not the originally as prepared powders. Cathodes contain the binder material which consists mainly of carbon and does not contain nitrogen. It also coats the original material and is hard to sputter off. Thus more carbon compared to nitrogen will be detected by AES and the percentage of nitrogen is expected to be less in AES data compared to chemical analysis data. This statement is supported by the AES measurement on as-made powder material, pressed into indium foil. The unprocessed material showed about 30% more nitrogen compared to an as-prepared battery cathode of the same material.

Battery cathodes were first used in cells and cycled to certain specifications that will be described in Chapter 5 together with the results. Then the fully charged cells (all reversibly intercalated lithium is removed) were taken apart and the carbon cathodes were recovered. They were rinsed in methanol for 24 hours to wash out all soluble reaction products from the reaction of lithium with the chemically active nitrogen containing species in the carbonaceous material. Other solvants could have been tried, which might dissolve these chemical nitrogen species better. After drying in an oven at 105°C for an hour they were brought into the Auger system and scanned. The reference cathode, that had not been cycled in a cell, was rinsed and dried the same way. To scan the original powder material as a comparison to cathode material, it was pressed into indium foil and scanned likewise.

CHAPTER FOUR: ANALYSIS AND RESULTS

4.1 MATERIAL ANALYSIS DATA

4.1.1 Chemical Analysis Results

The results of chemical analysis (Table 1) show that nitrogen is incorporated into all samples made from nitrogen containing precursors. The samples pyrolyzed from acetonitrile and pyridine show a dependence of nitrogen content on the deposition temperature as can be seen in Figure 4.1. With falling deposition temperature, the nitrogen content of the prepared material rises. The acetonitrile 850°C sample also shows the highest overall nitrogen content of any of the samples. The samples pyridine 1000°C, pyridine 1050°C and $C_2H_2:NH_3(1:1)$ 900°C show the lowest nitrogen content of all samples. All samples produced from acetylene and ammonia show, within the error of ±0.3%, no dependence of nitrogen content on deposition temperature. The nitrogen content for these samples only varies with the flow rate ratio of acetylene and ammonia in the reactant gas mixture.

Both the benzene 900°C and 1050°C samples showed no detectable nitrogen. The only difference between them was the much higher carbon content of 99.70% for the benzene 1050°C powder over the benzene 900°C powder, which contained only 98.43% carbon. This is due to the loss of hydrogen in that temperature range, which was discussed in Section 1.2.

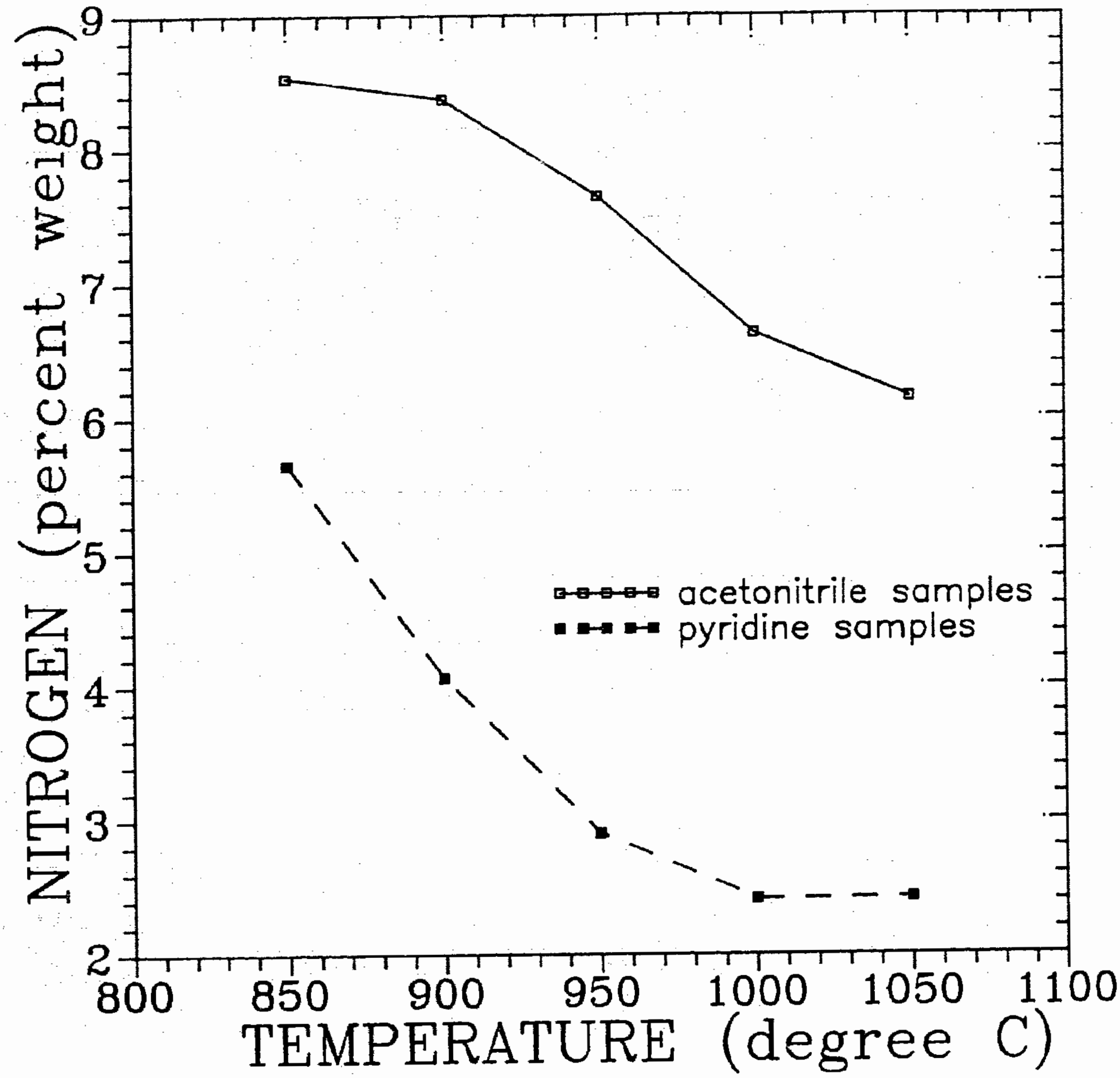

Fig. 4.1 Temperature dependence of nitrogen content in the material for samples prepared from acetonitrile and pyridine.

Sample	percent N by weight	percent H by weight	average irrev. capac. in mAh/g	# of cells used for average irrev. capac.
benzene 850	n.a.	n.a.	57	1
benzene 900	<0.1	0.44	30	1
benzene 950	n.a.	n.a.	50	1
benzene 1000	n.a.	n.a.	28	1
benzene 1050	<0.1	<0.1	17	1
aceto 850	8.53	1.51	n.a.	n.a.
aceto 900	8.37	0.42	183	2
aceto 950	7.64	0.38	149	4
aceto 1000	6.62	0.30	113	1
aceto 1050	6.14	<0.1	111	2
pyridine 850	5.65	0.34	119	2
pyridine 900	4.06	0.30	99	2
pyridine 950	2.90	0.22	72	2
pyridine 1000	2.41	<0.1	69	5
pyridine 1050	2.42	<0.1	102	2
$C_2H_2:NH_3$ (1:1) 900	2.91	1.27	139	1
$C_2H_2:NH_3$ (1:1) 950	2.96	0.37	166	1
$C_2H_2:NH_3$ (1:1) 1000	3.18	0.29	59	1
$C_2H_2:NH_3$ (2:3) 900	3.62	0.57	127	2
$C_2H_2:NH_3$ (2:3) 950	3.75	0.34	85	1
$C_2H_2:NH_3$ (2:3) 1000	3.55	0.44	128	2

Error on all above nitrogen and hydrogen values: ±0.3

Table 1 showing nitrogen and hydrogen content in weight % as well as irreversible capacities in mAh/g for materials made from benzene (as a reference), acetonitrile (aceto), pyridine and 1:1/2:3 mixture of acetylene and ammonia ($C_2H_2:NH_3$ (1:1) and $C_2H_2:NH_3$ (2:3) respectively). The specified numbers behind the materials are the temperatures in °C at which the materials were produced.

4.1.2 X-ray Diffraction Results

Now we must determine how the nitrogen is incorporated in the material, as bonded substituent chemical groups 'external' to the graphite honeycomb, or as a substitutional dopant, directly replacing a carbon atom in the graphite structure. Earlier references have proven this to be a difficult task, as an example see [4-1]. We expect that if the nitrogen is substitutional, it will most likely affect the lattice constants and other properties of the carbonaceous materials.

The lattice constants and crystallite size of carbon prepared near 1000°C depend strongly on the heat treatment temperature [4-2] which affects the degree of graphitization of the carbon as mentioned above. Substitutional boron greatly accelerates the graphitization process [4-3] for boron-carbons with the graphite structure prepared at 900°C. In [4-3] materials with up to 17% substitutional boron were prepared. This caused the (002) Bragg peak to shift from 25.3° for pure carbon to 26.7° for $B_{0.17}C_{0.83}$.

The presence of nitrogen in the deposition process slows down the deposition considerably. We will show below that the effect of substitutional nitrogen on the lattice constants appears to be weaker than for boron, although we are not sure how much of the total nitrogen in the material is, in fact, substitutional. Also, the amount of nitrogen in our samples is much less than the amount of boron in the boron containing materials to begin with.

Figure 4.2 shows the x-ray diffraction pattern for the acetonitrile 950°C sample. Four main peaks can be identified. The strongest of them is the (002) peak at approximately 25.5° scattering angle. This pattern is qualitatively similar to that of a carbon prepared from benzene at the same temperature, also shown in Figure 4.2.

To check for small differences between the samples with and without nitrogen, we plotted the (002) Bragg peak positions for all samples (as obtained from the fitting program, described in Chapter 3.3) versus deposition temperature. Figure 4.3 shows that the incorporation of nitrogen leads to a small increase in the (002) peak position (maximum 0.5°) compared to the samples prepared from benzene. The shift is strongest for the acetonitrile 900°C sample, which has the highest nitrogen content. A shift to higher angle can be related to smaller lattice spacing by the Bragg formula:

$$\lambda = 2\ d \sin(\theta)$$

where λ is the x-ray wavelength, θ is the Bragg angle and d is the layer spacing, or in this case 1/2 the lattice spacing, as we are referring to the (002) peaks.

Incorporated nitrogen apparently causes the spacing between adjacent carbon sheets to decrease. This decrease is also roughly

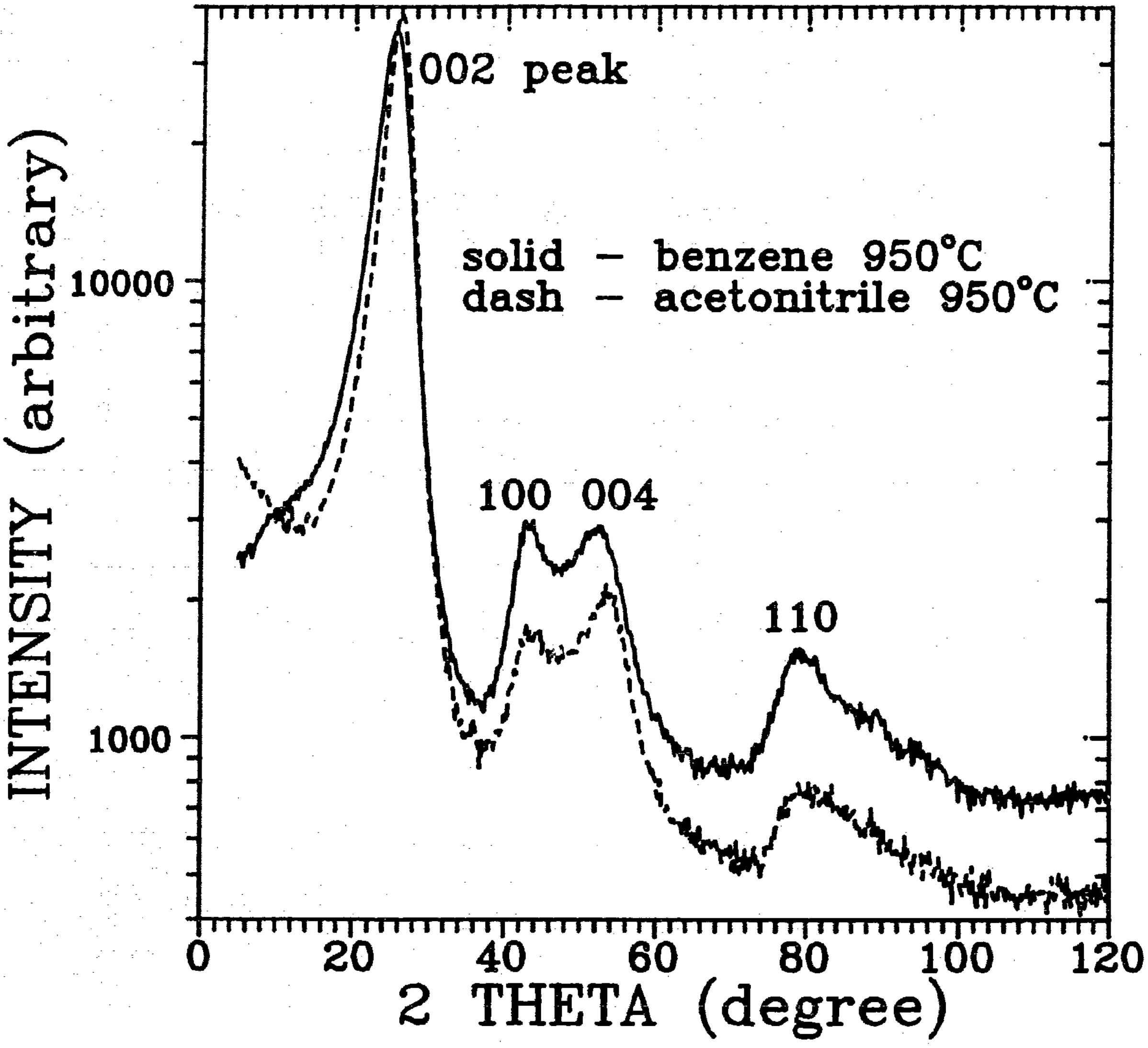

Fig. 4.2 X-ray diffraction pattern for acetonitrile 950°C and for benzene 950°C from 5° to 120° in scattering angle.

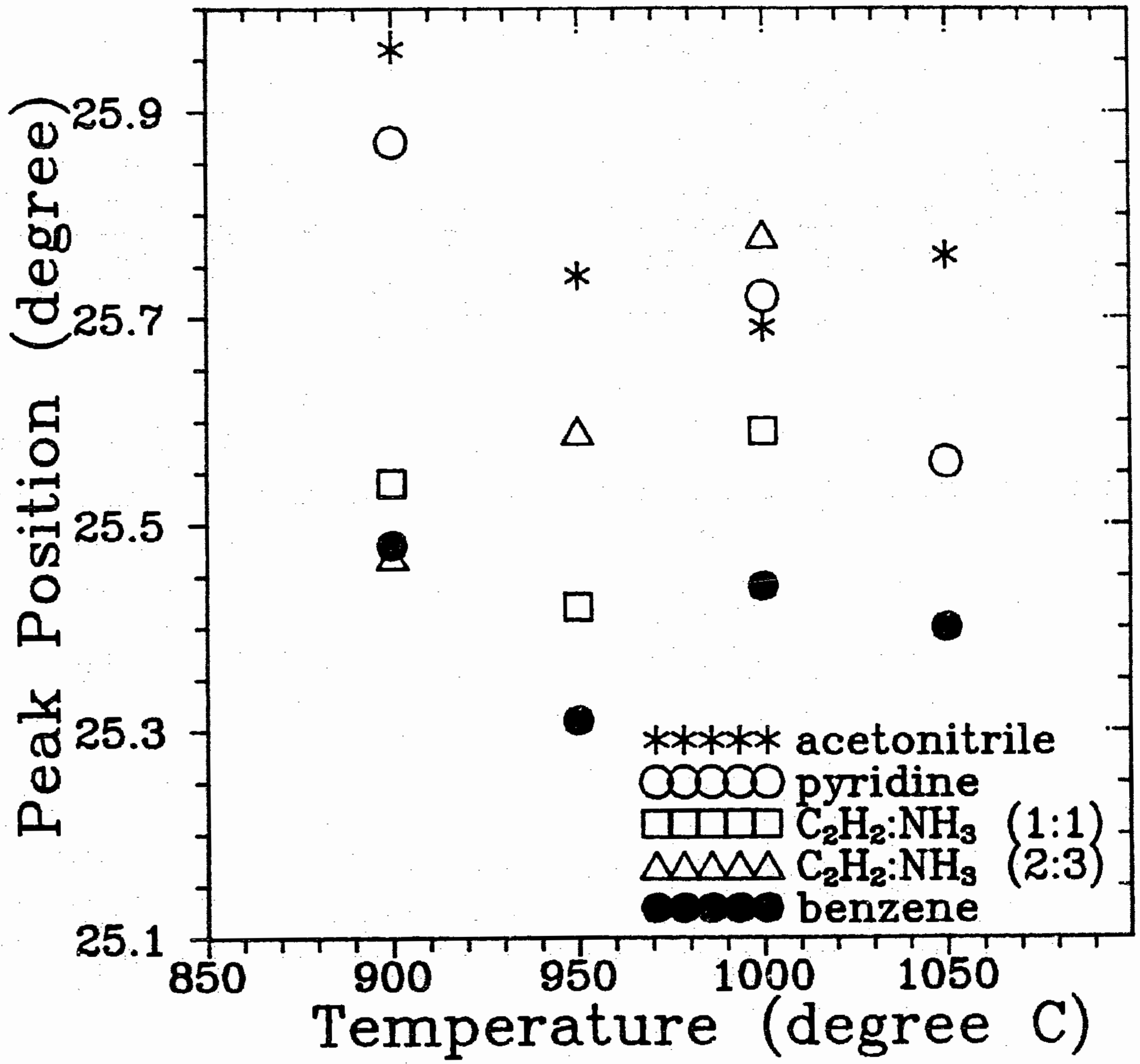

Fig. 4.3 Peak positions of the (002) Bragg peaks for all samples, obtained from the peak fitting program as described in the text.

proportional to the nitrogen content in the material. Figure 4.4 shows a graph of lattice spacing versus nitrogen content, calculated using Bragg's law. The reduction of lattice spacing is coupled with an increase in nitrogen content in the material (from $C_2H_2:NH_3$ (1:1) 900°C to acetonitrile 850°C).

Figure 4.5 shows the half width at half maximum of the (002) Bragg peaks versus heat treatment temperature for all the samples. Carbons prepared at low temperature usually have a broad (002) peak. The breadth is caused by a finite number of carbon layers which scatter x-rays coherently. The number of layers which scatter coherently determines the crystallinity of the carbon and is affected by the length of the particle in the c-axis direction (commonly called L_c) and by c-axis strain [1-19]. Figure 4.5 shows that carbons made from pyridine and benzene show similar broad peaks, which means they have low crystallinity. On the other hand the samples made from acetonitrile or acetylene and ammonia show sharper peaks and thus are more crystalline when prepared at the same temperature. The growth mechanism for carbons pyrolyzed from aromatic molecules (e.g. benzene and pyridine) is apparently different from the deposition mechanism for short, straight-chain molecules (acetylene and acetonitrile).

We can conclude that the incorporated nitrogen changes the structure of the material. For example, samples prepared from pyridine and benzene have similar crystallinity, but different layer spacing, presumably due to the incorporated nitrogen.

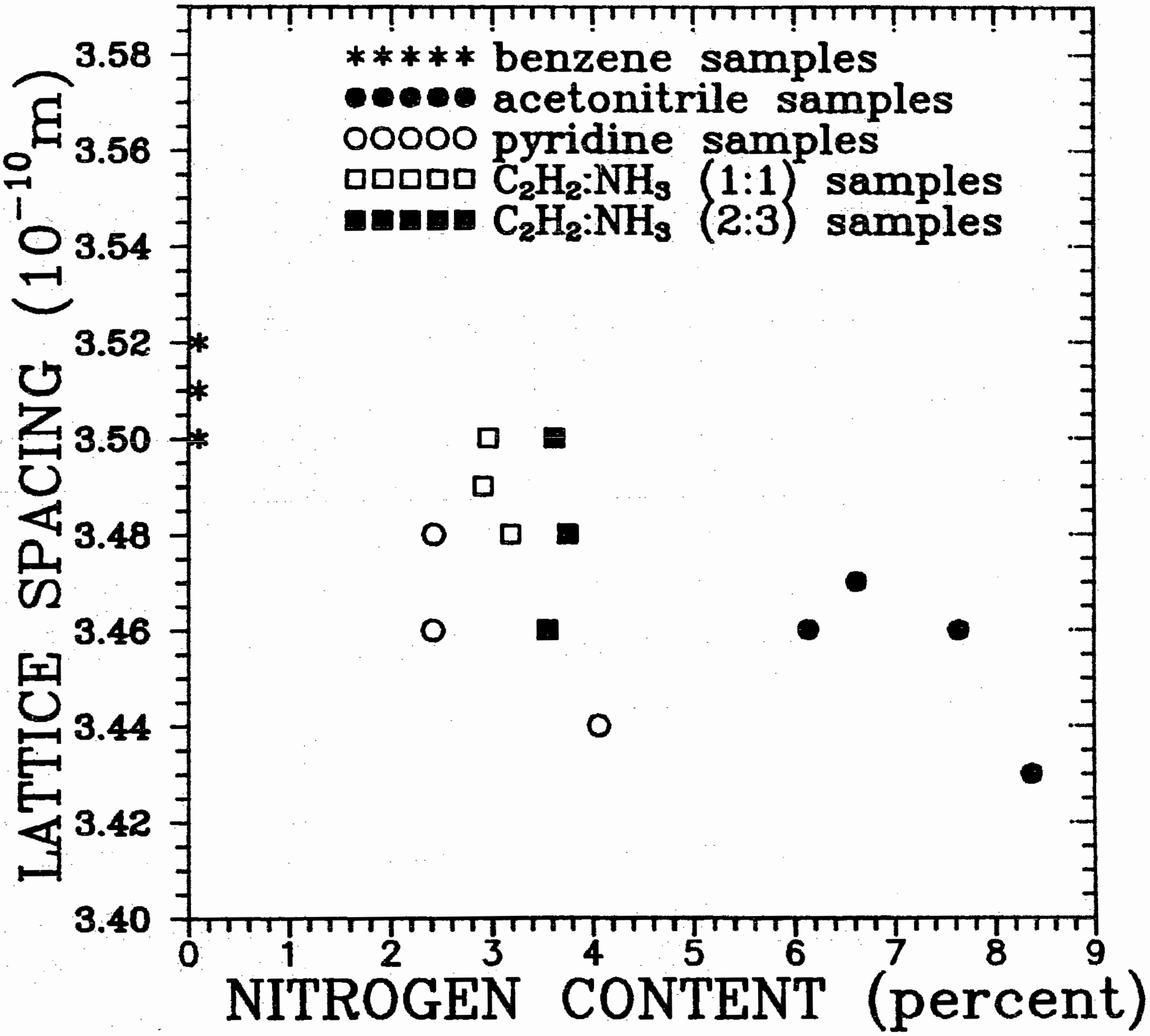

Fig. 4.4 Lattice spacing for all samples, obtained from the (002) peak positions from Fig. 4.3 using Braggs law.

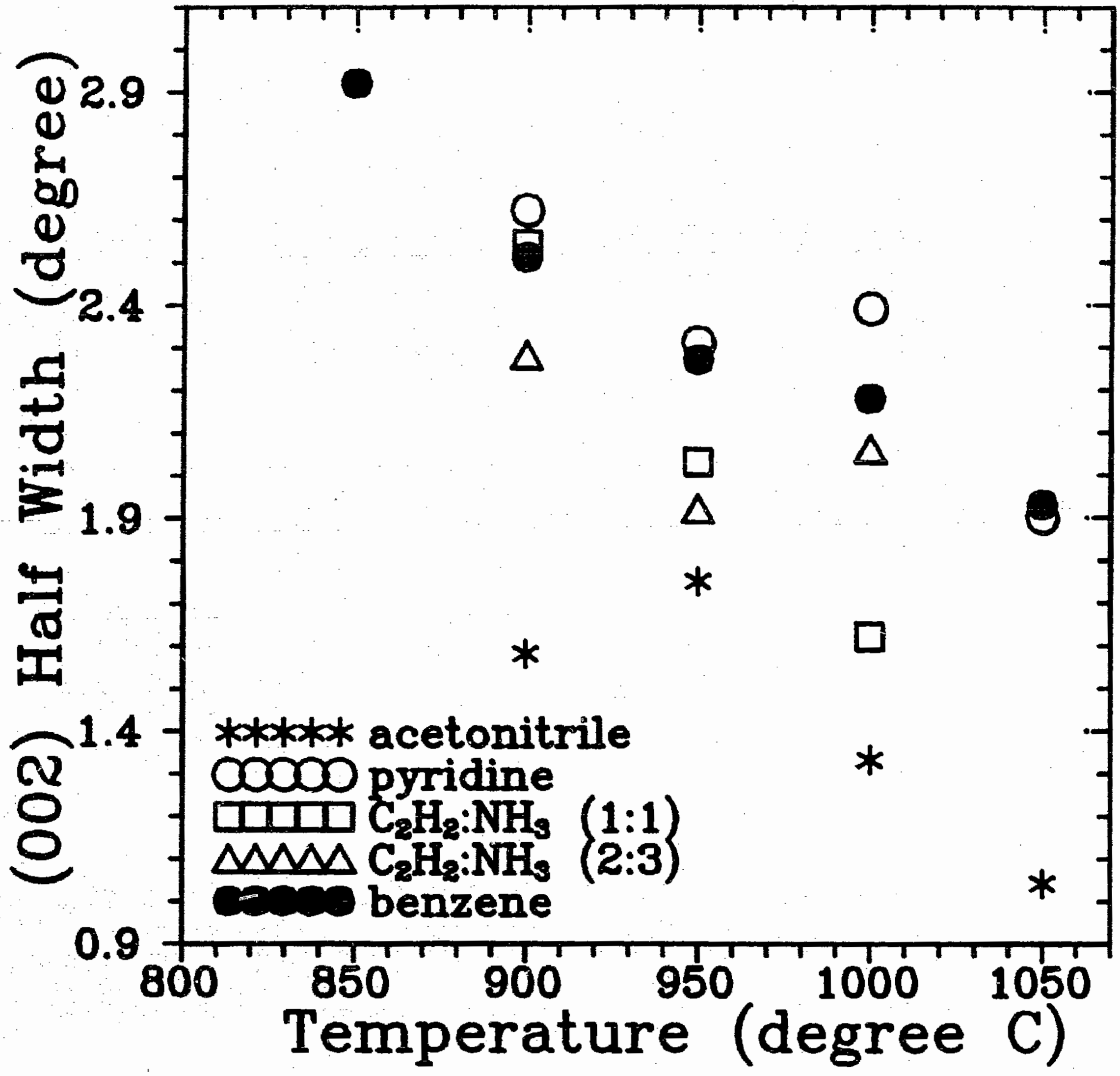

Fig. 4.5 Half width at half maximum of the (002) Bragg peak for all samples.

4.1.3 Angular Dependent X-ray Absorption Spectroscopy Results

The X-ray absorption spectrum (XAS) shown in Figure 4.6 is an overview scan from 280eV to 430eV for the acetonitrile 900°C sample at an angle of 59°. As defined before, this angle means that the beam is incident on the sample about 30° from the sample surface normal. The spectrum clearly shows the carbon absorption edge near 290eV (theoretical C 1s binding energy: 284.3eV) and the nitrogen absorption edge near 400eV (theoretical N 1s binding energy: 397.9eV). The first, sharper feature at both edges is the 'π^*-peak' where the second, broader shoulder is the 'σ^*-peak'. The nitrogen edge features are less intense than the carbon features, due to the comparatively low nitrogen content in the sample.

From the relative peak heights of the π^*-peaks for carbon and nitrogen, we can also calculate the amount of nitrogen in the material. For a given angle we obtain the amount of nitrogen, which has the same absorption characteristics as the carbon at that angle. Taking the atomic subshell photoionization cross sections for carbon at photon energy 285eV (8×10^{-3}Mb) and the equivalent cross section for nitrogen at 398 eV (9×10^{-3}Mb) into consideration [4-4], we find the nitrogen content in the material to be 8.7%±1.0%. The error is large, due to the inaccurate peak height determination, especially for the nitrogen π^*-peak. This nitrogen content compares well with the 8.37%±0.3%, obtained from chemical analysis of the same material.

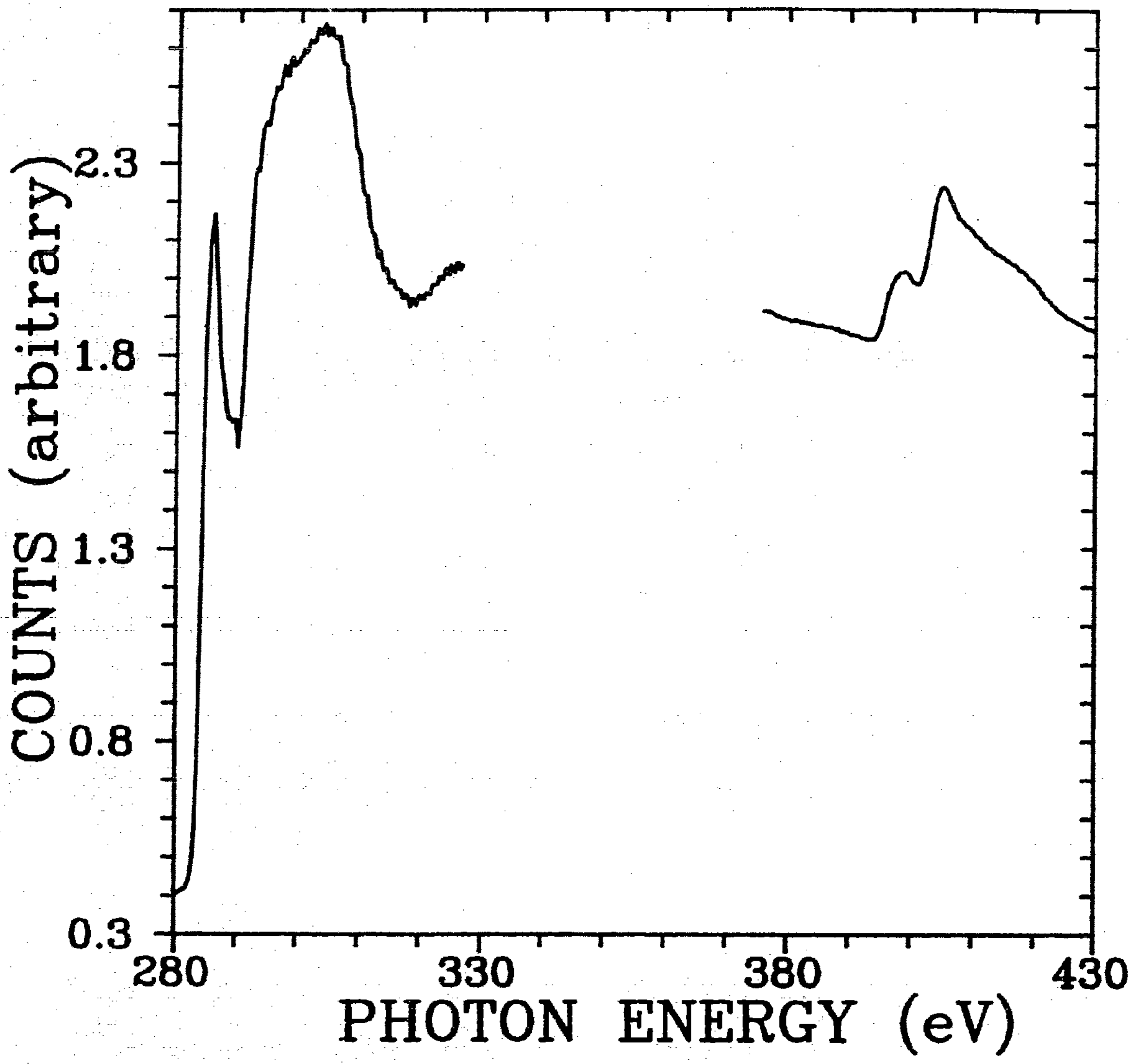

Fig. 4.6 XAS overview spectrum from 280eV to 430eV for the acetonitrile 900°C sample. The scan shows the carbon and nitrogen edge for this sample taken at 59° angle between the photon beam and the sample surface.

As shown in Figure 3.4 in Section 3.2, the π^* and σ^* peaks of highly oriented pyrolytic graphite (HOPG) samples show an angular dependence. We do not expect as perfect angular dependence as demonstrated in Figure 3.3 for our samples, due to the orientational disorder of the flaky powders, but hope to see the same trends with variation of angle. For all scans described below the incident beam energy was scanned from 280eV to 325eV for the carbon absorption edge and from 392eV to 430eV for the nitrogen absorption edge. All raw data was corrected for the respective I_o as described in Section 3.2.

Figure 4.7 shows an XAS scan at the carbon edge for the acetonitrile 950°C sample. The data has been collected at 90° (normal incidence), 59° and 30°, between the incident photon beam and the flat sample surface. When the photon beam is perpendicular to the graphite layers, transitions from the 1s core level to unfilled π^*-bands at the conduction band edge are forbidden [3-6], as described in Chapter 3.2. As the angle decreases towards 0°, transitions to the π^*-bands (sharper feature at about 285eV) become stronger whereas transitions to σ^*-bands (broader shoulder from about 292eV to 307eV) become weaker [3-6]. This general trend is observed in our data, except that the π^*-band contribution can still be observed at normal incidence because our powder samples were not perfectly oriented with their honeycomb layers in the plane of the substrate. The ratio of the π^*-peak height to the σ^*-peak varies from about 1:1 at normal incidence to 3.5:1 when the angle between the photon beam and the sample surface is 30°.

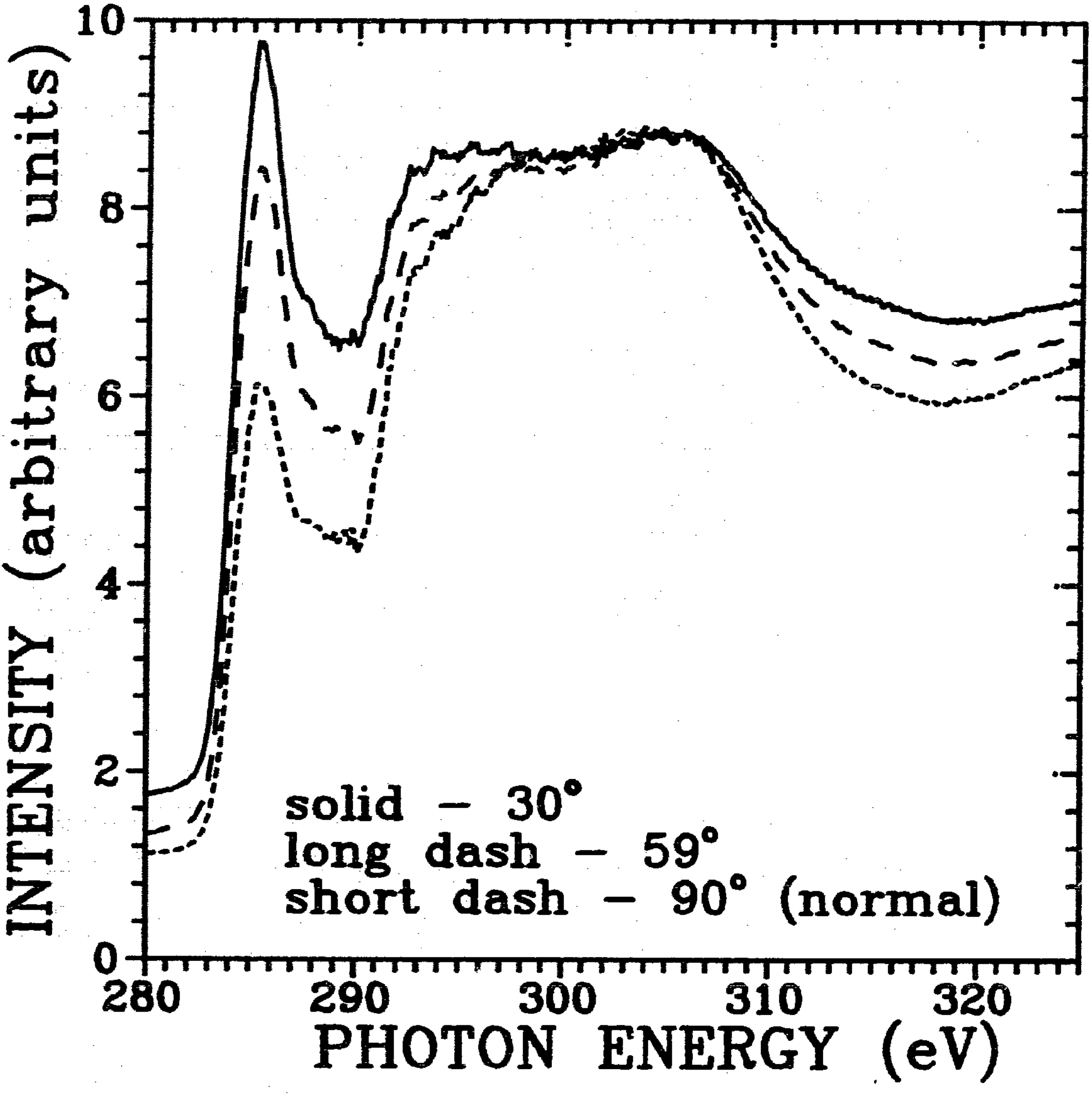

Fig. 4.7 XAS scan of the carbon absorption edge for acetonitrile 950°C taken at three different angles of the photon beam relative to the sample surface, 90° (normal), 59° and 30°.

If nitrogen is substitutional for carbon in these samples, we expect the XAS spectra at the nitrogen edge to show the same dependence on angle as the carbon edge spectra. Figure 4.8 shows the nitrogen edge measured on the same sample as used for Figure 4.7 at the same three angles. Again, the intensity of the π^*-peak (~ 399eV) relative to the σ^*-shoulder (~ 405eV) grows as the angle of the photon beam approaches grazing incidence. The ratio of the π^*-peak to the σ^*-peak changes from about 1:2 at normal incidence to about 3:2 at 30^o. This 3 fold increase is similar to the 3.5 fold increase observed at the carbon edge.

Scans on the other materials prepared from pyridine or acetylene and ammonia yielded similar results. They show the same type of angular dependence for the carbon and nitrogen edges.

The results above show that the nitrogen and carbon are in similar chemical environments in the material. The XAS results are consistent with substitutional nitrogen, although they do not prove that the nitrogen has substituted for carbon. Any flat, for example aromatic, molecule containing nitrogen which is bonded with its σ^*-orbitals parallel and π^*-orbitals perpendicular to the graphite layers will give rise to a dependence on angle consistent with that observed in Figure 4.8. Furthermore, nitrogen bonded differently in the sample, i.e. with the σ^*-orbitals not oriented in the plane parallel to the sample surface, would contribute to the π^*-peak, which does not vanish at 90^o incidence.

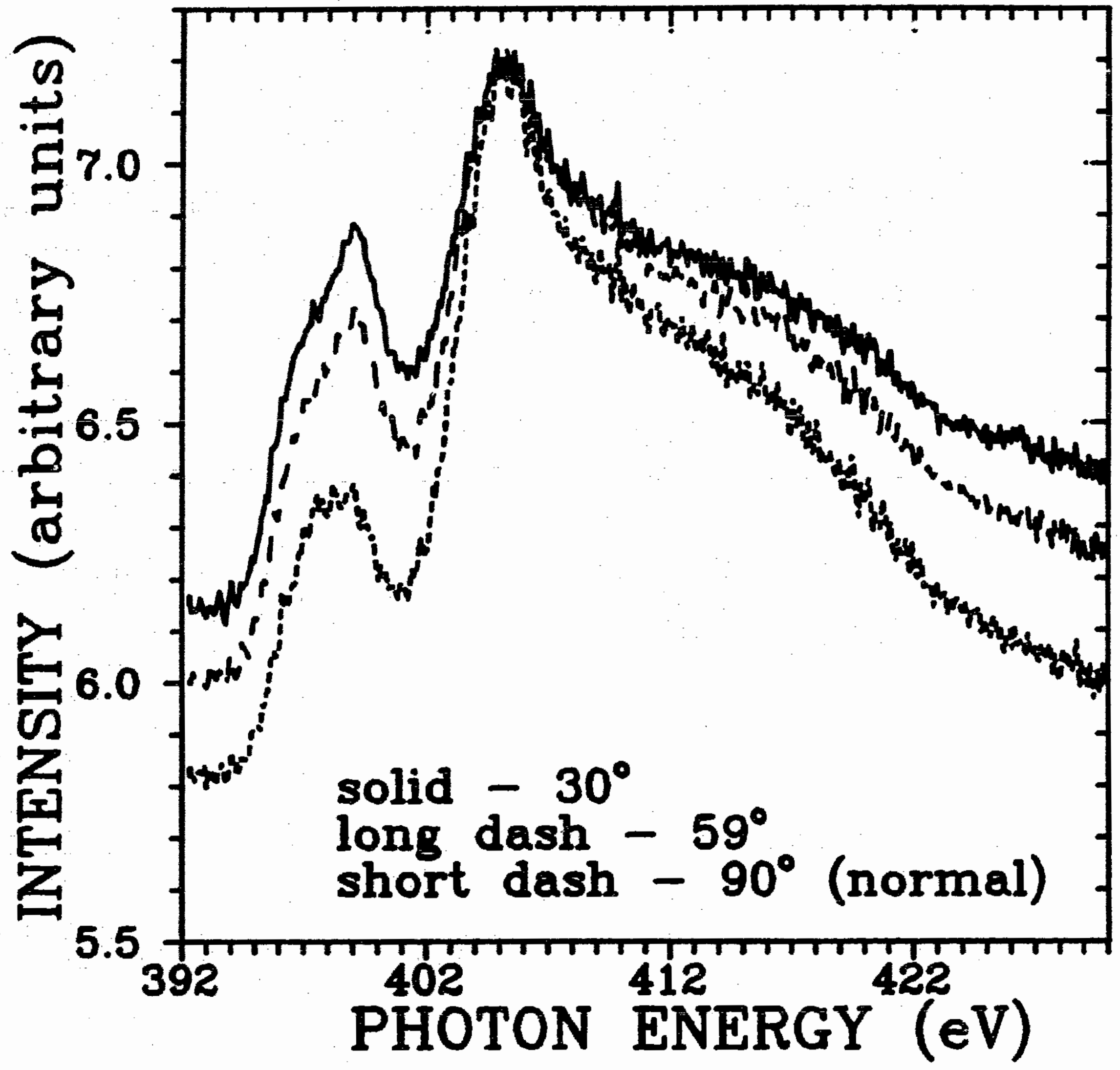

Fig. 4.8 XAS scan of the nitrogen edge for acetonitrile 950°C taken at three different angles of the photon beam relative to the sample surface, 90° (normal), 59° and 30°.

The chemical analysis shows, that the samples prepared from nitrogen containing precursors contain nitrogen up to 9% by weight of the material. X-ray diffraction studies show that nitrogen changes the properties of the material, indicating some substitutional nitrogen in the carbon. X-ray absorption studies are also consistent with the assumption of substitutional nitrogen. In conclusion it is most likely that at least some of the nitrogen in the material is substitutional for carbon within its honeycomb structure.

4.2 CELL DATA ANALYSIS

Electrochemical cells were built as described in Section 2.5 for all carbonaceous materials produced. We will present selected data from the cell experiments and try to understand the measured voltage curves. We found that the properties like lattice spacing and crystallinity of the carbonaceous materials change when nitrogen is substituted for carbon. The electrochemical properties are thus expected to change somewhat, due to the nitrogen in the material. The nitrogen has a drastic effect on certain cell properties associated with the capacity of the cells, as we will show below. They can be observed in the plots of cell voltage versus the amount of lithium, x, in the carbonaceous materials.

Figure 4.9 shows the cell voltage during the first cycle and the second discharge of a Li/(N_zC_{1-z}) cell containing N_zC_{1-z} prepared from the pyridine 850°C material. For all our cells the consecutive charge and discharge cycles map the second cycle very closely. The cell voltage, V, is plotted versus x in $Li_x(N_zC_{1-z})_6$ as described in Section 1.4. Data for a Li/Li_xC_6 cell with a pure carbon electrode prepared from benzene 850°C is shown for comparison. The inset in Figure 4.9 shows the derivative, dx/dV, plotted versus cell voltage for the same two cells. Even though dx/dV is always negative, we have made it positive for the charge part for clarity. Two features of this data are noteworthy: the 'irreversible capacity', seen on the first discharge, and the shape of the voltage profile around 1.0V.

4.2.1 Irreversible Capacity

For both cells the capacity associated with the first charge (removing lithium from the carbonaceous material, called deintercalation) is less than that of the first discharge (putting Li into the carbon, called intercalation). This means, that a certain amount of lithium, δx, remains in the carbon material, trapped or bound in some way, after the cell is completely charged up to 2.8V, our upper turnaround point. The difference in capacity, δx, generally called 'irreversible capacity', is associated with the formation of a passivating film on the surface of the carbon electrode particles [4-5] and with the consumption of chemical species on the carbon electrode which react with lithium. These reactions are only observed on the

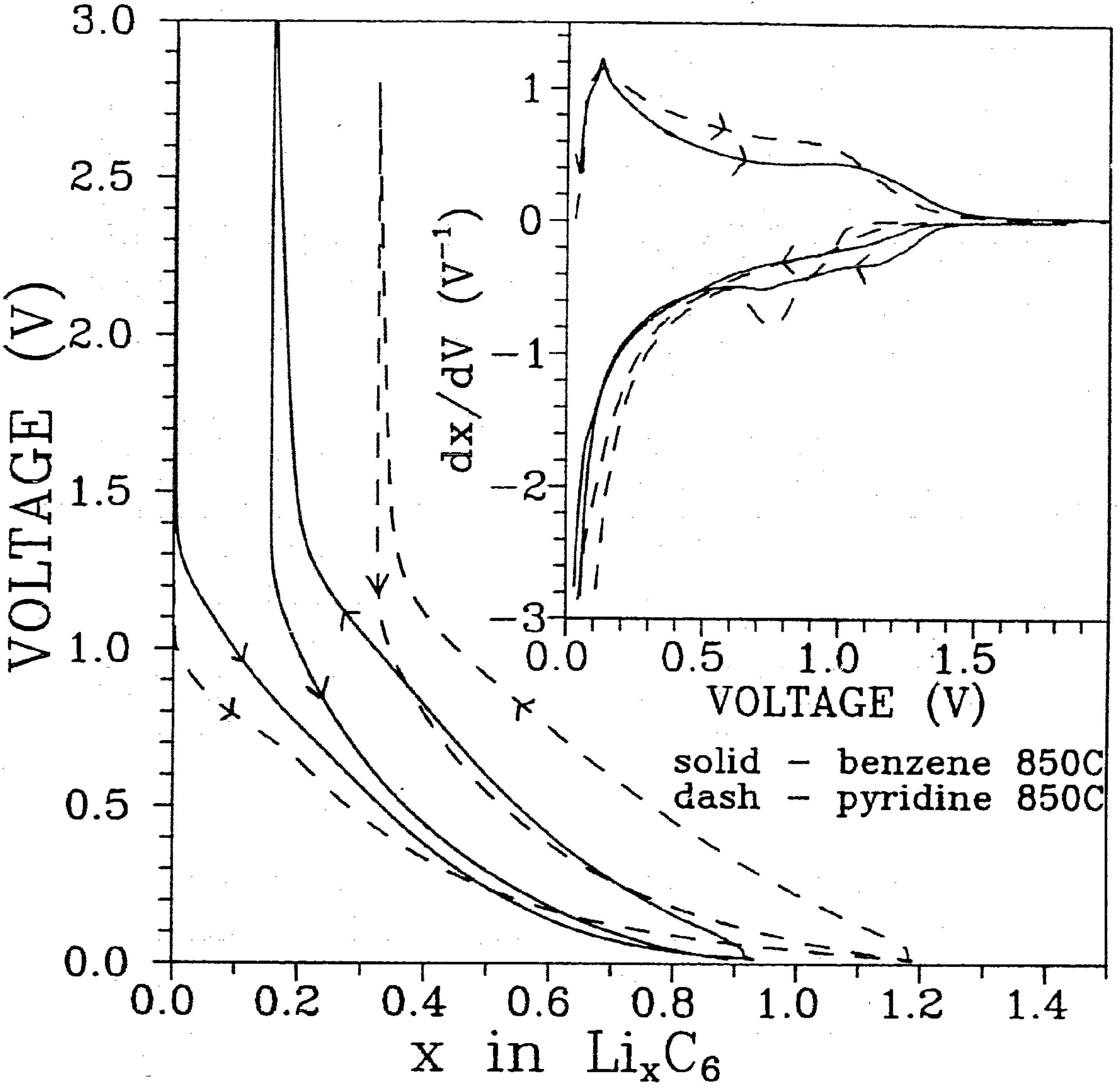

Fig. 4.9 Cell voltage profile, V(x), and dx/dV, for an acetonitrile 850°C cell and a benzene 850°C reference cell.

first discharge cycle but are a common phenomenon for lithium/carbon cells. They remove lithium from further reaction and thus are undesirable. Efforts are usually made to minimize the irreversible capacity of practical electrodes. The best test bench cells using graphite electrodes show irreversible capacities of about $\delta x=0.06$, which corresponds to a capacity loss of 22mAh/g.

We measured surface areas on selected samples and found that the surface areas, using the BET method [4-6], of our samples are of the order of 0.8-2.0m^2/g and are independent of nitrogen content in the material. The surface area of a specific sample seems to depend mainly on the grinding conditions of the sample. Figure 4.10 shows the surface area versus irreversible capacity, which clearly shows no correlation. The surface area for all our samples is low and independent of nitrogen content and thus surface area is not a major reason explaining the high irreversible capacities observed in our nitrogen containing samples. We can say that the larger irreversible capacity of the pyridine 850°C material (Figure 4.9) suggests that it contains more chemically reactive species that trap lithium on the first cell discharge. We are curious as to whether this is caused by the nitrogen contained in the sample.

Figure 4.11 shows cell voltage, V(x), for cells containing carbonaceous materials prepared from benzene, pyridine and acetonitrile at 900°C. The voltage curves for pyridine 900°C and acetonitrile 900°C

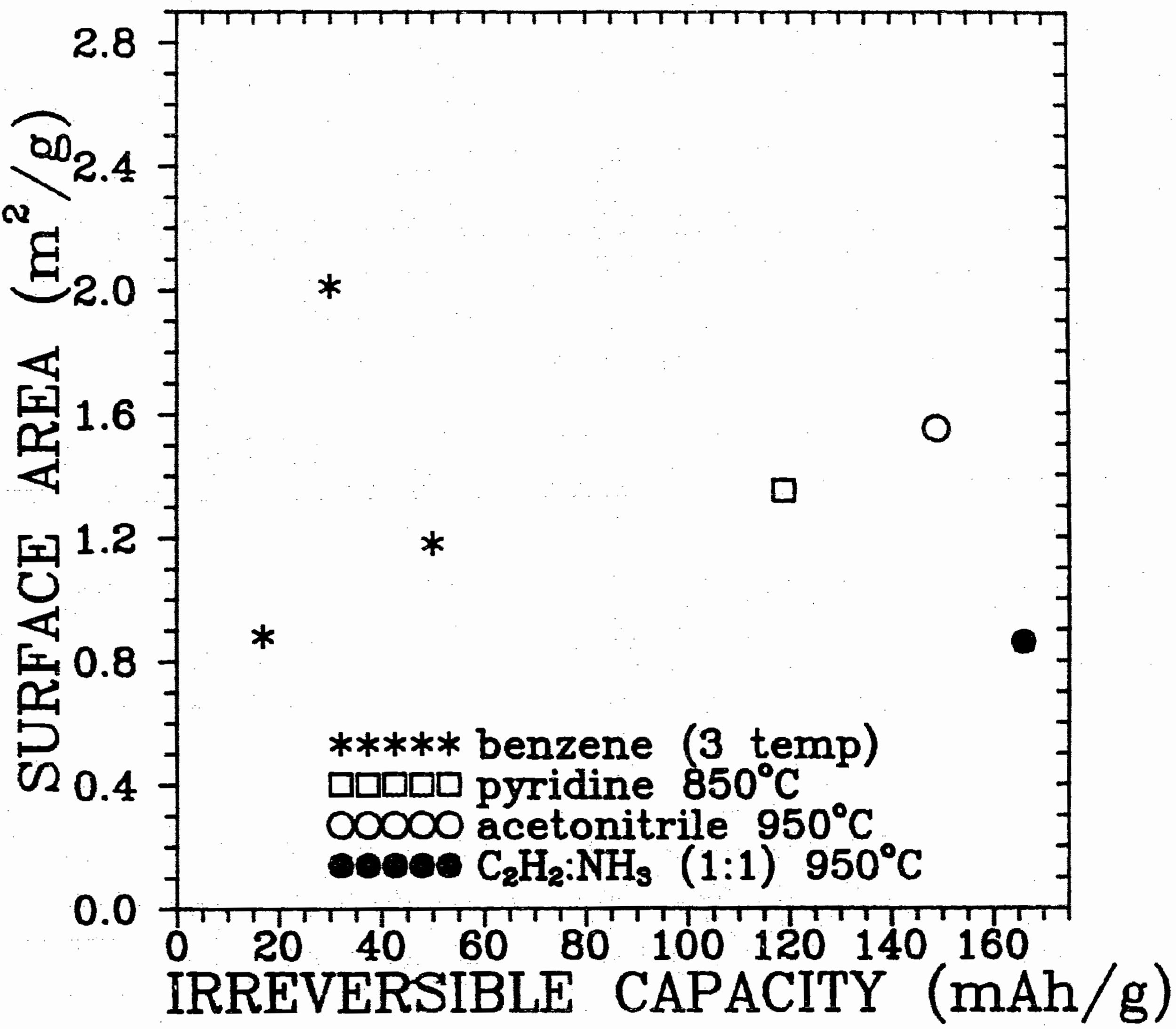

Fig. 4.10 Surface area from BET measurements versus irreversible capacity for selected samples prepared from benzene, pyridine, acetonitrile and $C_2H_2:NH_3$ (1:1).

are shifted upward by 1.0V and 2.0V respectively for ease of viewing. The irreversible capacity is largest for the sample made from acetonitrile 900°C ($\delta x=0.50$) which also has the largest nitrogen content (cf. Table 1). It is lower ($\delta x=0.28$) for pyridine 900°C and lowest for benzene 900°C ($\delta x=0.08$). There is clear dependence of irreversible capacity on nitrogen content.

Figure 4.12 shows the irreversible capacity for all samples plotted versus their nitrogen content given in Table 1. The irreversible capacity can be expressed in two ways, either as x in Li_xC_6 or in units of mAh/g, where x=1 in Li_xC_6 corresponds to 370mAh/g capacity. The irreversible capacity is roughly proportional to the nitrogen content in the material as indicated by the solid line in Figure 4.12 that serves as a guide to the eye. This suggests that some nitrogen containing species in the electrode materials is reacting irreversibly with lithium on the first electrochemical lithium transfer. We will call this reactive nitrogen species 'chemical nitrogen'.

In Table 1 we have also listed the hydrogen content for all samples. We believe that it is the nitrogen content, not the hydrogen content, that most strongly affects the irreversible capacity in these samples. For example, the samples made from benzene and acetonitrile at 900°C have similar hydrogen content, but the latter has much larger irreversible capacity due to its large nitrogen content. As well, the

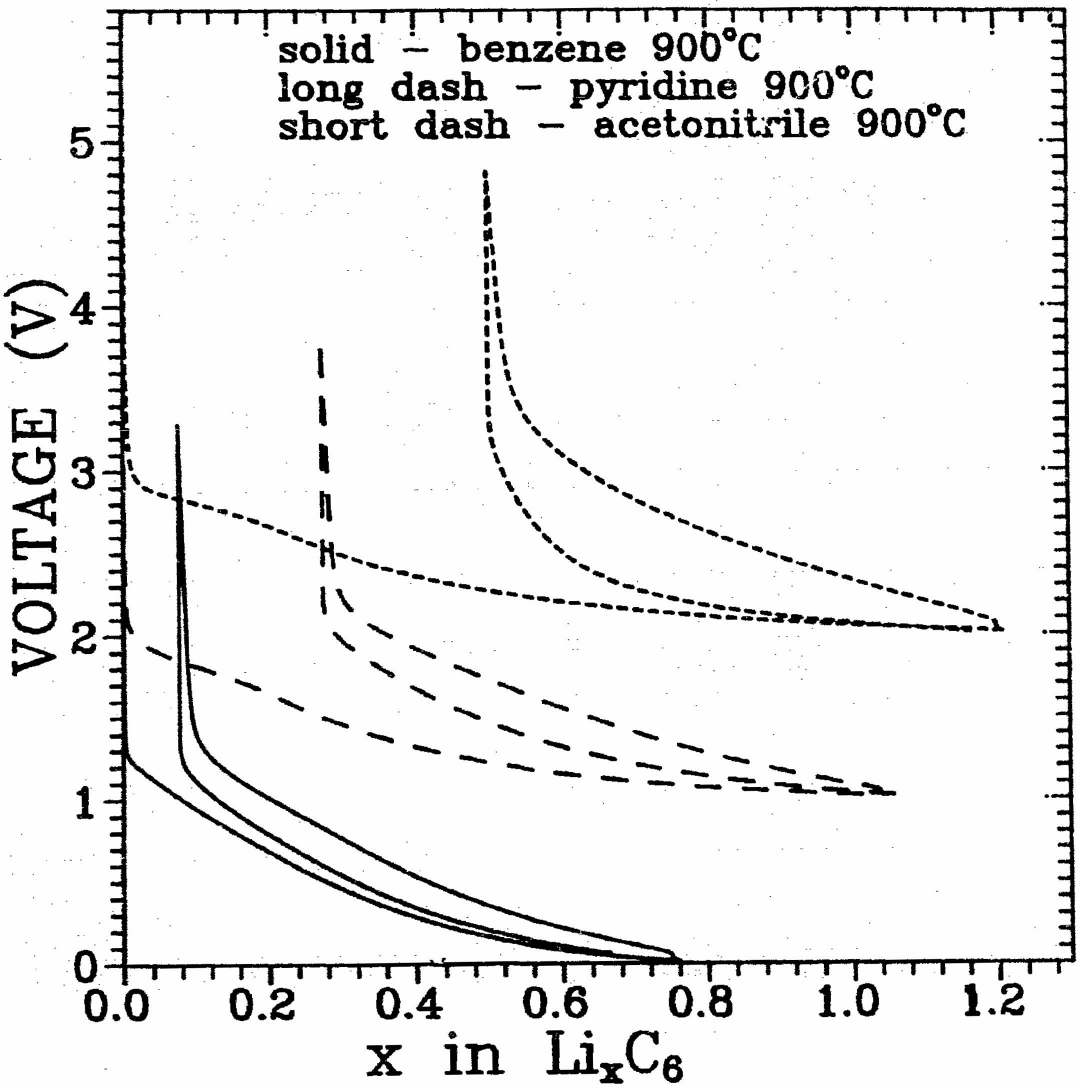

Fig. 4.11 Cell voltage curves versus x in $Li_x(N_yC_{1-y})_6$ for the three samples made from benzene, pyridine and acetonitrile at 900°C.

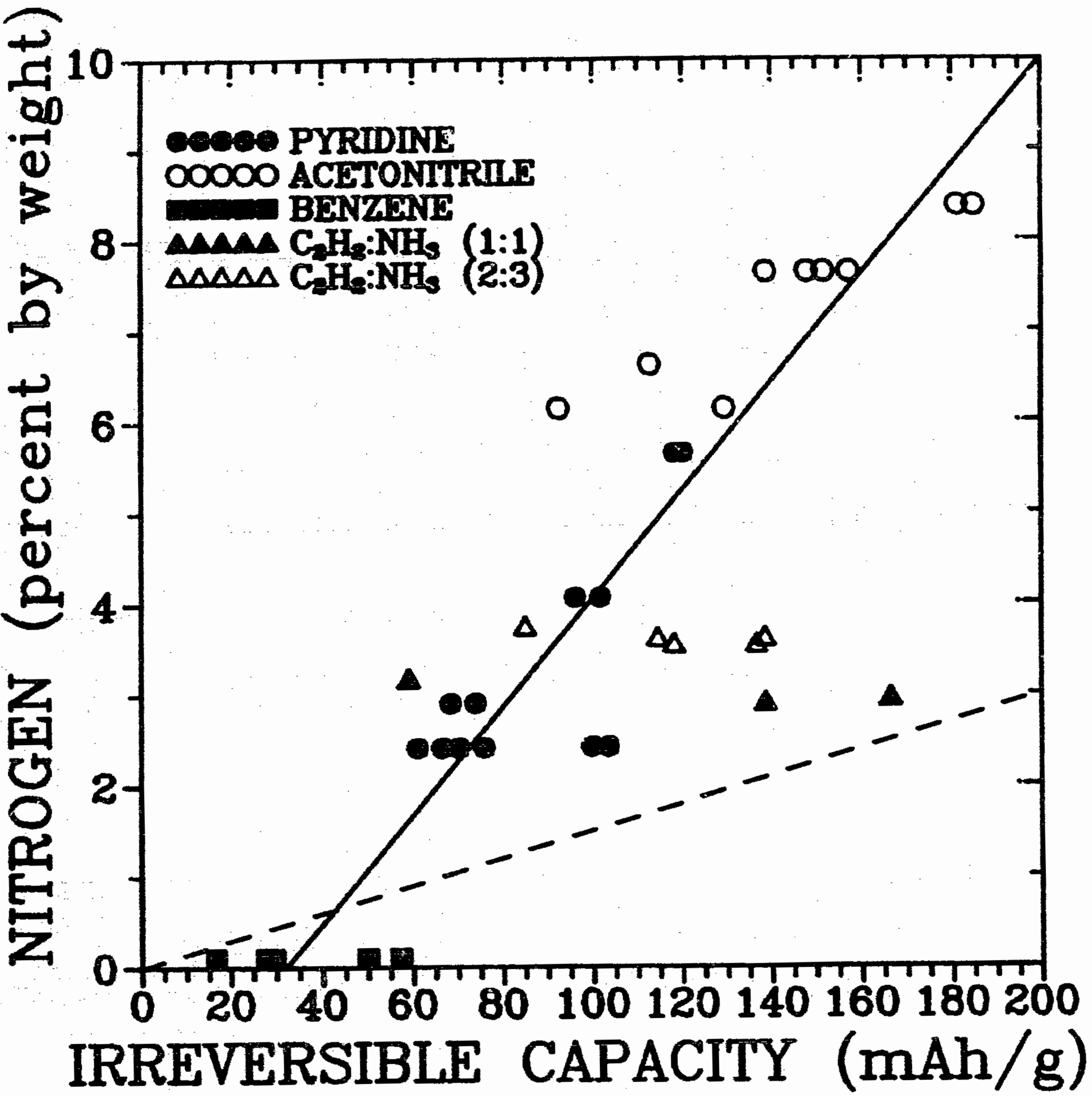

Fig. 4.12 Irreversible capacity vs. nitrogen content for all prepared samples. The meaning of the lines is explained in the text.

simplest imaginable reaction of hydrogen with lithium ($Li + H \rightarrow LiH$) consumes a lot less lithium than the equivalent reaction of lithium with nitrogen.

The simplest possible lithium reaction with nitrogen is: $3\ Li + N \rightarrow Li_3N$, which is a well known spontaneous reaction. This reaction consumes large amounts of lithium (three lithium atoms per nitrogen atom), especially compared to the intercalation reaction where only one lithium is intercalated for every six carbon atoms. Irreversible capacities that would correspond to the amount of lithium used if all nitrogen in the material would follow the above reaction are indicated in Figure 4.12 as the dashed line. As we can see from the position of the line, this reaction can not be used solely to explain the observed phenomenon, since none of the samples shows high enough irreversible capacity. More likely is that complex lithium-nitrogen-organic products are formed and that some nitrogen does not react irreversibly but changes the cell properties reversibly as we will show later below.

This very high irreversible capacity, observed for the nitrogen containing cells is an unexpected effect, not seen for any previously used substituents in carbon electrodes. Nitrogen in the materials does, however, not seem to influence the reversible capacity of the materials drastically. Reversible capacities for all prepared samples are shown in Figure 4.13 versus nitrogen content. There is a slight variation of the reversible capacity for the benzene samples, depending on

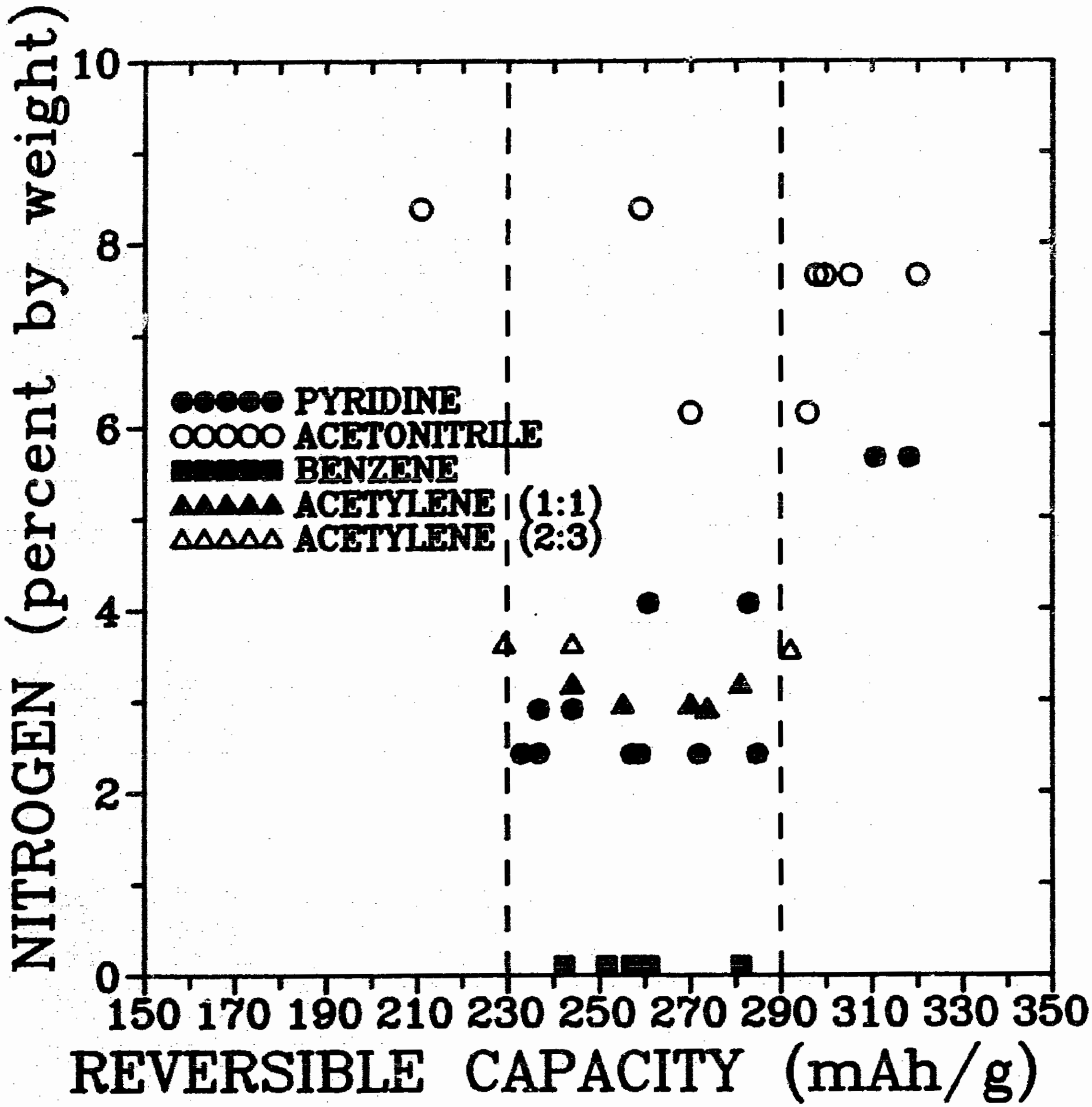

Fig. 4.13 Reversible capacity vs. nitrogen content for all prepared samples.

temperature. Figure 4.14 shows this more clearly, where the reversible capacity versus deposition temperature is plotted. From earlier experiments [1-18] on heat treated carbons we expect a slight linear decrease of reversible capacity with temperature for this temperature range. The slight variation of experimental conditions between the different powder production runs introduces errors so that this trend of reduction in reversible capacity is hard to see in Figure 4.14.

Concluding, nitrogen in the material has a rather small effect on the reversible capacity. We certainly do not see an increase in reversible capacity by 30% as was observed for the phosphorus containing samples mentioned in Section 1.3 [1-25,1-27].

4.2.2 Capacity Shift to Lower Voltage

Figure 4.9 also demonstrates another interesting effect. During each cycle, not only the first, the capacity of the cell containing carbonaceous material made from pyridine 850°C begins at a lower voltage than that of the cell containing pure carbon made from benzene. It is clearly seen in the graph of dx/dV versus V shown in the inset of Figure 4.9. The derivative dx/dV is zero for higher voltage, but around 1.1V, for the nitrogen containing material, starts deviating from zero and assumes non-zero values. We consider this point as the start of cell capacity. For the pure carbon sample this point is at about 1.4V.

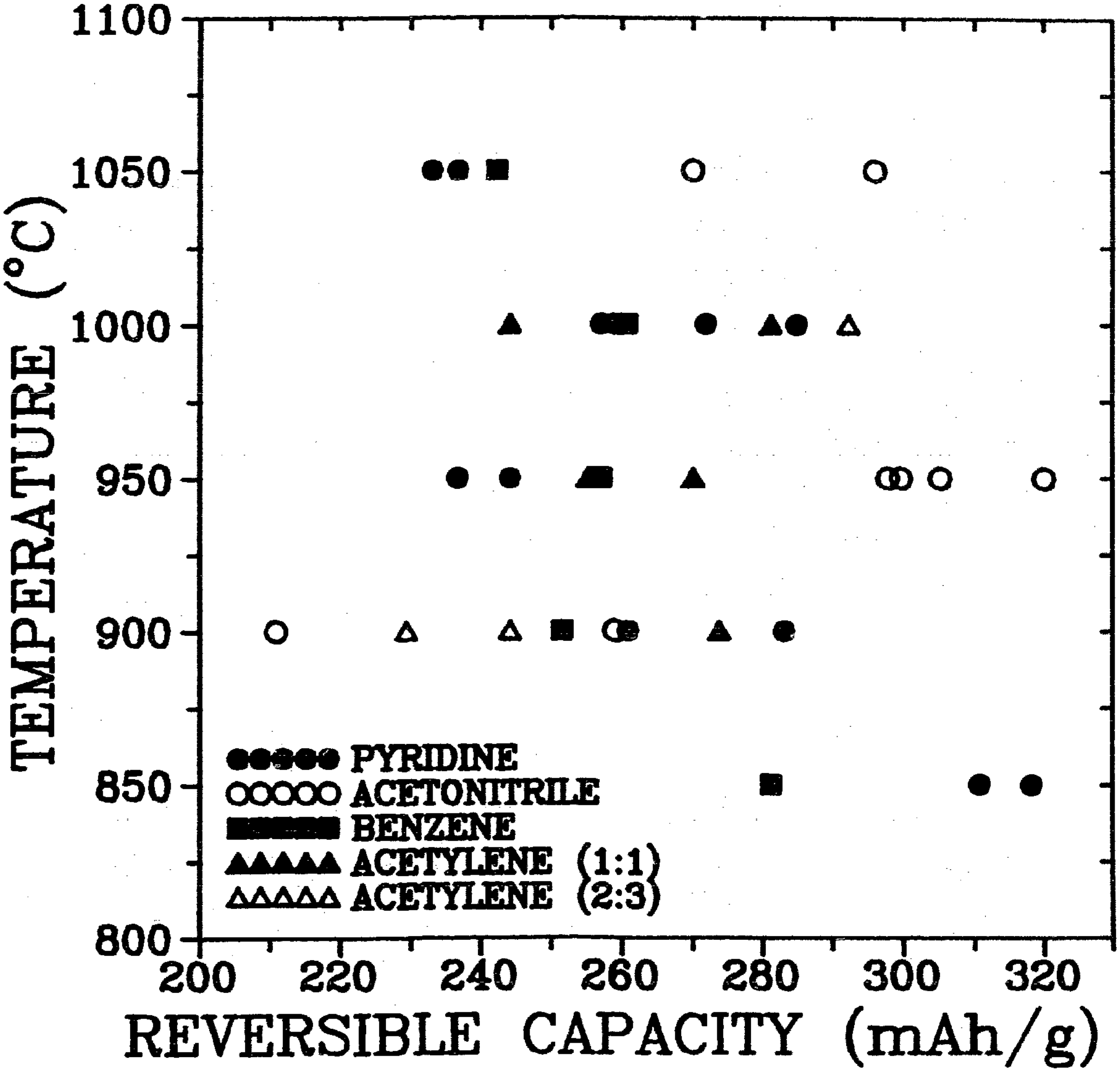

Fig. 4.14 Reversible capacity vs. deposition temperature for all prepared samples.

This means, that there are only very few empty sites in the nitrogen doped carbon that can intercalate lithium at voltages above 1.1V against lithium metal. In the pure carbon, there are sites that can intercalate lithium from 1.4V onward. A detectable amount of lithium only starts intercalating into nitrogen containing carbon below 1.0V cell voltage. A more in depth discussion of this effect will be presented below in Section 5.2.

Increased capacity can also be observed at lower voltage for the nitrogen containing cell compared to the pure carbon cell. This can be seen clearly from the derivative plot, dx/dV, in the inset in Figure 4.9. Below 0.5V the density of sites for lithium is larger in the nitrogen containing cell, observed by a shift of the curve for nitrogen containing carbon to higher values of $|dx/dV|$ (that is down in the plot for dx/dV) compared to the pure carbon material. Some irreversible capacity originates at low voltage, as the curve for the second discharge shows lower capacity in this region (i.e. it shifts upward in the dx/dV plot) compared to the curve for the first discharge.

This has to be contrasted with the behaviour of electrodes where boron has been substituted for carbon. Figure 4.15 shows V(x) for a $Li/B_{0.1}C_{0.9}$ cell, from [1-24], compared to a cell with a pure carbon electrode (the benzene 900°C sample) prepared at the same temperature. The presence of boron causes a large shift in cell capacity to higher cell voltage, as has been previously reported [1-23, 1-24]. The

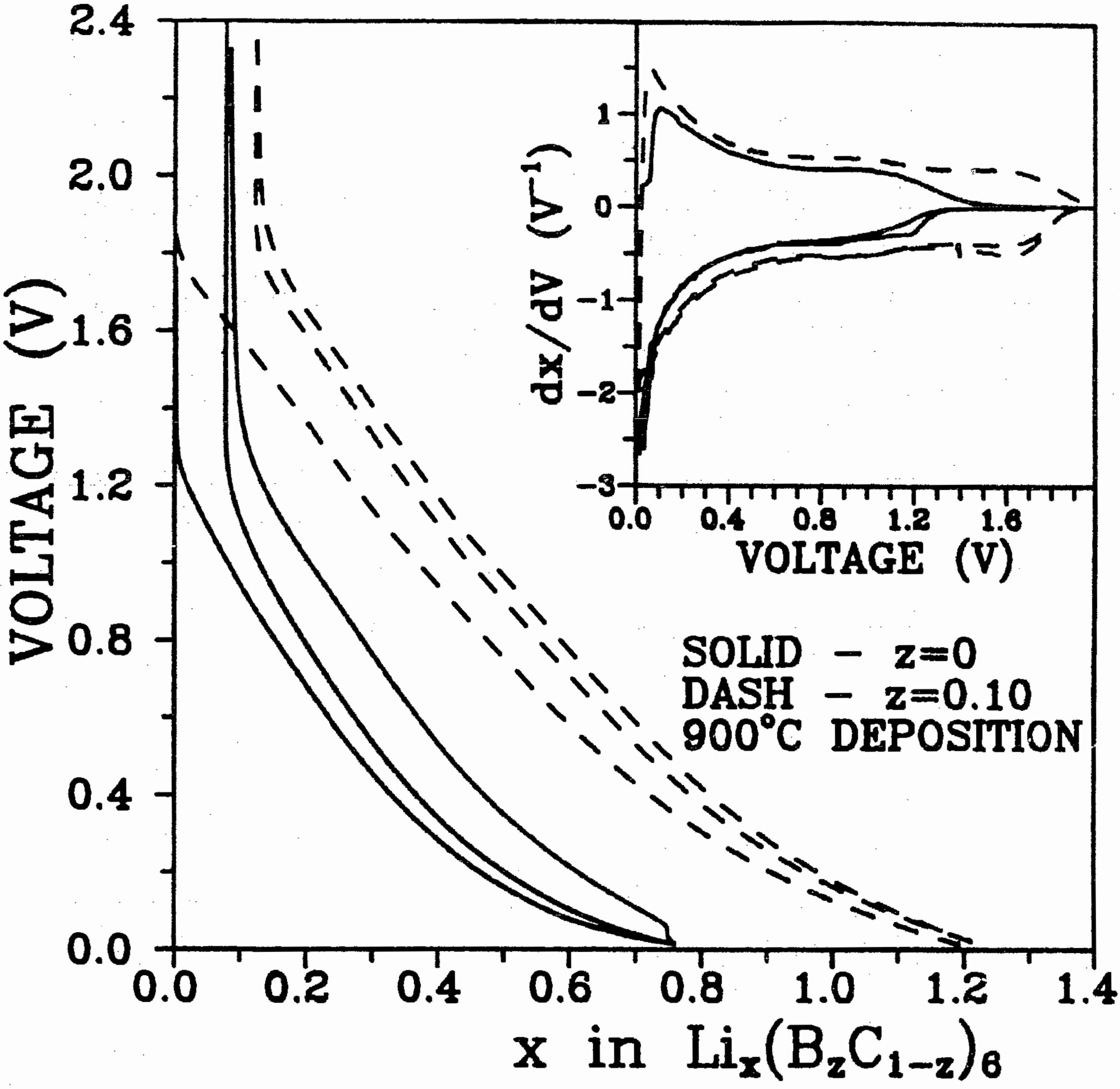

Fig. 4.15 Voltage and derivative curve for a sample of $B_{0.1}C_{0.9}$ and a benzene reference produced at 900°C.

reversible capacity starts at 1.8V and is increased over the capacity for a pure carbon compound all the way down to about 0.1V.

Clearly substituents for carbon in graphitic materials have a strong effect on the shape of V(x) for the respective Li/carbon cells manufactured using those compounds.

CHAPTER FIVE: DISCUSSION

We showed in Section 4.2 that the nitrogen which has been incorporated into our materials causes two different effects. We conclude that it exists in our samples in two different forms: 1) 'chemical nitrogen', which leads to an increase in irreversible capacity and 2) 'lattice nitrogen', which leads to a shift in the Li/N_zC_{1-z} cell capacity to lower voltage, compared to nitrogen free carbon made at the same temperature. It is difficult for us to quantify the amount of each species present in our samples. However, many trends can be clearly observed.

5.1 UNDERSTANDING THE 'IRREVERSIBLE CAPACITY'

Table 1 shows that the irreversible capacity and the nitrogen content decrease in general with higher preparation temperature. This implies that the chemical nitrogen content is reduced with increasing heating temperature.

Figures 5.1, 5.2 and 5.3 show V(x) and dx/dV versus V for Li/N_zC_{1-z} cells with electrodes made from pyridine at 900°C, 950°C and 1000°C. Using Figure 4.9 for comparison, we see that as the heating temperature increases dx/dV behaves more like that of cells with carbon

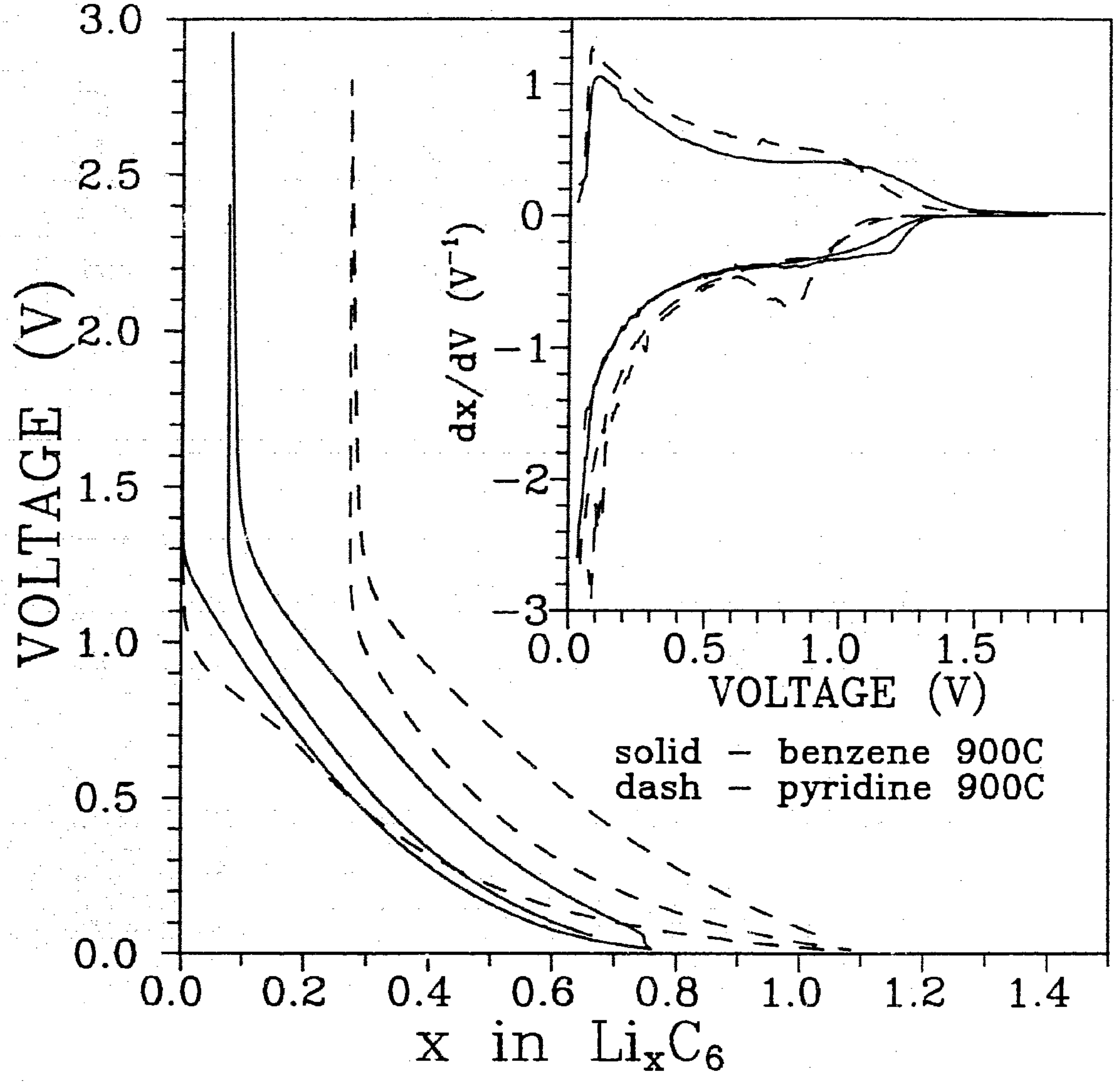

Fig. 5.1 Voltage and derivative curve for the pyridine 900°C sample and a benzene 900°C reference.

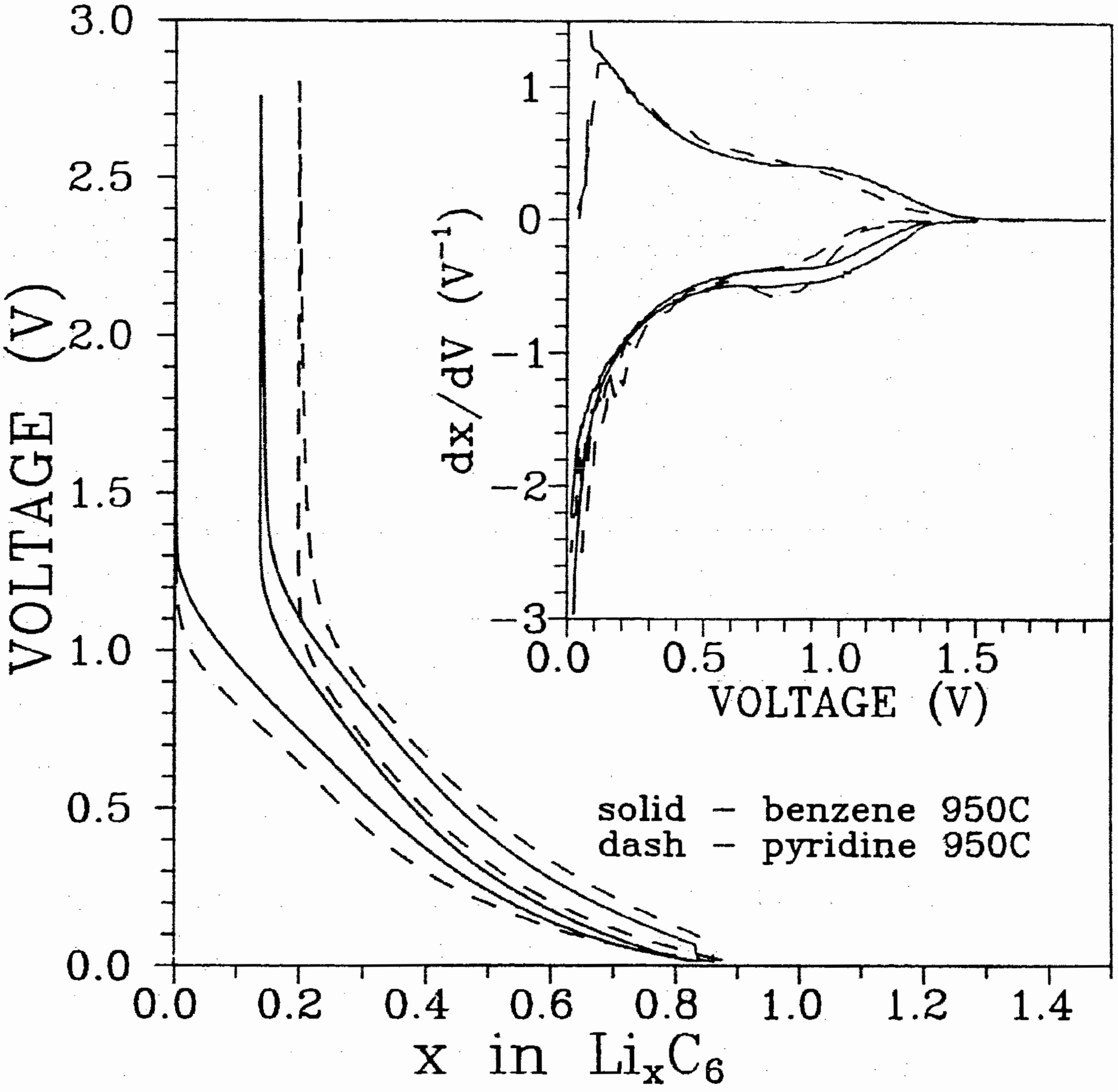

Fig. 5.2 Voltage and derivative curve for the pyridine 950°C sample and a benzene 950°C reference.

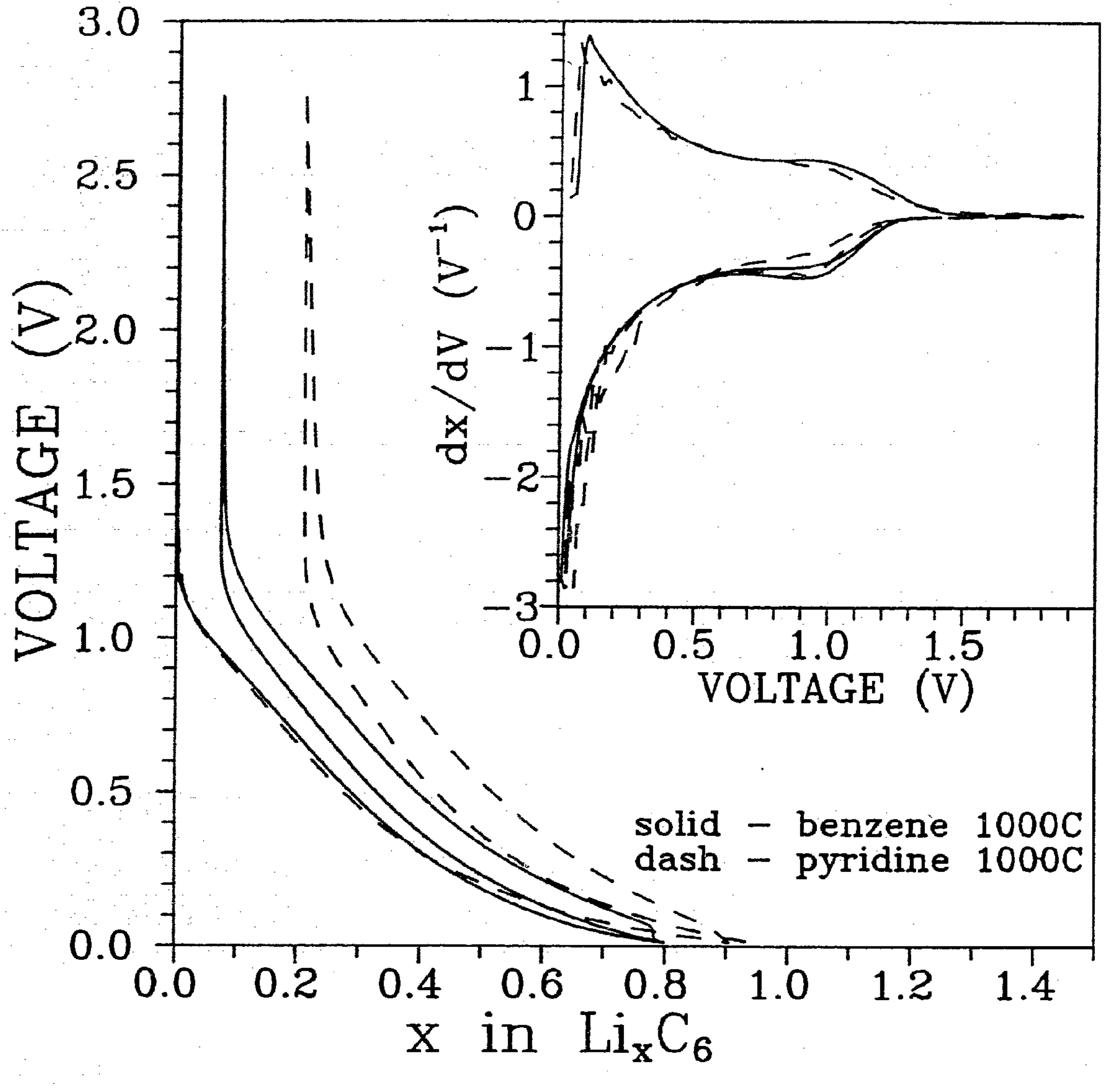

Fig. 5.3 Voltage and derivative curve for the pyridine 1000°C sample and a benzene 1000°C reference.

electrodes made from benzene. The additional capacity at around 0.8V (broad peak in the derivative curve) decreases with increasing temperature, but the irreversible capacity at low voltage stays roughly constant. The shift in the voltage curve becomes smaller with increasing temperature and nearly disappears for the sample produced at 1000°C, c.f. Figure 5.3. This suggests that less lattice nitrogen is incorporated in the film as the synthesis temperature increases, in agreement with [5-1]. It agrees with the fact that the total nitrogen content in the film is low for this sample.

The chemical nitrogen apparently varies depending on how the N_zC_{1-z} is prepared in terms of deposition temperature and method. The peak in dx/dV near 0.8V during the first discharge in Figures 4.9, 5.1, 5.2 and 5.3 is thought to be caused by the reaction of chemical nitrogen with lithium and disappears after the first discharge. Figure 5.4 shows V(x) and dx/dV versus V for a Li/N_zC_{1-z} cell with material prepared from C_2H_2:NH_3 (1:1) 950°C (referred to as 'C_2H_2+NH_3 950C' in the figure). In addition to a relatively small peak in the derivative near 0.75V, there is a sharp irreversible capacity peak near 0.25V during the first discharge of the cell. Similar behaviour is seen for the C_2H_2:NH_3 (2:3) 950°C sample (referred to as 'C_2H_2 (2:3) 950C' in the figure), shown in Figure 5.5. The peak in dx/dV near 0.25V is caused by the irreversible capacity in this material. This suggests that different chemical nitrogen species are responsible for the two features seen in the derivative plot around 0.8V and 0.25V, which we associate with irreversible capacity. They are likely to be caused by the different deposition mechanisms.

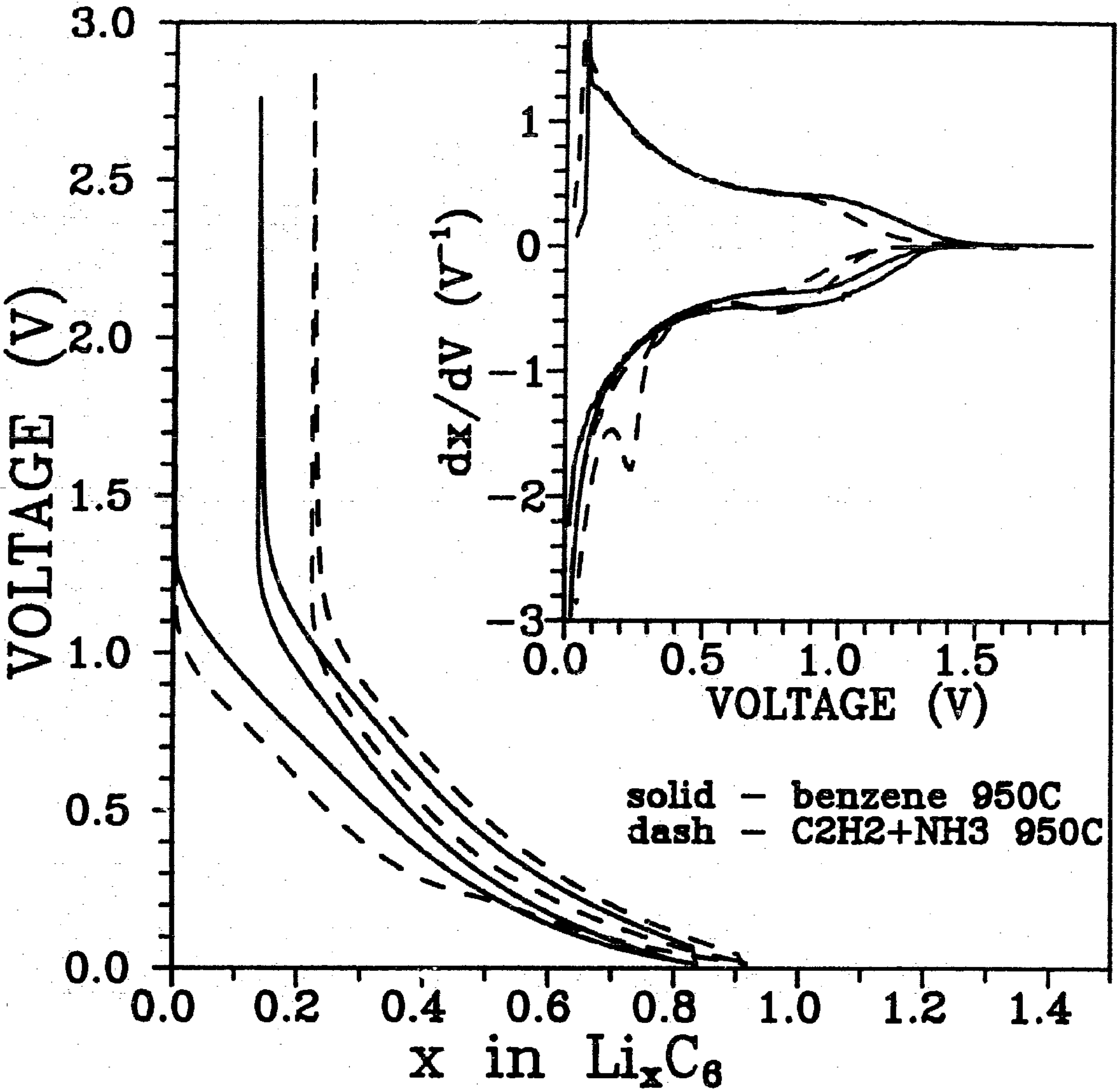

Fig. 5.4 Voltage and derivative curve for the $C_2H_2:NH_3$ (1:1) 950°C sample and a benzene 950°C reference.

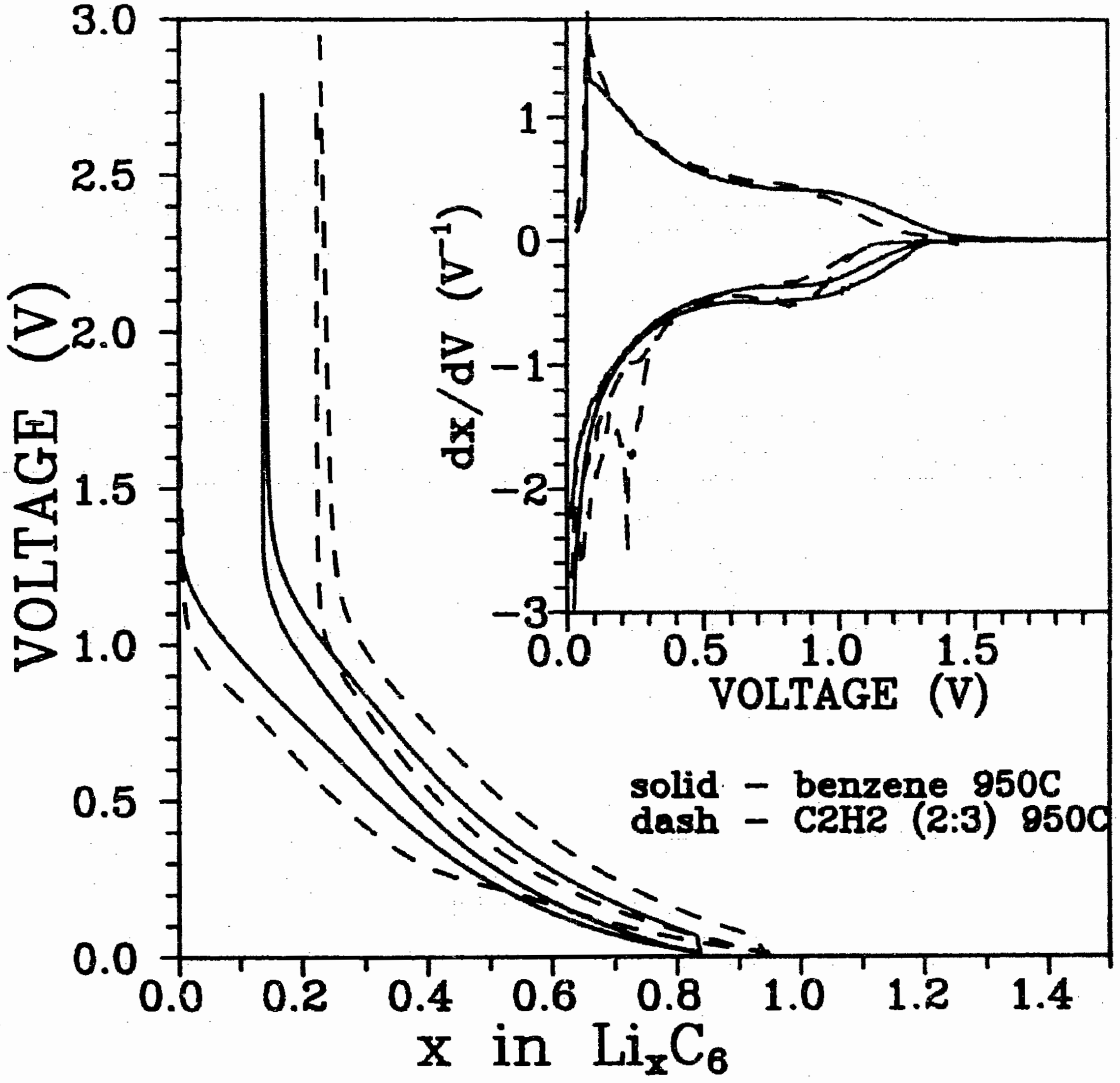

Fig. 5.5 Voltage and derivative curve for the C_2H_2:NH_3 (2:3) 950°C sample and a benzene 950°C reference.

5.2 REVERSIBLE CAPACITY OBSERVED AT A CERTAIN VOLTAGE

The reversible capacity at a certain voltage is influenced greatly by the substitution of carbon atoms by boron or nitrogen. The effect these two dopants have on carbon materials can be understood using the following qualitative argument.

Elemental boron, carbon and nitrogen have 3, 4 and 5 valence electrons respectively. Thus, boron substituted for carbon in a graphitic material will act as an electron acceptor and nitrogen will act as an electron donor. When lithium is intercalated into carbon it donates its 2s electron to the carbon host. This charge transfer is an effect of the chemical bond between lithium and the carbon host,formed during intercalation. The strength of the bond determines the chemical potential of the intercalated lithium in the solid host which, in turn, determines the cell voltage as described in Section 1.4.

Since boron acts as an acceptor, its presence will strengthen the lithium-host bond, hence increasing the voltage of a Li/B_zC_{1-z} cell compared to one with a pure carbon electrode. We can also observe an effect on the 'density of sites' available for lithium in the carbonaceous material at a certain voltage. The derivative dx/dV is a measure of this 'density of sites', which is closely connected with the density of states (DOS) for the electrons because each intercalated lithium atom transfers its 2s electron to the carbon host. For the boron doped carbon with the highest boron concentration ($B_{0.17}C_{0.83}$) the Fermi energy, E_F, drops by about 1.3V from its former position in the DOS plot for carbon, see Figure 3.5, from [1-22]. Assuming that the DOS calculated from the band structure for pure carbon does not change due to the boron substitution [1-22,3-3,3-10], this results in a DOS increase at E_F, as can be seen in Figure 3.5.

Conversely, the presence of nitrogen will have the opposite effect. The capacity of nitrogen containing carbon should shift to lower voltage compared to pure carbon, due to a weakening of the lithium-carbon bond. We expect a slight movement of E_F upward in the DOS plot in Figure 3.5 due to the substitutional nitrogen. It is caused solely by the lattice nitrogen in the material. Its percentage in the material is markedly less than the percentage of boron in $B_{0.17}C_{0.83}$ and thus we expect a less dramatic effect.

Figure 5.6 clearly shows the effects on the capacity for boron and nitrogen containing samples all produced at 900°C. The derivative for the boron containing material shows capacity starting at 1.85V, the capacity for the carbon sample starts around 1.3V and the nitrogen containing pyridine 900°C sample shows capacity below 1.1V. It must be emphasized that the substitutional boron concentration, y, in the B_yC_{1-y} material, described by Figures 4.15 and 5.6, is probably at least three times the substitutional nitrogen content, z, in the N_zC_{1-z} material, described by Figures 4.9 and 5.6. This is certainly part of

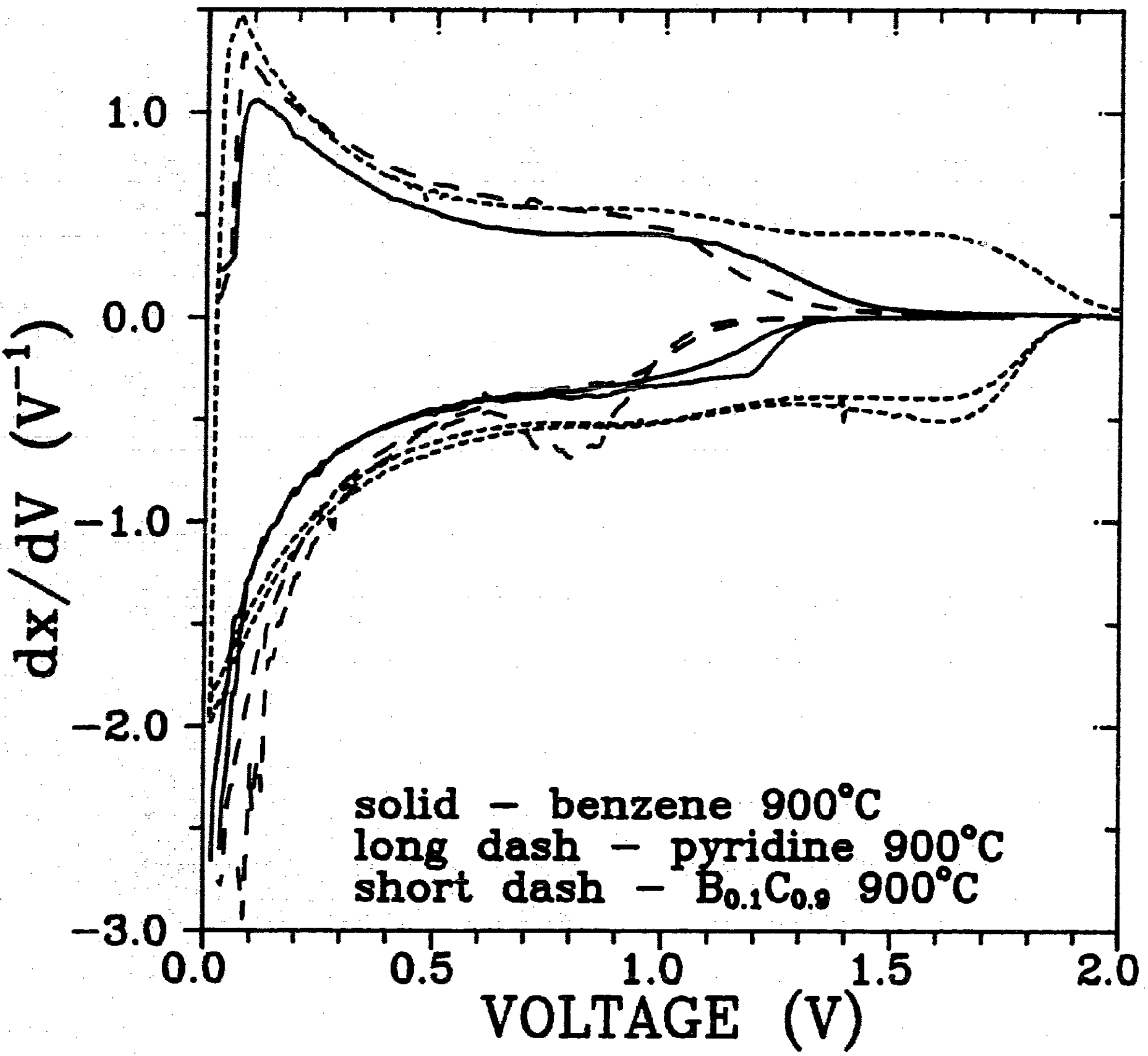

Fig. 5.6 Derivative curves for the benzene 900°C sample, the $B_{.1}C_{.9}$ material produced at 900°C and the pyridine 900°C sample.

the reason why the effect of boron is much more striking as E_F drops more for the boron substituted materials than it rises for the nitrogen substituted samples. In both cases the Fermi level position with respect to the minimum in the DOS will clearly differ from that observed for pure carbon electrodes.

Nitrogen, which has been substitutionally incorporated in the carbon lattice greatly affects the voltage and derivative curves of Li/N_zC_{1-z} cells . This effect persists throughout each of the charge and discharge cycles of the cell, suggesting that the nitrogen causing this effect remains incorporated within the lattice.

5.3 AUGER ELECTRON SPECTROSCOPY AND CHEMICAL NITROGEN

To try to confirm our hypothesis of 'chemical' and 'lattice' nitrogen, we assembled, then discharged a series of Li/N_zC_{1-z} cells to different voltages. We then analyzed their carbonaceous electrodes with Auger electron spectroscopy. Five cells with electrodes prepared from the acetonitrile 950°C sample were tested. These were discharged to 0.8V, 0.6V, 0.4V, 0.2V and 0.01V respectively and then fully charged to 2.8V. The cells were opened and the electrodes recovered, rinsed and dried as described in Section 3.4. Auger Electron Spectroscopy (AES) was then used to measure the nitrogen content (subject to the uncertainties described in the experimental section) of each electrode.

The same scans were also taken on an as-made acetonitrile 950°C cathode that had been rinsed likewise. We expect more and more chemical nitrogen to react with lithium as the depth of discharge increases (discharge to lower voltage). If the reaction products of the lithium/nitrogen reaction would be soluble in methanol and could be washed out, we would expect a decrease in the nitrogen content in the cycled cathodes over the test series.

Figure 5.7 shows the nitrogen content in atomic percent versus the discharge turnaround voltage. Clearly, the nitrogen content decreases as the discharge voltage decreases, within the experimental error. Ideally the reaction products formed by the irreversible reaction of lithium with the chemical nitrogen species would be washed out by the rinsing, where the lattice nitrogen would stay incorporated in the structure of the material. Then only this lattice nitrogen would be seen in the Auger data. Compared to the nitrogen content of the rinsed as-made battery cathode, plotted at 1.2V, some of the nitrogen is lost once the cell is discharged to 0.8V, the area where the derivative curves in e.g. Figures 4.9 or 5.1 show a major peak of irreversible capacity. There is a further drop in nitrogen content below 0.4V, which corresponds to the uniformly distributed irreversible capacity at low voltage.

The AES data is consistent with our model for the origin of irreversible capacity, but still does not give certain proof for

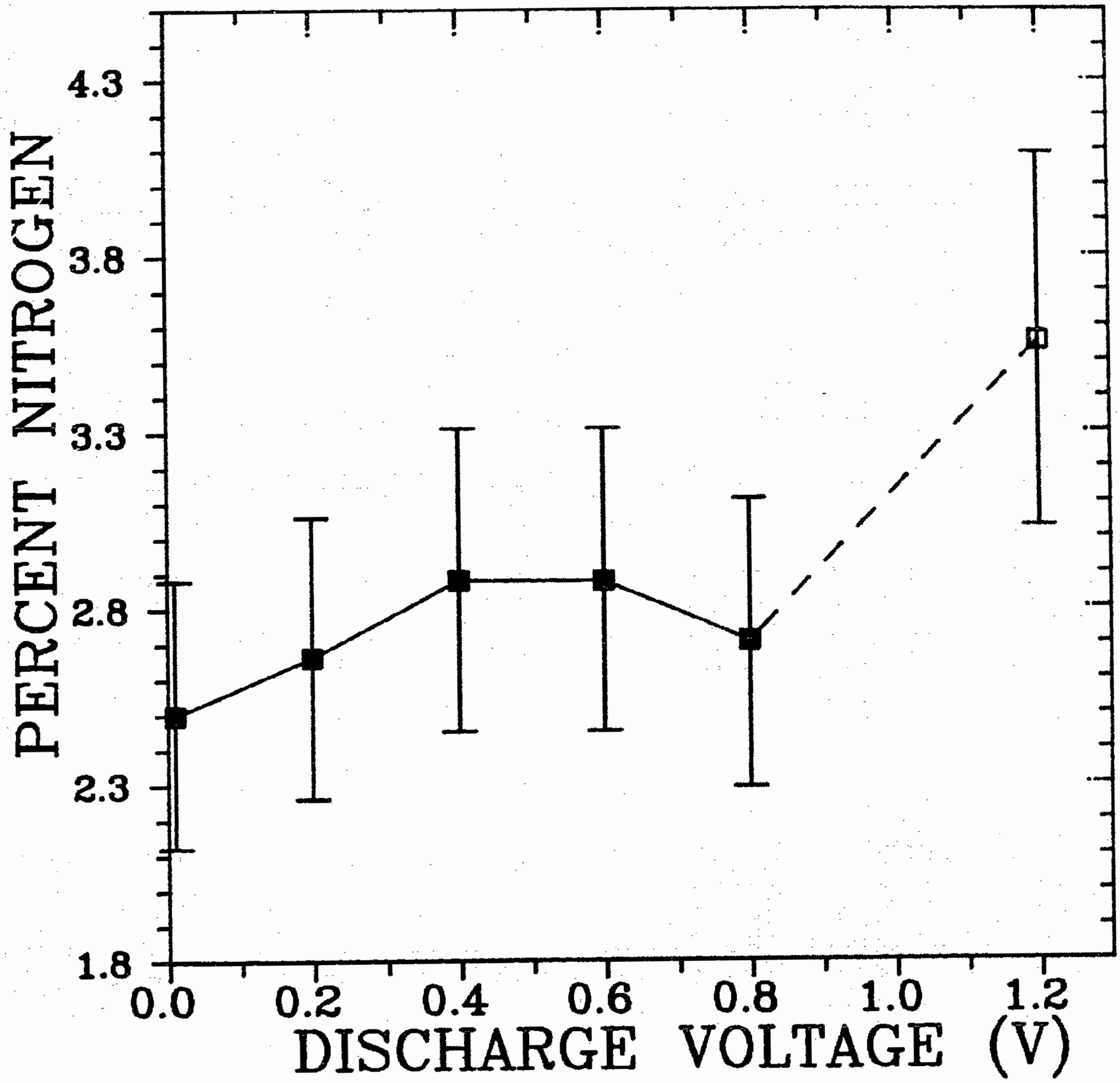

Fig. 5.7 Nitrogen content according to Auger electron spectroscopy on cathodes made from acetonitrile 950°C after discharging to the voltages indicated. The data point at 1.2V corresponds to the reference cathode, which had not been cycled.

'chemical nitrogen'. The nitrogen content as seen by AES for the fully discharged and charged samples most probably represents both lattice nitrogen and insoluble reaction products of chemical nitrogen. The solubility of the nitrogen reaction products is adversely affected by the binder in the cathode material, and we are uncertain about the amount of chemical nitrogen in the material to begin with. Nevertheless the trend in the data is consistent with our proposed explanation for irreversible capacity.

CHAPTER SIX: CONCLUSIONS AND OUTLOOK

We have prepared nitrogen containing carbons in a variety of ways. Using x-ray diffraction, x-ray absorption, Auger Electron Spectroscopy and electrochemical measurements of differential capacity, dx/dV, we showed that some of the nitrogen is substitutional for carbon ('lattice nitrogen') in the N_zC_{1-z} materials. On the other hand, there is also strong evidence for nitrogen containing chemical species ('chemical nitrogen') incorporated in these carbons which reacts irreversibly with lithium. The irreversible capacity of nitrogen containing carbons is directly correlated to the nitrogen content, suggesting the presence of 'chemical nitrogen'.

Both the 'chemical nitrogen' and the 'lattice nitrogen' strongly affect the behavior of Li/N_zC_{1-z} cells. The former causes irreversible capacity and the latter shifts the reversible cell capacity to lower voltage. The combination of these effects, in particular the very high irreversible capacity observed, suggests that these materials will <u>not</u> be useful as Li-ion cell anode materials. It is clear that at least 'chemical nitrogen' should be avoided in such cells at all cost.

A further project in this area could be to understand the 'chemical' nitrogen and its origin in the deposition process better and try to reduce it in the samples by finding different ways of producing nitrogen containing carbons or by trying to convert 'chemical' nitrogen into 'lattice' nitrogen by means of heat treatment. Heat treatment to very high temperatures, around 3000°C, has been proven to enhance the electrochemical properties of carbon/graphite greatly by increasing the structural order of the atoms. As well it could remove the chemical nitrogen but might also remove part of the lattice nitrogen.

As far as other substitutional dopants are concerned, a thorough study of different stoichiometric combinations of boron and nitrogen in carbon might be interesting, as the combination of these dopants does not show the extreme irreversible capacities we observed for only nitrogen substitution here [1-28].

A systematic study of phosphorus doped carbons produced by decomposition of phosphorus containing precursors could be interesting as well. Earlier studies used phosphorus doped polymers for carbon production [1-26], and thus were producing so called 'hard carbons', which can not be graphitized as well as our 'soft carbons'.

Substitution of carbon by other elements is imaginable as well. Aluminum, being similar to boron in its properties (located one row down from boron in the periodic table) could be an interesting candidate to try, as boron doping was quite successful. Silicon, which is somewhat similar to carbon in its properties, seems interesting and is being tried at the moment. The halogenides do not yield good results as substituents. They make high capacity carbons, but the intercalation into those materials is mostly irreversible, which makes them useless as electrode materials for lithium-ion cells.

LIST OF REFERENCES

CHAPTER 1:

[1-1] J.M. Tarascon and D.G. Guyomard, paper #74 presented at the 1993 Spring Meeting of the Electrochemical Society, Honolulu, Hawaii, May 16-21 (1993).

[1-2] J. Desilvestro and O. Haas, J. Electrochem Soc. 137, 5c (1990).

[1-3] A. Demachi, paper #19 presented at the 1993 Spring Meeting of the Electrochemical Society, Honolulu, Hawaii, May 16-21 (1993).

[1-4] E.J. Cairns and F.R. McLarnon, paper #21 presented at the 1993 Spring Meeting of the Electrochemical Society, Honolulu, Hawaii, May 16-21 (1993).

[1-5] E.Z. Ratner, P.C. Symons, W. Walsh and C.J. Warde, Study on: Assessment of battery technologies for electrical vehicles, Vol 1, prepared for EG&G Idaho, U.S. Department of Energy et.al., (August 1989).

[1-6] "Cellular Phone Recall may Cause Setback for Moli", Toronto Globe & Mail, August 15, 1989, Toronto, Canada.

[1-7] J.R. Dahn, U. von Sacken, M.W. Juzkow and H. Al-Janaby, J. Electrochem. Soc. 138, 783 (1991).

[1-8] T. Nagaura and K. Tozawa, Progress in Batteries and Solar Cells, 9, 209 (1990).

[1-9] D. Guyomard and J.M. Tarascon, J.Electrochem. Soc. 139, 937 (1992).

[1-10] T. Ohzuku, M. Kitagawa and T. Hirai, J. Electrochem. Soc. 137, 769 (1990).

[1-11] Battery & EV Technology, 12 (7), 2 (1988).

[1-12] R.W.G. Wyckhoff, Crystal Structures, Volume 1, p 27, 2nd edition, R.E. Krieger Publishing Company, Malabar, Florida, 1982.

[1-13] N.W. Ashcroft, N.D. Mermin, Solid State Physics, pp 304-305, W.B. Saunders Company, Philadelphia (1976).

[1-14] Facility Reports, Synchrotron Radiation News, 5, 9 (1992).

[1-15] Materials & Electrochemical Research (MER) Corporation release, April 15 (1993).

[1-16] Y. Chabre, D. Djurado, M. Armand, W.R. Romanow, N. Coustel, J.P. McCauley Jr., J.E. Fischer and A.B. Smith III, J. Am. Chem. Soc., 114, 764 (1992).

[1-17] M. Fujimoto, K. Ueno, T. Nohma, M. Takahashi, K. Nishio and T. Saito, paper #72 presented at the 1993 Spring Meeting of the Electrochemical Society, Honolulu, Hawaii, May 16-21, (1993).

[1-18] J.R. Dahn, A.K. Sleigh, H. Shi, J.N. Reimers, G. Zhong and B.M. Way , Electrochimica Acta, 38, 1179 (1993).

[1-19] R.E. Franklin, Proc. Roy. Soc. (London) A, 209, 196 (1951).

[1-20] D.B. Fischbach, The Kinetics and Mechanism of Graphitization, in: Chemistry and Physics of Carbon, ed by P.L. Walker Jr., Vol. 7, pp 107-154, Marcel Dekker Inc., New York (1971).

[1-21] J. Maire, J. Méring, Graphitization of soft carbons, in: Chemistry and Physics of Carbon, ed by P.L. Walker Jr., Vol. 6, pp 128-170, Marcel Dekker Inc., New York (1970).

[1-22] J.R. Dahn, J.N Reimers, A.K. Sleigh and T. Tiedje, Phys. Rev. B 45, 3773 (1992).

[1-23] B.M. Way and J.R. Dahn, Paper #42 presented at the 1992 Fall Meeting of the Electrochemical Society, Toronto, Canada, October 12-16, (1992).

[1-24] B.M. Way and J.R. Dahn, submitted to J. Electrochem. Soc.

[1-25] A. Omaru, H. Azuma, M. Aoki, A. Kita and Y. Nishi, Paper #25 presented at the 1992 Fall Meeting of the Electrochemical Society, Toronto, Canada, October 12-16, (1992).

[1-26] H. Imoto, A. Omaru. H. Azuma and Y. Nishi, Paper #26 presented at the 1992 Fall Meeting of the Electrochemical Society, Toronto, Canada, October 12-16, (1992).

[1-27] Y. Nishi et. al., European Patent Application 89115940.2, August 29, 1989.

[1-28] M. Morita, T. Hanada, H. Tsutsumi, Y. Matsuda and M. Kawaguchi, J. Electrochem. Soc. 139, 1227 (1992).

[1-29] R.B. Kaner, J. Kouvetakis, C.E. Warble, M.L. Sattler and N. Bartlett, Mat. Res. Bull. 22, 399 (1987).

[1-30] W.R. McKinnon, Physical mechanisms of intercalation batteries, Ph.D. Thesis, University of British Columbia, Vancouver, Canada (1980).

[1-31] J.R. Dahn, Phys. Rev. B, 44, 9170 (1991).

[1-32] J.R. Dahn, R. Fong and M.J. Spoon, Phys. Rev. B, 42, 6424 (1990).

CHAPTER 2:

[2-1] N. Patibandla, K.L. Luthra, J. Electrochem. Soc., 139, 3558 (1992).

[2-2] D. Guyomard and J.M. Tarascon, U.S. Patent 5192629 (1993).

CHAPTER 3:

[3-1] E. Pella and B. Colombo, Mikrochimica Acta [Wien], 697 (1973).

[3-2] K.H. Tan, G.M. Bancroft, L.L. Coatsworth and B.W. Yates, Can. J. Phys. 60, 131 (1982).

[3-3] J.R. Dahn, J.N. Reimers, T. Tiedje, Y. Gao, A.K. Sleigh, W.R McKinnon, S. Cramm, Phys. Rev. Letters, 68, 835 (1992).

[3-4] G.W. Castellan, Physical Chemistry, p 547, 3rd edition, Addison-Wesley Publishing Company, Reading, Massachusetts (1983).

[3-5] J. Stöhr, NEXAFS Spectroscopy, p 277, Springer Series in Surface Science 25, Springer Verlag, Berlin (1992).

[3-6] R.A. Rosenberg, P.J. Love and V. Rehn, Phys. Rev. B, 33, 4034 (1986).

[3-7] A. Zangwill, Physics at surfaces, pp 250-253, Cambridge University Press, Cambridge (1988).

[3-8] D.A. Fischer, R.M. Wentzcovitch, R.G Carr, A Continenza, A.J Freeman, Phys. Rev. B, 44, 1427 (1991).

[3-9] W. Eberhardt, I.T. McGovern, E.W. Plummer and J.E. Fisher, Phys. Rev. Letters, 44, 200 (1980).

[3-10] International tables for X-ray crystallography, Vol III, 3rd edition, Kynoch Press, Birmingham (1969).

[3-11] J.N. Reimers, W. Li, J.R. Dahn, Phys. Rev. B, 47, 8486 (1993).

[3-12] D. Briggs, M. P. Seah, Practical Surface Analysis by Auger and X-ray Photoelectron Spectroscopy, pp 5-6, John Wiley & Sons, New York (1983).

[3-13] L.E. Davis, N.C. MacDonald, P.W. Palmberg, G.E. Riach, R.E. Weber, Handbook of Auger Electron Spectroscopy (second edition), Physical Electronics Division, Pelkin-Elmer Corporation, (1978).

CHAPTER 4:

[4-1] Z. Bashir, Carbon 29, 1081 (1991).

[4-2] J. Maire and J. Mering, Physics and Chemistry of Carbon, Volume 6 (1970).

[4-3] B.M. Way, J.R. Dahn, T. Tiedje, K. Myrtle and M. Kasrai, Phys. Rev. B 46, 1697 (1992).

[4-4] J.J. Yeh and I. Lindau, Atomic Data and Nuclear Data Tables, 32, 1-115 (1985).

[4-5] R. Fong, U. von Sacken and J.R. Dahn, J. Electrochem. Soc., 137, 2009 (1990).

[4-6] S. Brunauer, P.H. Emmett, E. Teller, J. Amer. Chem. Soc., 60, 309 (1938).

CHAPTER 5:

[5-1] J. Kouvetakis, T. Sasaki, C. Shen, R. Harigawa, M. Lerner, K.M. Krishnan and N. Bartlett, Synthetic Metals, 34, 1 (1989).